Investigating Ionospheric Scintillation Mechanisms via Theory and Experimentation

Burston, Robert

Award date:
2009

Awarding institution:
University of Bath

Investigating Ionospheric Scintillation Mechanisms via Theory and Experimentation

Submitted by Robert Burston
for the degree of Doctor of Philosophy

University of Bath
Department of Electronic and Electrical Engineering

January 2009

This thesis aims to answer the question, "What physical process dominates the formation of plasma irregularities, capable of directly or indirectly causing GPS L1 band scintillation, in polar cap plasma patches during magnetic storm conditions?." A novel modelling technique utilising an ionospheric imaging algorithm is developed and used to elucidate the relative importance of the two most commonly discussed processes. These are the Gradient Drift Instability (GDI) and turbulence induced by electric field mapping to the ionosphere from the magnetosphere. The results show that in magnetic storm conditions, at times the GDI process is dominant, but that at other times turbulence may be as significant as the GDI in determining how the plasma within a polar cap patch behaves, possibly more so. This in turn suggests that further study of the turbulence process is necessary in order to fully understand how big a role it plays in causing GPS L1 band scintillation in the polar cap. The success of the modelling technique developed here shows the utility of ionospheric imaging as a tool for understanding physical problems of the ionosphere; efforts to improve it and to apply it in other contexts would be worthwhile.

Acknowledgements

I gratefully acknowledge the following people for providing data without which the research presented here would be impossible: Dr. Lucilla Alfonsi, Prof. Cathryn Mitchell, Dr. Todd Pedersen and Dr. Susan Skone. I also gratefully acknowledge the Center for Space Sciences at the University of Texas at Dallas and the US Air Force for providing the DMSP thermal plasma data.

Table of Contents

List of Figures

List of Tables

Symbols and Abbreviations

A = distance from a receiver to a thin phase screen, $0<\theta<90^{o}$
A = amplitude of a plasma wave
A = mean molecular weight
A' = distance from a satellite to a thin phase screen, $0<\theta<90^{o}$
$\overline{A}$ = mean amplitude of a plasma wave over time.
B = magnetic field strength
B = $|\mathbf{B}|$ = magnetic field strength,
$\mathbf{B_0}$ = constant magnetic field strength
$B_0 = |\mathbf{B_0}|$ = constant magnetic field strength
B_a = magnetic field strength, region a
B_b = magnetic field strength, region b
C_A = Alfven Speed
CAT = Computed Axial Tomography
D = distance from a receiver to a thin phase screen, vertical incidence
D' = distance from a satellite to a thin phase screen, vertical incidence
DMSP = Defence Meteorological Satellites Program
e = charge on one electron.
E = electric field strength
E = $|\mathbf{E}|$ = electric field strength
E_r = Earth's radius = 6400km
$\mathbf{E}_T(\kappa)$ = "turbulent" electric field mapped to the ionosphere from the magnetosphere
$\mathbf{E_0}$ = constant electric field strength
E'_{x0} = Electric Field Strength, x-component
E'_{Z0} = Electric Field Strength, y-component
$E_{0\|}$ = the component of $\mathbf{E_0}$ in the direction parallel to $\mathbf{B_0}$
$E_{0\perp}$ = the component of $\mathbf{E_0}$ in the direction of $\nabla n_0 \times \mathbf{B_0}$
f = fading frequency
f_F = Fresnel frequency,
F_{R1} = radius of the 1st Fresnel Zone
g = acceleration due to gravity (assumed constant).
GDI = Gradient Drift Instability
GPS = Global Positioning System
GNSS = Global Navigation Satellite System
h = altitude
h_{max} = "most unstable" altitude in the ionosphere
K = Boltzmann's constant
K-H = Kelvin-Helmholtz
k = wave number
$k_{\|}$ = wave number component in the direction parallel to $\mathbf{B_0}$
$k_{\perp}$ = wave number component in the direction perpendicular to $\mathbf{B_0}$

$k_L = 2\pi / L = 2\pi \frac{\nabla n_0}{n_0}$ = Longest wavelength of relevance to turbulence theory

L = Electron concentration gradient scale-length

M = mass of one ion

m = mass of a particle

m = mass of one electron

NMR = Nuclear Magnetic Resonance

n = the total number of results

n_o= background ion concentration

n_1 = perturbation ion concentration

n_a = electron concentration, region a

n_b = electron concentration, region a

n_e = electron concentration

n_n = neutral concentration

n_i = ion concentration

P = received power

P = probability of the observed number of positive results

P_{SD} = Power Spectral Density,

p = the probability of an individual result being positive (assumed = 0.5)

q = charge of a particle

R = GPS Satellite Earth concentric orbital radius = 26560/2 = 13280km

S_4 = Scintillation Index, normalized standard deviation of the received power

SSI/ES = Special Sensor for Ions and Electrons

TEC = Total Electron Concentration

T_e = electron temperature

T_i = ion-temperature

t = time

U = neutral wind velocity

u = Eastward neutral wind speed.

V_a = Plasma Velocity, zone a

V_b = Plasma Velocity, zone b

V_{ir} = the component of the vector sum of the satellite and irregularity velocities perpendicular to the direction of the radio wave propagation

v = velocity of a particle

v_{ex} = electron drift velocity, x-component

v_{ey} = electron drift velocity, y-component

$\mathbf{v}_{i0}$ = constant ion drift velocity

$\mathbf{v}_{i1}$ = perturbation ion drift velocity

v_{ix} = ion drift velocity, x-component

v_{iy} = ion drift velocity, y-component

$v_{\parallel}$ = $\mathbf{E} \times \mathbf{B}$ drift velocity component parallel to ∇n_0

$v_{\perp}$ = Perpendicular drift velocity (whole plasma)

x = the number of positive results

β = a constant of proportionality

γ = instability growth rate

γ = sum of a series of growth rate values

γ_{GD} = Gradient Drift Instability growth-rate

γ_{KH} = Kelvin-Helmholtz growth-rate

$\gamma_{m(k)}$ = turbulent mixing growth-rate (wavelength-specific)

γ_{RT} = Rayleigh –Taylor Instability growth rate

γ_{T} = Small-scale turbulence growth-rate

$\Delta \mathbf{V}$ = change in velocity across a shear

θ = elevation angle of a GPS satellite, as seen from a ground based receiver

λ = wavelength

μ_0 = permeability of free space.

ν_{ei} = the electron-ion collision rate

ν_{en} = electron-neutral collision frequency

ν_{in} = ion-neutral collision rate

$\varphi_T(k)$ = turbulence growth rate for any given wavenumber, k

ρ = slope of a power-law spectrum

ρ_a = mass density of a plasma, zone a

ρ_b = mass density of a plasma, zone b

σ_ϕ = Scintillation Index, “sigma – phi”.

Ω_{Ci} = ion-gyro-frequency

Ω_{Ce} = electron gyro-frequency.

ω = angular frequency.

Chapter 1: Introduction to the Ionosphere

1.1 The Ionosphere

The ionosphere exists in the altitude range of approximately 90-600km above the surface of the Earth. It is made up of free electrons and heavy ions scattered amongst the neutral molecules of the atmosphere, forming a weakly ionised plasma. This is not the kind of plasma found in fusion reactor experiments, where the entire gas is ionised. The ionosphere is only about 1% ionised even where it is at its peak of electron concentration (the number of free electrons per unit volume) [*McNamara*, 1991].

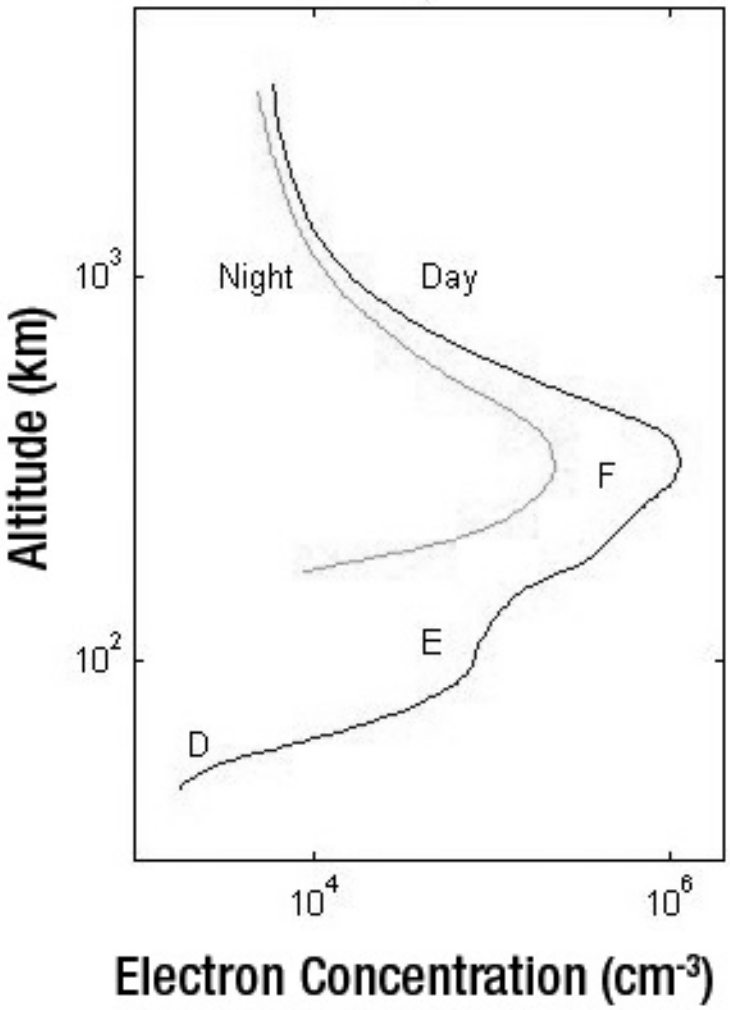

Fig.1.1: Typical Mid-latitude Electron Concentration Profile of the Ionosphere, Day and Night

The ionisation occurs when neutral molecules absorb extreme ultra-violet light or x-rays from the sun, causing an electron to be ejected and thus creating an electron-ion pair. Random collisions eventually lead any given electron to re-combine with an ion, returning them to a neutral state via a series of chemical reactions. These neutralisation reactions are diverse, usually multi-step processes and can involve numerous species

present at ionospheric altitudes [*Hargreaves*, 1992; *McNamara*, 1991]. Hence there is a balance of creation and dissipation of plasma in the ionosphere during daylight hours. At night no creation takes place and only dissipation occurs, however an appreciable charged layer always remains at dawn as the collision rate is not sufficient to allow for the re-combination of all the ion-electron pairs.

The ionosphere is divided into three bands, the D, E and F layers, in order of increasing altitude. The F layer is sub-divided into the F_1 and F_2 layers. Diurnal variations of these layers exist. Only the F_2 layer can be observed at all times, day or night. The E-layer, present in daylight as a distinct layer, ceases to be visible as such on profiles such as that shown in fig.1.1 [*McNamara*, 1991]. The electron concentration drops by two orders of magnitude after sunset and the profile appears smooth (see fig.1.1) [*Hunsucker*, 2003]. A phenomenon called Sporadic E can occur at night at high latitudes, giving rise to an E_S-layer, where the subscript indicates the sporadic nature of the layer. E_S-layers are localised clouds of electrons with higher concentrations than the background at the altitude of their formation. Sporadic E also occurs at mid and low latitudes but is rarely observed at night [*Hunsucker*, 2003]. The D-layer, which strongly absorbs radio waves during the day, re-combines at night to the extent of not being visible at all on night-time profiles (see fig.1.1) [*Hunsucker*, 2003].

The ionosphere can be divided up into five regions by latitude. These are:
A. The Equatorial Region. The band around the globe that would just contain both Equatorial Anomalies is the equatorial region. The Equatorial Anomalies are found at approximately $\pm$ 10° to 20° of geomagnetic latitude and are the regions of highest electron concentration in the ionosphere [*Hargreaves*, 1992]. (See fig.1.2.)

B. The two polar regions made up of the polar caps and the auroral ovals. The low-latitude edges of the auroral ovals form the boundaries between the polar regions and the mid-latitude regions. The auroral ovals are the regions where the aurora are most prevalent and they surround the polar caps. (See fig.1.2.)

C. The two mid-latitude bands occupy the space between the Polar Regions and the Equatorial Region (See fig.1.2.).

The ionosphere displays a rich diversity of phenomena of intrinsic scientific interest and is also of supreme importance in the fields of radio communications and navigation. For example, over the horizon radio links would be impossible without use of repeaters, if not for the conducting layer of the ionosphere reflecting signals back toward the Earth. Some ionospheric phenomena, however, can also degrade signals that pass through the ionosphere, with negative consequences for the accuracy of Global Navigation Satellite Systems (GNSS), such as the Global Positioning System (GPS).

An outline of some of the most significant ionospheric phenomena in each geographical region of the ionosphere is given in the next three sections.

1.2 The Equatorial Region

The equatorial region, also known as the low-latitude region, extends from the geomagnetic equator to the Equatorial Anomaly (also sometimes referred to as the Appleton Anomaly, after its discover, Edward V. Appleton). The equatorial anomaly consists of the regions of highest free electron concentration observed anywhere in the Earth's ionosphere. The anomaly crests (where the anomalies are most intense) are normally quoted as being 10º to 20º of latitude either side of the geomagnetic equator and varies daily [*Hargreaves*, 1992]. Within this range of latitudes, the single most significant phenomenon is the Fountain Effect which is the cause of the Equatorial Anomaly. The Fountain Effect is caused by the interaction of ionospheric plasma with electric fields and the Earth's magnetic field as detailed below.

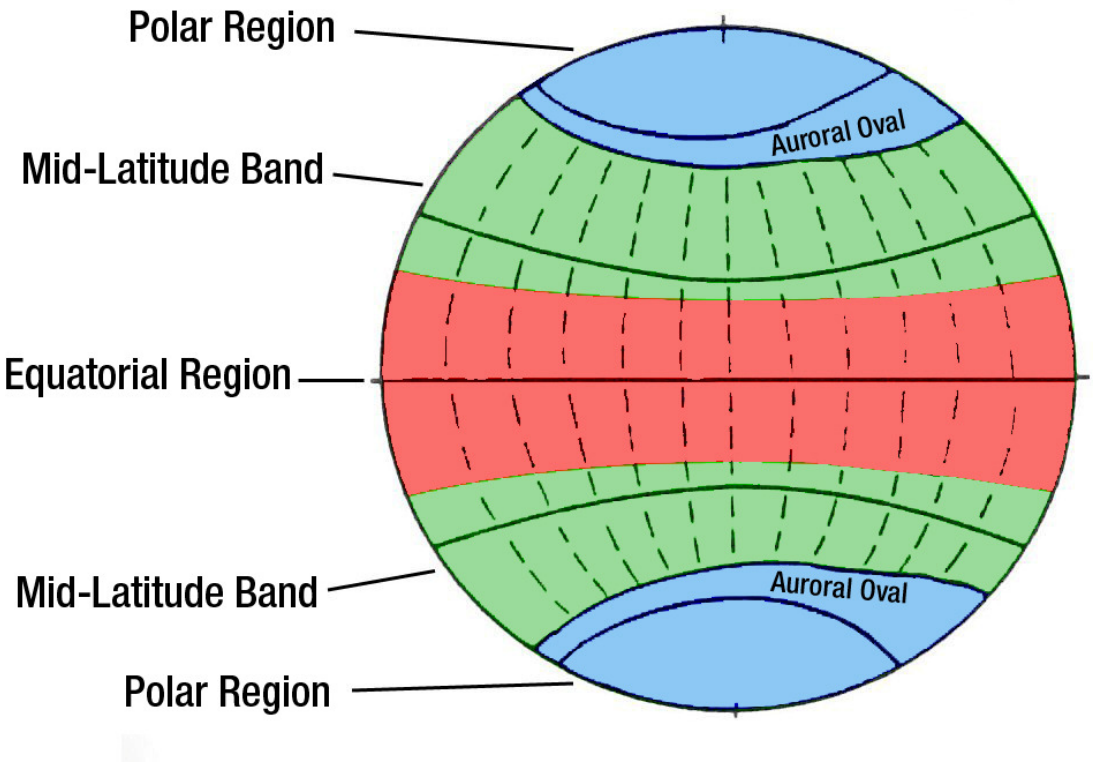

Fig.1.2: Regions of the ionosphere.

An electric field in the same horizontal plane as the magnetic field will cause a plasma to drift perpendicular to both as demonstrated below. The following argument is based on that of [*Chen*, 1984].

The equation of motion for a single charged particle is

$$m\frac{d\mathbf{v}}{dt}=q(\mathbf{E}+\mathbf{v}\times\mathbf{B}), \qquad (1.1)$$

where
v = velocity
q = charge on the particle
E = electric field
B = magnetic field

m = mass of the particle
t = time.

If **E** = 0 then the motion will be circular about **B**. The number of times per second that a charged particle rotates in a uniform magnetic field is called the gyro-frequency. If **E** > 0 there will still be circular motion about **B**, but also an additional motion perpendicular to the plane of **B** and **E**. This component can be found by solving $\mathbf{E} + \mathbf{v} \times \mathbf{B} = 0$ (i.e. ignoring time varying components of **v** and dividing by q).

Taking the cross product of this gives

$$\mathbf{B} \times \mathbf{E} + (\mathbf{B} \times (\mathbf{v} \times \mathbf{B})) = 0 . \qquad (1.2)$$

Re-arranging and expanding gives

$$\mathbf{E} \times \mathbf{B} = \mathbf{B} \times (\mathbf{v} \times \mathbf{B}) = \mathbf{v}(\mathbf{B}.\mathbf{B}) - \mathbf{B}(\mathbf{v}.\mathbf{B}) = \mathbf{v}B^2 - \mathbf{B}(\mathbf{v}.\mathbf{B}) \qquad (1.3)$$

Looking only for components perpendicular to the plane of **B** and **E**, the final term on the right of eqn.(1.3) is zero and we are left with

$$v_{\perp} = \mathbf{E} \times \mathbf{B}/B^2 , \qquad (1.4)$$

where $v_{\perp}$ is the velocity component perpendicular to both the electric and magnetic fields. It is important to note that this component of velocity represents a drift that is independent of charge and mass – electrons and positive ions will drift in the same direction at the same speed. This result is known as the "$\mathbf{E} \times \mathbf{B}$ drift".

1.2.1 The E-Region Dynamo

The Earth generates its own magnetic field, which can be approximated as by dipole field (see fig.1.3). At the geomagnetic equator, the Earth's magnetic field is, by definition, horizontal.

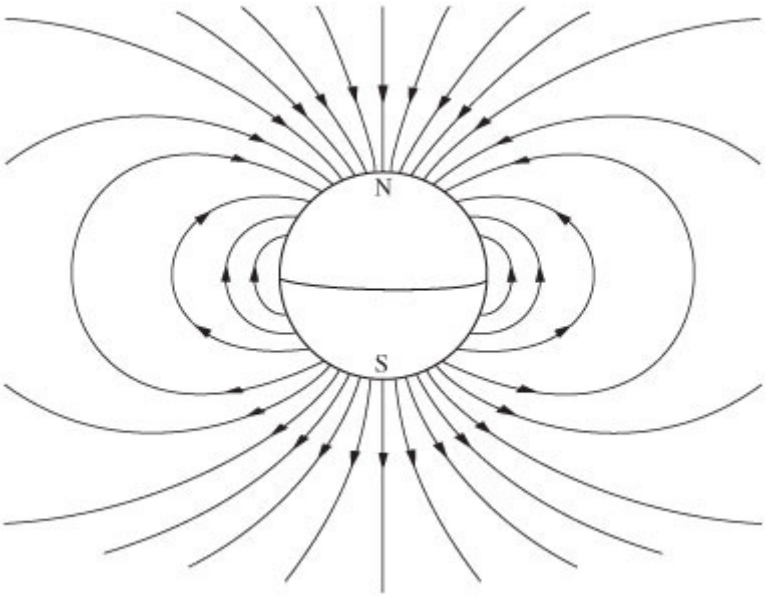

Figure 1.3: The Earth's magnetic field approximated as an ideal dipole field. The magnetic field is horizontal at the equator. The Geo-magnetic Equator is defined as the line on the earth's surface along which the Earth's magnetic field is locally horizontal.

There is also a naturally occurring horizontal electric field, which combines with the Earth's magnetic field to cause a vertical $\mathbf{E} \times \mathbf{B}$ drift in the manner described in the previous section. This electric field is, in ultimate origin, generated by tidal motion of the neutral atmosphere. At Equatorial latitudes and E-Region altitudes, the diurnal solar heating mode dominates other atmospheric tides and drives a phenomenon known as the "E-Region dynamo." (The lower atmosphere has been heated and the tide propagates to these altitudes.) Since the ionosphere is just a weakly ionised component of the thermosphere, collisions between wind–driven neutral particles and charged particles take place. An otherwise stationary uncharged particle would be accelerated to the neutral wind velocity by random collisions, but this is not necessarily the case for charged particles. Charged particles are constrained from moving readily in directions not parallel to the magnetic field, as described in the previous section. Furthermore the direction of drift of electrons will be different from that of positive ions and a charge separation will occur in the plasma, creating the observed electric fields. This is because the response of each type of particle is dependent on its gyro-frequency and collision rate with other particles. The gyro-frequency (the rate at which a particle rotates around a magnetic field line) is dependent on mass and is therefore different for electrons and ions. The greatest difference in direction of drift of ions and electrons creates the strongest electric field and this occurs at a particular range of collision rates (corresponding to altitudes in the ionosphere). This range is 75-120km.

Because of the direction of flow of the thermospheric winds in each hemisphere, the night time hemisphere's electric field is westward and the day time hemisphere's electric field is eastward. Thus the ionosphere at the geomagnetic equator is subject to an upward drift during the daylight hours and a downward drift during darkness.

1.2.2 The F-Region Dynamo

There is an anomalous period immediately after sunset during which the F-layer continues to rise. This short (less than 1 hour) period is known as the "pre-reversal enhancement" as the eastward electric field and hence vertical $\mathbf{E} \times \mathbf{B}$ drift are greatest at this time, just before the electric field reverses direction. Because darkness has fallen, the E-Region Dynamo cannot be responsible for the pre-reversal enhancement. Instead the F-Region Dynamo takes over. The F-Region Dynamo is caused by in-situ solar heating; the thermosphere in daylight is hotter than the night-time thermosphere because of direct absorption of sunlight. This causes a wind to blow from the day side of the dusk terminator to the night side and, in a similar fashion to the E-Region Dynamo, it causes a charge separation in the plasma. An electric field results from the charge separation. These two dynamo processes are like two voltaic cells with different internal resistances – if both are in the same circuit, the current will be drawn from the cell with the lesser internal resistance. During daylight hours the lower resistance of the E-Layer means that the F-Layer Dynamo is masked. In darkness the re-combination of the E-layer is much faster than that of the F-layer and so the layer with the least resistance becomes the F-layer.

Immediately after sunset, the F-layer Dynamo dominates. It is believed that the horizontal component of the F-layer Dynamo electric field is responsible for the pre-reversal enhancement [*Kelley*, 1989].

Since the electric field and Earth's magnetic field are perpendicular at the geomagnetic equator, an $\mathbf{E}\times\mathbf{B}$ drift occurs there, driving the plasma upward during the day and downward at night after the pre-reversal enhancement caused by the F-layer Dynamo.

There are other forces operating on the plasma in the same region; these are gravitational and diffusive in character and tend to oppose any upward $\mathbf{E}\times\mathbf{B}$ drift. There will be a height at which these forces balance. Having reached stalemate in vertical motion the plasma will still be trying to equalize the pressure gradient created by moving relatively concentrated plasma to greater heights where it is surrounded by lower concentration plasma. This can only be achieved by horizontal motion: The magnetic force resists diffusion in any direction perpendicular to the magnetic field by causing circular motion around field lines. There is no such resistance parallel to magnetic field lines, so the rate of diffusion is preferentially high in these directions. Hence, by motion along magnetic field lines, plasma spreads north–south. As it moves away from the geomagnetic equator and the field lines start to dip toward the Earth's surface, so the plasma descends. Where it meets the locally generated plasma two crests of very high electron concentration form, thus generating the equatorial anomaly.

The image of plasma forced upward at a central location and spreading out and descending over a wide area conjures the analogy of a fountain of water and gives the Fountain Effect its name.

1.3 The Polar Regions

Many phenomena occur in the polar caps and auroral ovals. Two of the most significant, Precipitation and Convection, are mentioned here.

1.3.1 Precipitation

Precipitation refers to the process of energetic particles arriving from space in the Earth's atmosphere. It occurs throughout the polar regions but most intensely in the auroral ovals. See [*Hargreaves*, 1992; *Kelley*, 1989] for details of why this occurs preferentially in these locations. The incoming flux of electrons, via collisions with neutral particles, causes ionisation and heating in the ionosphere. Lower energy electrons tend to deposit their energy in the F-layer, higher energy ones in the E-layer [*Kelley*, 1989].

Precipitation is responsible for auroral arcs. These occur mainly in the E- and lower F-regions and are enhancements of electron concentration and, as the name indicates, are usually narrow, curved structures. Their shapes may be influenced by plasma transport processes [*Kelley*, 1989]. They are short lived and unstable in shape. Auroral arcs are the main cause of the visible aurora, emitting light as excited particles release energy.

1.3.2 Convection

A complex and variable plasma flow pattern exists in the Polar ionosphere, generated by electric fields having their origins in Earth's interaction with the solar wind and interplanetary magnetic field. Because there is no resistance to the motion of charged particles parallel to a magnetic field, these electric fields are carried along the geo-magnetic field. At ionospheric altitudes, the electric field will be in the polar regions. Because the Earth's magnetic field is almost vertical in the polar ionosphere, any locally horizontal component of these electric fields will cause $\mathbf{E}\times\mathbf{B}$ drifts that are horizontal. Plasma can be transported long distances by these drifts. The process of carrying electric fields along magnetic field lines so that the electric field distribution in one region is an image of that in another is called "electric field mapping". Under certain conditions a two-cell convection flow pattern is imposed in the polar cap ionosphere by this process. (See [*Hargreaves*, 1992; *Kelley*, 1989] for details.) A two-cell circulation pattern is illustrated in fig.1.4.

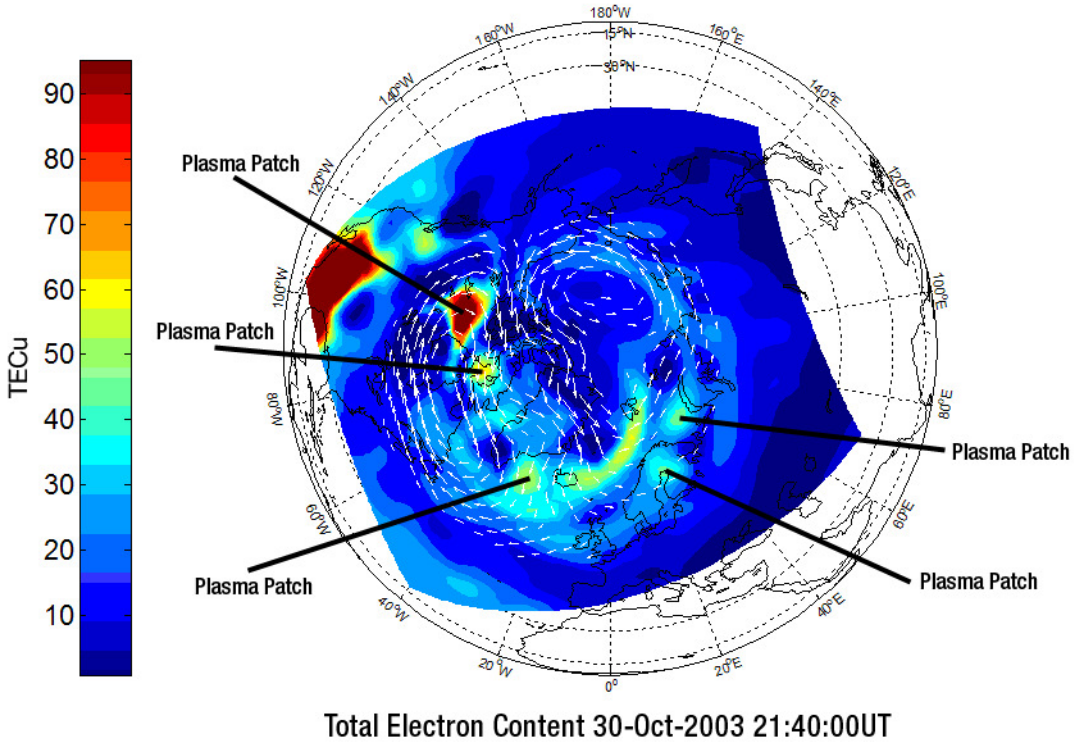

Fig.1.4: A tomographic reconstruction of the northern polar-cap ionosphere, showing a patch.

1.3.3 Polar Cap Patches

Large enhancements of electron concentration can appear in the night-time polar cap ionosphere. These are referred to as "patches" and have particularly steep electron concentration gradients at their edges because of the exceptionally low background level of ionisation they are surrounded by. (Note that similar formations found in the auroral ovals are referred to as "blobs".) Patches can travel for several hours in the polar cap before losing their identity, moving at the same speed as the background ionization in

whatever direction is dictated by the polar cap circulation pattern present at the time [*Hunsucker*, 2003].

Fig.1.4 shows a tomographic reconstruction of the total electron content of the ionosphere over the North Polar Region during an extreme magnetic storm. The arrows indicate the **E×B** drift direction as computed by the Weimer model [*Weimer*, 1995; 1996; 2001a; b; 2005a; 2005b]. A two cell convection system can be seen.

A number of other observational statements about patches are given by [*Hunsucker*, 2003]: Patches are roughly circular and between 200km and 1000km. The patches are smaller than the gaps between them. The degree of enhancement is between 2 and 10 times the ion concentration of the background. The electron concentration gradients at the edges of patches are on scales of kilometres up to 100 kilometres and are the same in all horizontal directions for any given patch. Patches appear when the Inter-planetary Magnetic Field (IMF) points southward. Patches can occur at any season of the year but are most prevalent during the winter. Patches form only when the geo-magnetic field is disturbed.

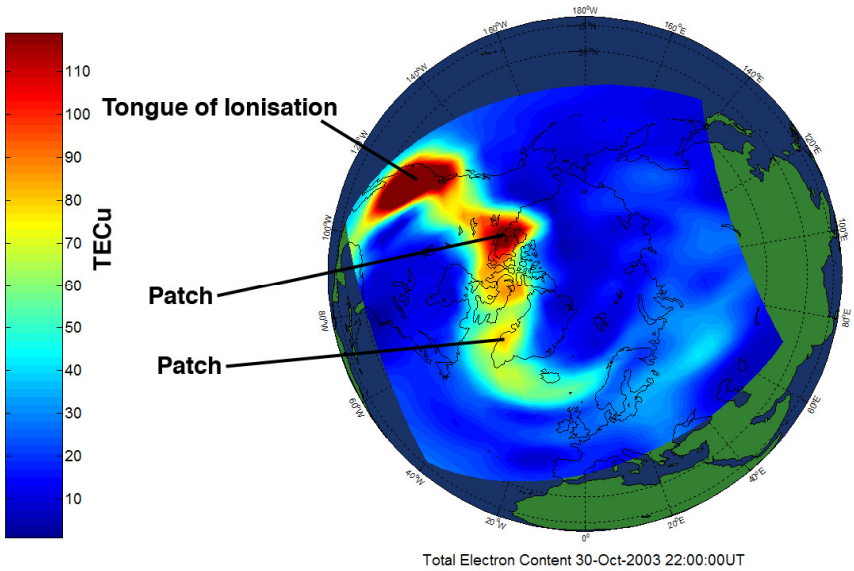

Fig.1.5: A tomographic reconstruction of the northern polar-cap ionosphere, showing a tongue of ionization and polar cap patches.

Recent results from ionospheric imaging such as that done for this thesis (see figs.1.4 and 1.5) and [*Spencer and Mitchell*, 2007] show a "tongue of ionisation" forming in the day side mid-latitude ionosphere and stretching into the auroral oval. As time goes on patches form as plasma is pulled into the polar cap by the **E×B** circulation pattern.

1.4 Mid-latitudes

In the mid-latitudes the motion of ionospheric plasma is dominated by winds in the neutral atmosphere and the Earth's magnetic field. The plasma would follow the neutral particles if the presence of the magnetic field did not create a resistance to

motion perpendicular to itself. One significant feature, however, cannot be explained in this way – the Mid-latitude Trough.

This phenomenon forms on the night-side, immediately equator-ward of the auroral ovals and consists of a region of the F-layer ionosphere with unusually low electron concentration. It is a few degrees of latitude wide and can stretch longitudinally across the night-side and sometimes into the day-side.

The Mid-latitude trough forms as plasma from the night-time polar cap enters a region that is convecting only slowly. The plasma has not seen sunlight for several hours so re-combination has reduced the electron concentration to low values. The slow convection means that it remains in the dark and higher concentration plasma is not being transported in from other regions. This situation is referred to as “Stagnation”.

Chapter 2: Research Background

2.1 Overview

The research presented in this thesis addresses the question "What mechanism dominates the process of generating irregularities in polar cap patches that cause GPS L1 band scintillation?" The approach taken to the question is novel, applying recent advances in ionospheric imaging techniques to simple theoretical results in order to create models of proposed irregularity generating mechanisms that develop in a 3-dimensional, time varying way, reliant as much as possible on observational data. Comparison of the model results gives an indication of which of the proposed mechanisms is dominant.

The remainder of this chapter gives the necessary background theory to understand the research presented in the subsequent chapters.

2.2 Scintillation

Ionospheric scintillation is an effect sometimes observed by users of radio receivers when a transmitted signal has passed through the ionosphere. The effect is that of rapid and unpredictable changes in the signal strength (wave amplitude or intensity) that were not present when the signal was transmitted. Astronomers use the term scintillation to refer to the shimmering of stars caused by the intervening atmosphere when observed from the Earth's surface. In ionospheric physics, the rapid, random fading and strengthening of received signals is termed "scintillation" in analogy with the astronomical phenomenon.

Merely passing through the ionosphere is not sufficient to cause scintillation. To undergo ionospheric scintillation, a radio signal must experience multiple random refractions across its wave-front. In normal circumstances this does not occur and to demonstrate this, the refractive properties of the ionosphere must be discussed. If the refractions were not random, the consequent amplitude changes would not be random either and could be used to reconstruct the state of the ionosphere; this would not be true scintillation.

The Refractive Index (RI) of a material indicates how much the phase velocity of a light, radio or other electromagnetic wave will change when it enters the material. The direction of propagation of the wave will change according to Snell's Law. The RI is itself determined by the permittivity of the material, which is defined as the linear response of the material to an imposed external electric field.

The Refractive Index (RI) of a material indicates the extent to which a light, radio or other electromagnetic wave is deflected from its path when it enters the material. It also indicates how much the phase velocity of the wave will change. The RI is itself determined by the permittivity of the material, which is defined as the linear response of the material to an imposed external electric field. The Refractive Index of the ionosphere is a dispersive medium for radio waves of the approximate frequency range 3-30 MHz. That is, the value of the RI is affected by the frequency of the wave

passing through the ionosphere. When this is taken into account it is found that the group velocity of a wave packet made up of a range of frequencies is slowed by the ionosphere [*Hargreaves*, 1992]. GPS L1 band signals are affected in just this way.

The Refractive Index of the ionosphere, at HF (high frequency) and greater radio frequencies, is principally affected by the free electron concentration. This is because the free electrons are the principal absorbers and re-radiators of radio waves. As the concentration of free electrons per unit volume increases, any incoming radiation is refracted to a greater degree. The more there are per unit volume, the more they refract the incoming radiation. Normally the ionosphere's electron concentration changes smoothly and slowly both with height and parallel to the Earth's surface [*McNamara*, 1991]. This means that the ionosphere's Refractive Index also changes smoothly in normal circumstances.

Because the Refractive Index varies slowly and smoothly in all directions, a radio wave traversing the ionosphere is continually refracted but, crucially, the entire wave-front is affected in exactly the same way. For scintillation to occur, the wave-front must encounter a region of the ionosphere that does not vary in this slow and smooth manner, which is defined as not changing significantly within the space of several wavelengths of the transmitted signal. Instead the wave-front must encounter a region of the ionosphere that exhibits random changes in Refractive Index across time and space on a scale less than that of several wavelengths. Each part of the wave-front is affected in a different way by the changes in speed and direction caused by these variations. Taking the simple view that the wave-front is made up of tiny wavelets (Huygens' Principle), once the wave has traversed the region of relatively rapid changes in Refractive Index and each wavelet is super-posed, the phase pattern of the wave has been distorted and, looking far enough away from the ionosphere, the intensity pattern has been randomised to some extent. This is scintillation.

Changes in Refractive Index imply changes in electron concentration. In order to see scintillation in a received signal, the signal must pass through a region of the ionosphere where the electron concentration varies randomly in both space and time such that the Refractive Index of the plasma changes significantly in the space of several wavelengths of the transmitted signal. These regions of relatively rapidly varying electron concentration and hence Refractive Index are known as "irregularities" in the ionosphere.

2.2.1 Scintillation Indices

It is often necessary to quantify the extent to which scintillation is occurring. Indices have been developed for this purpose and the two most commonly used indices are described here. One measures the severity of amplitude distortion or "fading" in the received signal, the other the extent of phase distortion introduced to the received signal.

The S_4 scintillation index is the most widely used measure of amplitude fading and is defined as:

$$S_4 = \frac{\sqrt{\left\langle \left(P - \langle P \rangle \right)^2 \right\rangle}}{\langle P \rangle} \qquad (2.1)$$

where P = received power and the symbols $\langle\rangle$ imply the mean value [*Hargreaves*, 1992]. S_4 can only take on values in the range 0 to 1.

Phase scintillation is most commonly measured by σ_ϕ, defined as:

$$\sigma_\phi^2 = \langle \phi^2 \rangle - \langle \phi \rangle^2 \qquad (2.2)$$

Again, $\langle\rangle$ implies the mean value. This can, in principle, take on any value. The length of time over which the mean is taken in eqn.(2.2) is of crucial importance. It must be short enough to be able to assume that the ray path between the satellite (which is moving) and the stationary receiver can be considered stationary. It should be long enough to give a statistically meaningful mean. These criteria conflict and care must be taken to achieve an appropriate compromise. In practice this means that no one length of time is appropriate for all situations [*Beach*, 2006].

2.2.2 Scintillation and Global Positioning System Signals

The Global Positioning System (GPS) is an example of a Global Navigation Satellite System (GNSS). A GNSS is a constellation of satellites that broadcast signals intended for use as a navigational aid. A receiver designed to pick up signals from the satellites can compute a location on the surface of the Earth by comparing a time code in the received signal with the time of arrival of the signal as measured by the receiver's own internal clock. In the case of GPS, to obtain an accurate location including an altitude, signals from four separate satellites are required. See [*Kaplan*, 1996] for details of how GNSS signals can be used for navigational purposes.

The GPS constellation transmits signals at the L1 (1575.42 MHz) and L2 (1227.60 MHz) bands. Specialized receivers are available, intended for the scientific community, that record the L1 band signal as received, complete with scintillation effects. Analysis of data from such receivers forms a very significant part of the work presented in this thesis. A description of the receiver model used is given in section 3.2.

The ionosphere is a dispersive medium i.e. its Refractive Index depends on the frequency of the signal being refracted. This means that signals at L1 and L2 bands travel at slightly different speeds for any particular electron concentration. The time difference between arrival of the L1 and L2 band signals can therefore be used to calculate the Total Electron Content (TEC) along the path of the signal. TEC is defined as the total number of electrons per square metre calculated by integrating along the length of a ray path. One TEC unit (TECu) is 10^{16} electrons/m^2. This ability to establish the TEC along a ray path is of crucial importance in ionospheric imaging algorithms.

2.2.3 1st Fresnel Zone Calculations

What size do irregularities have to be to directly cause amplitude scintillation in GPS signals? One way of tackling this question is by using the concept of Fresnel Zones. To do this, it is assumed that the effect of ionospheric irregularities can be modelled by an infinitely thin sheet at a given altitude which introduces the space and time varying phase distortions to a signal transmitted through it. Such a model is a "thin

phase screen" model. The model discussed here is applicable when the effect of a single irregularity is not severe – severe being defined as introducing a phase change greater than one radian [*Hargreaves*, 1992]. Using this model it is possible to calculate the radius of the 1st Fresnel Zone, the minimum distance a wave has to travel before phase distortions can cause amplitude scintillation. See [*Hargreaves*, 1992] for full details. Ionospheric irregularities must be smaller than the 1st Fresnel Zone radius if they are to affect the transmitted signal.

Since the research reported in this thesis uses scintillations observed in signals received from GPS broadcasts it is worth looking in some detail at what sizes of irregularities are directly involved in their generation. Taking the result for the size of the 1st Fresnel Zone from [*Hargreaves*, 1992] we have:

$$F_{R1} = \sqrt{\frac{DD'\lambda}{D+D'}} \tag{2.3}$$

where

F_{R1} = Radius of the 1st Fresnel Zone

D = the distance from the receiver to the thin phase screen

D' = the distance from the satellite to the thin phase screen

λ = wavelength of the signal = 0.19m = 0.00019km [*Kaplan*, 1996].

If the satellite is directly over the receiver and we know its orbital radius it is straight-forward to calculate F_{R1} for any given altitude of thin phase screen. However most of the time the satellite will be at some elevation angle $\theta<90^o$. It is of interest to see how F_{R1} varies with the elevation angle θ and in turn the implications for the sizes of irregularities that can cause amplitude scintillation on GPS transmissions. Redefining D and D' as the distances when $\theta=90^o$ and introducing the two distances,

A = the distance from the receiver to the thin phase screen, $0<\theta<90^o$

A' = the distance from the satellite to the thin phase screen, $0<\theta<90^o$,

the modified result is:

$$F_{R1}(\theta) = \sqrt{\frac{AA'\lambda}{A+A'}}\,. \tag{2.4}$$

The dependence of A and A' on θ is required in order to calculate the variations of F_{R1} for any given D. The value of D' for any given D, for a GPS satellite orbit, is also required.

Starting with the latter, assuming a spherical Earth with radius E_r = 6400km and a GPS satellite concentric orbital radius R = 26560 [*Kaplan*, 1996], then

$$D' = (R - E_r - D)$$

or

$$D' = (26560\text{-}6400\text{-}D) = (20160\text{-}D)\ \text{km}.$$

See fig.2.3 for a diagram showing the geometry of the problem.

In order to work out the relationships between D, D', A, A' and θ it is easier to first work in terms of the angles ϕ and α, (see fig.2.1, below) then derive the relationships between θ, ϕ and α.

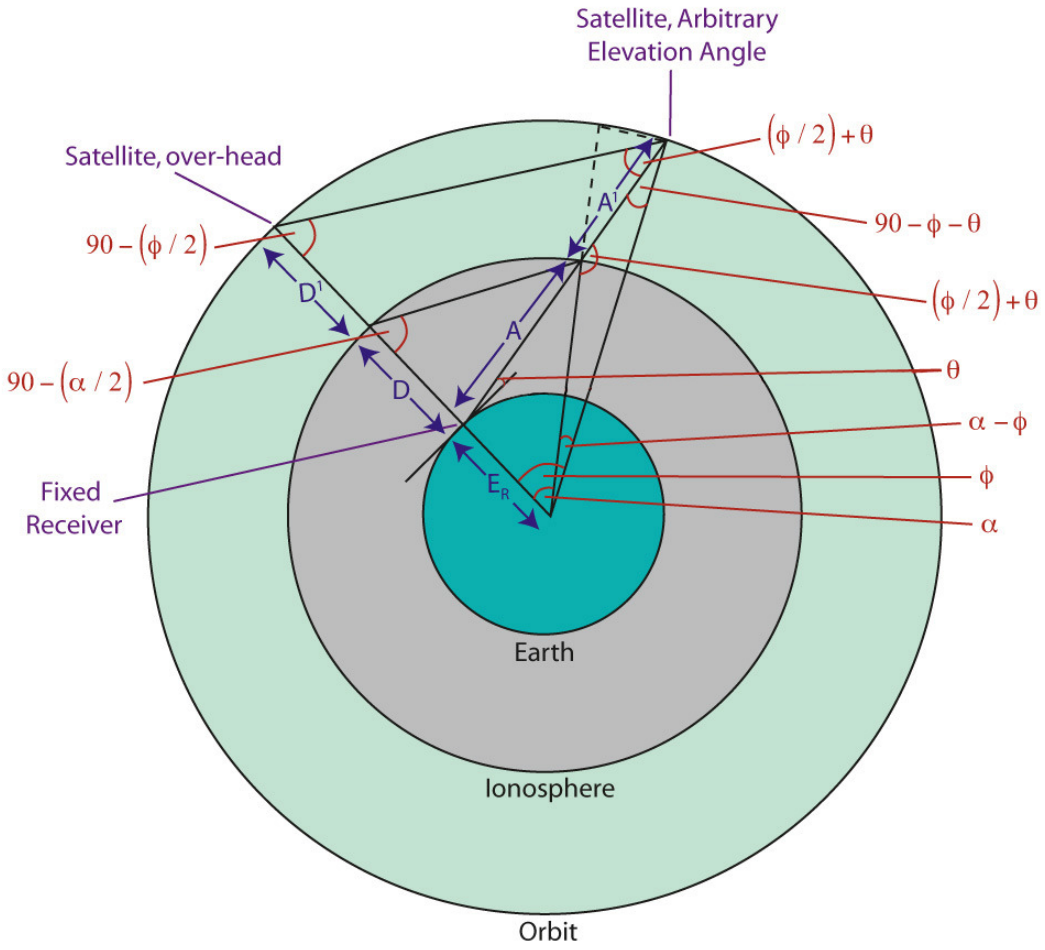

Fig.2.1: The geometry of a receiver and satellite, with the satellite directly over head and at an arbitrary elevation angle. (Not to scale.)

Applying the Cosine Rule gives

$$A^2 = E_R^2 + (E_R + D)^2 - 2E_R(E_R + D)\cos\alpha \qquad (2.5)$$

and

$$A^2 = D^2 + 2(E_R + D)^2(1-\cos\alpha) - 2D\sqrt{2(E_R + D)^2(1-\cos\alpha)}\sin(\alpha/2). \qquad (2.6)$$

By equivalent triangles,

$$(A+A')^2 = (E_R + D)^2 + (E_R + D+D')^2 - 2(E_R + D)(E_R + D+D')\cos\phi \qquad (2.7)$$

and

$$\begin{aligned}(A+A')^2 &= (D+D')^2 + 2(E_R + D+D')^2(1-\cos\phi) \\ &-2(D+D')\sqrt{2(E_R + D+D')^2(1-\cos\phi)}\sin(\phi/2)\end{aligned}. \qquad (2.8)$$

Applying the Cosine Rule twice more yields

$$A'^2 = (E_R + D)^2 + (E_R + D+D')^2 - 2(E_R + D)(E_R + D+D')\cos(\phi-\alpha) \qquad (2.9)$$

and

$$A'^2 = D'^2 + 2(E_R + D + D')\left[1 - \cos(\phi - \alpha)\right] - 2(D + D')^2 \sqrt{2(E_R + D + D')^2}\left[1 - \cos(\phi - \alpha)\right]^{1/2} \sin(\theta + \phi) \quad (2.10)$$

Moving on to make use of the Sine Rule:

$$\frac{A}{\sin\alpha} = \frac{E_R}{\sin(90 - \theta - \alpha)} = \frac{(E_R + D)}{\sin(90 + \theta)}.$$

This can be re-written as

$$\frac{A}{\sin\alpha} = \frac{E_R}{\cos(\theta + \alpha)} = \frac{(E_R + D)}{\cos\theta}. \quad (2.11)$$

Making use of the Sine Rule again:

$$\frac{A'}{\sin(\phi - \alpha)} = \frac{(E_R + D)}{\cos(\theta + \phi)} = \frac{(E_R + D + D')}{\cos\theta} \quad (2.12)$$

and

$$\frac{(A + A')}{\sin\phi} = \frac{(E_R + D)}{\cos(\theta + \phi)} = \frac{(E_R + D + D')}{\cos(\theta + \alpha)}. \quad (2.13)$$

The set of equations (2.5) to (2.13) will be used to determine the relationship between θ and ϕ and between θ and α as follows:

Eq.(2.5) = eq.(2.6) $\therefore$

$$E_R^2 + (E_R + D)^2 - 2E_R(E_R + D)\cos\alpha = D^2 + 2(E_R + D)^2(1 - \cos\alpha) - 2D\sqrt{2(E_R + D)^2(1 - \cos\alpha)}\sin(\alpha/2) \quad (2.14)$$

Taking all but the final term to the left hand side gives

$$E_R^2 + (E_R + D)^2 - 2E_R(E_R + D)\cos\alpha - D^2 - 2(E_R + D)^2(1 - \cos\alpha) = -2D\sqrt{2(E_R + D)^2(1 - \cos\alpha)}\sin(\alpha/2).$$

Collecting similar terms and re-arranging slightly:

$$E_R^2 - D^2 - (E_R + D)^2 + 2(E_R + D)(E_R + D - E_R)\cos\alpha = -2D\sqrt{2(E_R + D)^2(1 - \cos\alpha)}\sin(\alpha/2).$$

Factorising the first two terms and taking the term in $(E_R + D)$ outside the square root:

$$(E_R + D)(E_R - D) - (E_R + D)^2 + 2(E_R + D)(E_R + D - E_R)\cos\alpha = -2D(E_R + D)\sqrt{2(1 - \cos\alpha)}\sin(\alpha/2).$$

$\div$by $(E_R + D)$:

$$(E_R - D) - (E_R + D) + 2(E_R + D - E_R)\cos\alpha = -2D\sqrt{2(1 - \cos\alpha)}\sin(\alpha/2).$$

$\div$by $(-2D)$ and tidy up:

$$1 - \cos\alpha = \sqrt{2(1 - \cos\alpha)}\sin(\alpha/2).$$

Square both sides:

$$(1 - \cos\alpha)^2 = 2(1 - \cos\alpha)\sin^2(\alpha/2).$$

Dividing by $(1-\cos\alpha)$ and re-arranging gives the result:

$$2\sin^2(\alpha/2) = 1-\cos\alpha. \qquad (2.15)$$

Using an identical approach with equations (2.7) and (2.8) yields

$$2\sin^2(\phi/2) = 1-\cos\phi. \qquad (2.16)$$

A third time, using equations (2.9) and (2.10):

$$2\sin^2(\theta+\phi) = 1-\cos(\phi-\alpha). \qquad (2.17)$$

From equations (2.12) and (2.13):

$$\frac{(E_R+D)}{\cos(\theta+\phi)} = \frac{(E_R+D+D')}{\cos\theta} = \frac{(E_R+D+D')}{\cos(\theta+\alpha)}$$

Hence

$$\cos\theta = \cos(\theta+\alpha), \qquad (2.18)$$

but in general if $\cos\beta = \cos\delta$ then $\beta = 2n\pi \pm \delta$ where n is an integer $\therefore$

$$\theta = 2n\pi + \theta + \alpha \text{ or } \theta = 2n\pi - \theta - \alpha.$$

Only the second case has a non-trivial solution:

Let n=1: $\theta = 2\pi - \theta - \alpha$ or, re-arranging;

$$\alpha = 2\pi - 2\theta. \qquad (2.19)$$

Hence $\cos\alpha = \cos(2\pi - 2\theta) = \cos 2\pi.\cos 2\theta + \sin 2\pi.\sin 2\theta$

$\Rightarrow$ $\cos\alpha = \cos 2\theta.$ (2.20)

Let n=2: $\theta = 4\pi - \theta - \alpha$ or, re-arranging; $\alpha = 4\pi - 2\theta$.

Hence $\cos\alpha = \cos(4\pi - 2\theta) = \cos 2\theta$, so the value of n is not relevant – the result will always be $\cos\alpha = \cos(2n\pi - 2\theta) = \cos 2\theta$.

Now substitute for α from eq.(2.19) in to eq.(2.17):

$$2\sin^2(\theta+\phi) = 1-\cos(\phi-2\pi+2\theta)$$

$\Rightarrow$ $2\sin^2(\theta+\phi) = 1-\cos(\phi+2\theta).\cos(-2\pi) + \sin(\phi+2\theta).\sin(-2\pi)$

$\Rightarrow$

$$2\sin^2(\theta+\phi) = 1-\cos(\phi+2\theta). \qquad (2.21)$$

But in general $2\sin^2\delta = 1-\cos(2\delta)$ $\therefore$ eq.(2.21) becomes

$$1-\cos(2\theta+2\phi) = 1-\cos(\phi+2\theta) \text{ or } \cos(2\theta+2\phi) = \cos(\phi+2\theta).$$

Again using the fact that in general if $\cos\beta = \cos\delta$ then $\beta = 2n\pi \pm \delta$ where n is an integer:

$2\theta + 2\phi = 2n\pi + \phi + 2\theta$ or $2\theta + 2\phi = 2n\pi - \phi - 2\theta$.

Only the right hand one of this pair has non-trivial solutions, $3\phi = 2n\pi - 4\theta$ and of these, the unique solutions are for n = 1, 2 and 4:

$$\phi = \frac{2}{3}(\pi - 2\theta), \frac{4}{3}(\pi - \theta), \frac{4}{3}(2\pi - \theta).$$

Leading to

$$\cos\phi = \cos\left[\frac{2}{3}(\pi - 2\theta)\right], \cos\left[\frac{4}{3}(\pi - \theta)\right], \cos\left[\frac{4}{3}(2\pi - \theta)\right]. \qquad (2.22)$$

The first and third of these solutions are identical when evaluated, so only the first two will be used henceforth. Equations (2.20) and (2.22) show how the angles ϕ and α relate to θ. Next substitute eq.(2.20) into eq.(2.5) and eq.(2.22) into eq.(2.7):

$$A^2 = E_R^2 + (E_R + D)^2 - 2E_R(E_R + D)\cos 2\theta \qquad (2.23)$$

$$(A+A')^2 = (E_R + D)^2 + (E_R + D + D')^2 - 2(E_R + D)(E_R + D + D')\cos\phi$$
$$\text{where } \phi = \frac{2}{3}(\pi - 2\theta), \frac{4}{3}(\pi - \theta). \qquad (2.24)$$

Going back to the original eq.(2.4), and re-arranging slightly yields

$$\frac{F_{R1}^2}{\lambda} = \frac{AA'}{A+A'} = \frac{A(A+A') - A^2}{A+A'} = A - \frac{A^2}{(A+A')}$$

which is the same as saying,

$$\frac{F_{R1}^2}{\lambda} = \sqrt{\text{eq.}(2.23)} - \frac{\text{eq.}(2.23)}{\sqrt{\text{eq.}(2.24)}}. \qquad (2.25)$$

At this point it is easier to progress by plotting the curves, taking extreme values we can see the "envelope" of F_{R1} (see figs.2.4 and 2.5, below).

We can take the following figures (to two significant figures) from these graphs:
For a phase screen at a very low 200km:

$F_{R1}(Max) = 1200\text{m}$

$F_{R1}(Min) = 190\text{m}$

For a phase screen at an extremely high 1000km:

$F_{R1}(Max) = 1200\text{m}$

$F_{R1}(Min) = 420\text{m}$

Examination of the figures for the two extremes of phase-screen altitude given above shows a range of $F_{R1} = 190 \rightarrow 1200\text{m}$. Since several irregularities have to be fitted inside the 1st Fresnel Zone Radius, it is reasonable to conclude that the maximum size of irregularities that can directly cause amplitude scintillation at the GPS L1 frequency is of the order of 100s of metres.

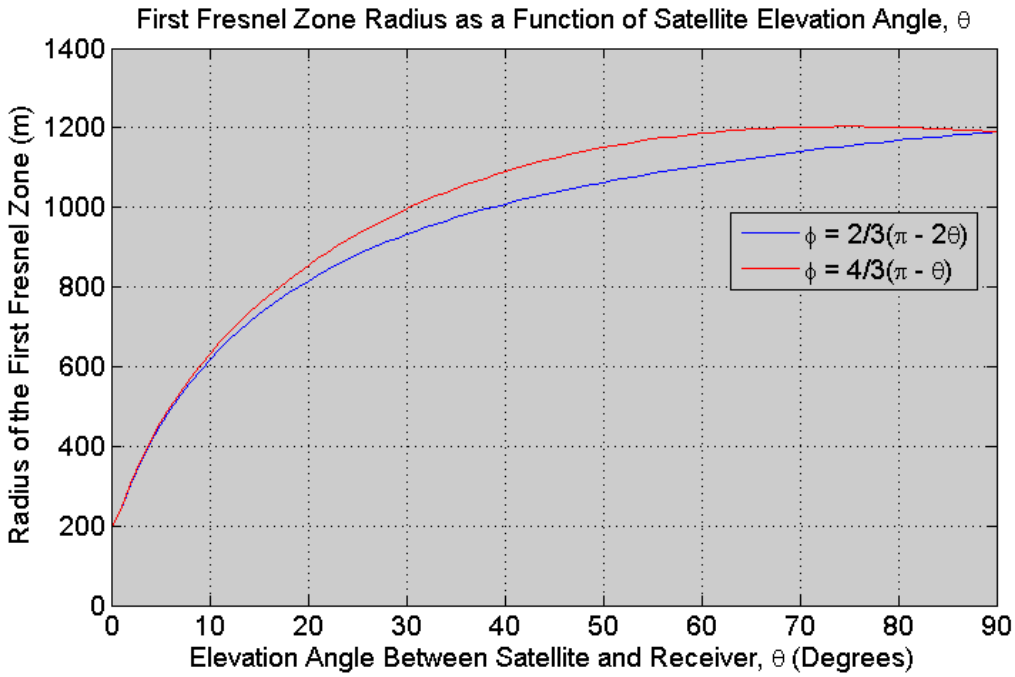

Fig.2.2: First Fresnel Zone Radius as a function of Satellite Elevation Angle. Thin phase screen at 200km altitude.

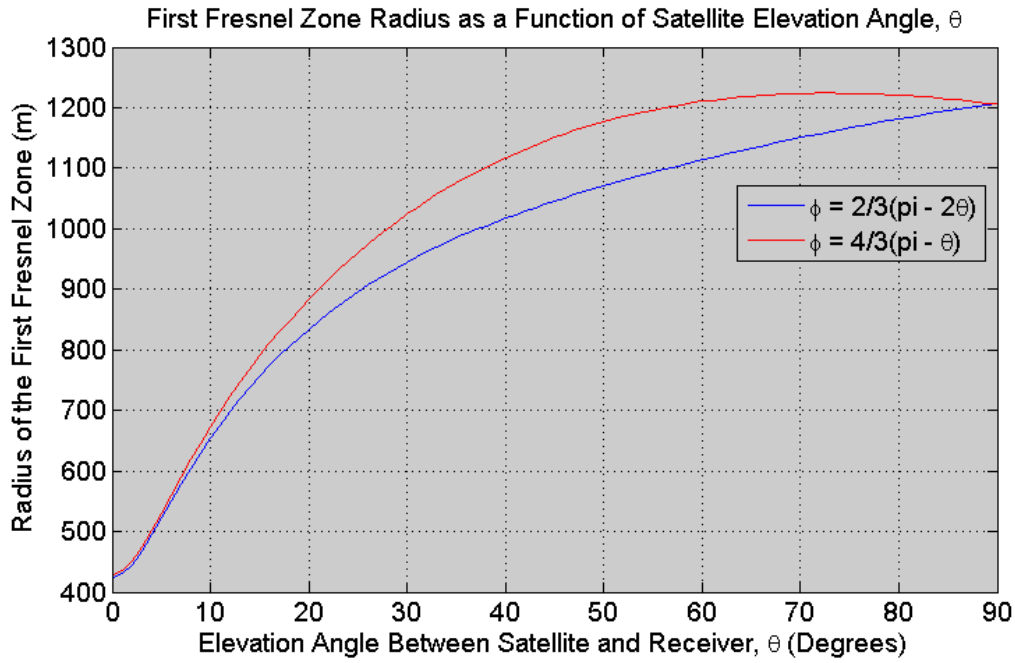

Fig.2.3: First Fresnel Zone Radius as a function of Satellite Elevation Angle. Thin phase screen at 1000km altitude.

2.2.4 Power-law Spectra and the Fresnel Frequency

Power Spectral Density is defined as power per unit frequency. When the power spectral density of the amplitude scintillations of a trans-ionospheric radio signal is plotted against the frequency of the scintillations (or fading frequency), on log-log

scales, an approximate relationship is revealed; the graph can be approximated by two straight lines that form an angle (see fig.2.4). The line to the left of the corner has approximately zero gradient. The line to the right of the corner has a slope, ρ.
In this region the relationship

$$P_{SD} = \beta f^{-\rho}, \tag{2.26}$$

where
P_{SD} = Power Spectral Density,
β = a constant of proportionality,
f = fading frequency and
ρ = slope of the spectrum,
is approximately correct. Since the spectrum obeys a power law, it is known as a power-law spectrum (often misleadingly abbreviated to "power spectrum"). The "corner" frequency, where this relationship first applies, is called the Fresnel frequency and is related to the radius of the First Fresnel Zone in the following way:

$$f_F = V_{ir} / F_{R1} \tag{2.27}$$

where
f_F = Fresnel frequency,
V_{ir} = the component of the vector sum of the satellite and irregularity velocities perpendicular to the direction of the radio wave propagation and
F_{R1} = the First Fresnel Zone radius.
ρ is found to range from 1 to 4, approximately [*Davies*, 1990].

If the same thin phase screen model is applied at various altitudes but is otherwise unchanged, the Fresnel frequency will show a dependence on the altitude of the screen because both V_{ir} and F_{R1} have an altitude dependence. For any given satellite elevation angle, F_{R1} can be calculated from eq.(2.25); it increases as the altitude of the phase screen increases. V_{ir} increases from the perpendicular component of the satellite velocity, up to some maximum value then starts to decrease again as altitude increases. This is because of the variation in the plasma velocity with altitude, which is initially zero, rising to a maximum then decreasing again. Overall, f_F will increase with altitude of the phase screen until the maximum of V_{ir} is reached as the change in V_{ir} with height is much faster than the change in F_{R1}. (See figs.2.2 and 2.3 for variations in F_{R1}.) The local plasma velocity perpendicular to the signal ray path will start at zero and rise to up to approximately 2000km/s at its maximum, according to the Weimer Model used in this research. (See section 2.5 and the following references for more details.) [*Weimer*, 1995; 1996; 2001a; b; 2005a; 2005b; *Winglee et al.*, 1997]

Taking these factors into account shows that as the phase screen altitude increases, the Fresnel frequency and hence the corner in the graph shown in fig.2.4, will move to the right. This in turn means that the total energy of the fading spectrum decreases – the amplitude scintillation becomes more severe. This decrease in severity will then start to reverse as the phase screen altitude goes beyond the altitude of maximum V_{ir}. The reason that the total energy in the power law spectrum decreases as the Fresnel frequency increases is that the sloped part of the spectrum remains unchanged: A higher Fresnel frequency then meets the sloped part of the graph to the

right of a lower Fresnel Frequency, but is lower on the vertical axis. The flat part of the spectrum is hence at a lower power density and the area under the graph as a whole is smaller, representing a drop in the total energy.

The same graph plotted for phase scintillations also shows a power-law spectrum but there is no Fresnel frequency evident. This is because there is no First Fresnel Zone effect for the phase scintillations. This means that the PSD graph for phase scintillations does not vary with the altitude of the thin phase screen.

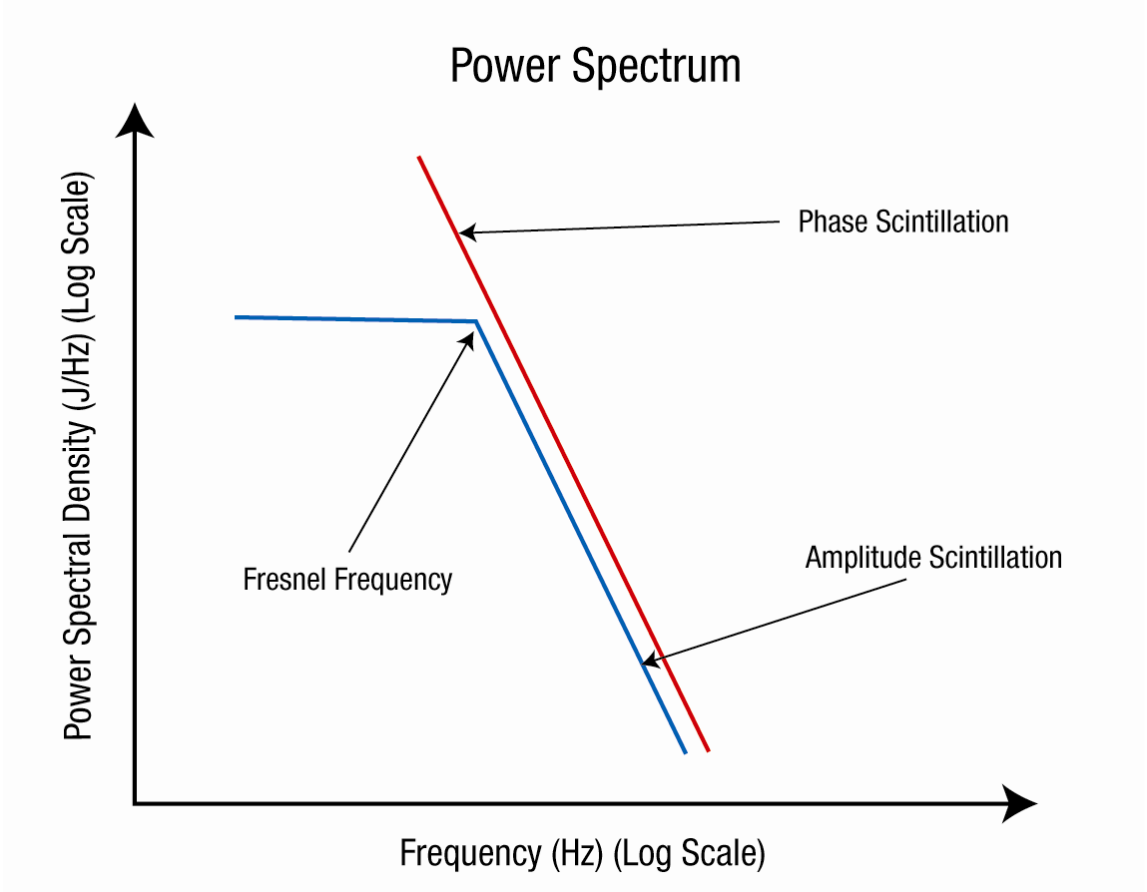

Fig.2.4: Idealised power-law spectra for amplitude and phase scintillation of a GPS L1 band signal.

2.3 Polar Cap Scintillation Phenomena

Polar cap patches maintain their identities for several hours and can be hundreds of kilometres in extent. They are closely correlated with scintillating radio signals [*Chaturvedi et al.*, 1994; *Coley and Heelis*, 1995; *Gondarenko and Guzdar*, 1999; 2001; *Gondarenko et al.*, 2003; *Gondarenko and Guzdar*, 2004a; b; *Gondarenko et al.*, 2005; *Gondarenko*, 2006a; b; *Kersley et al.*, 1989; *Kivanc and Heelis*, 1997; *Sojka et al.*, 1998].

Various mechanisms for generating irregularities in plasma patches have been put forward. The most studied is the Gradient Drift Instability (GDI) [*Chaturvedi et al.*, 1994; *Gondarenko and Guzdar*, 1999; 2001; *Gondarenko et al.*, 2003; *Gondarenko and Guzdar*, 2004a; b; *Gondarenko*, 2006a; b; *Kersley et al.*, 1989; *Sojka et al.*, 1998].

Turbulence has been put forward as a competing mechanism [*Huba et al.*, 1985; *Kelley*, 1989; *Kintner and Seyler*, 1985; *Zvezdin and Fridman*, 1992]. The Kelvin-Helmholtz Instability has been studied as a secondary process occurring when the GDI is operating and creating smaller scale irregularities [*Keskinen et al.*, 1988]. Each of these mechanisms is discussed in more detail below.

2.3.1 The Gradient Drift Instability

This phenomenon has been referred to by a number of names; Gradient Drift Waves, The Generalised $\mathbf{E}\times\mathbf{B}$ Instability and the Gradient Drift Instability are all the same physical process [*Kelley*, 1989]. Here, the name Gradient Drift Instability (GDI) is used for the process as this appears to be the recent convention when discussing plasma patches. Occasionally the irregularities themselves are referred to as Gradient Drift Waves.

The GDI requires a horizontal electron concentration gradient, a vertical or near vertical magnetic field and an electric field perpendicular to both. Steep horizontal electron concentration gradients exist on the edges of polar cap patches. The Earth's magnetic field is nearly vertical in the polar cap. The electric field that generates the polar-cap convection pattern may have a significant component perpendicular to both the electron concentration gradient of a patch and the Earth's magnetic field. The GDI is therefore an excellent candidate for causing irregularities to form on patches, as all the required conditions can be met.

An initial perturbation must exist if an irregularity is to form. Furthermore, the direction of (or at least a component of) the $\mathbf{E}\times\mathbf{B}$ drift must be parallel to the direction of the electron concentration gradient: If the $\mathbf{E}\times\mathbf{B}$ drift is anti-parallel to the electron concentration gradient, the enhanced side of the perturbation will be moving into an enhanced background where at some point it will cease to be a perturbation at all and the wave will not grow further. (Similarly the depleted part of the perturbation will move into a depleted background.) (See fig.2.9.)

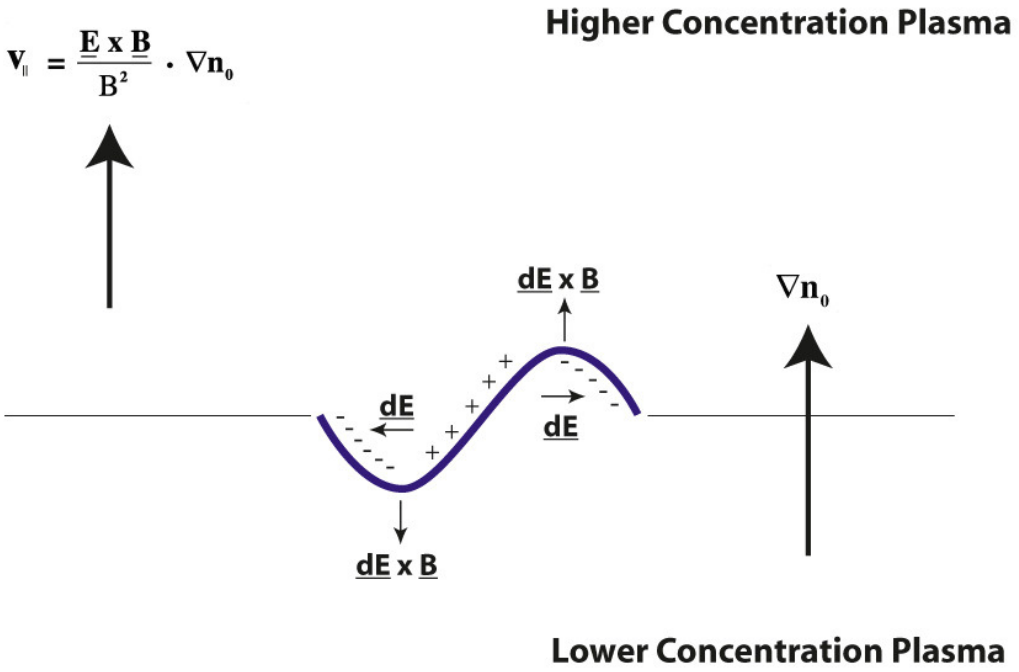

Fig.2.5: Geometry and Dynamics of the Gradient Drift Instability. (After [*Kelley*, 1989]). The wave shown is in an unstable configuration.

The GDI has been studied by observational, theoretical and modelling approaches [*Chaturvedi et al.*, 1994; *Gondarenko and Guzdar*, 1999; 2001; 2004b; *Guzdar et al.*, 1998; *Kivanc and Heelis*, 1997; *Sojka et al.*, 2000]. It is tailor-made for explaining the observation that the trailing edges of some patches are more prone to scintillation, as the geometry of the $\mathbf{E} \times \mathbf{B}$ drift and electron concentration gradient will be at its most unstable on that part of the patch. (See Section 2.3, Growth Rates, for a more detailed discussion.) Some success has been obtained in showing that longer wavelength modes of the GDI are more stable than shorter ones, overcoming the initial objections that the GDI would destroy a convecting plasma patch in much less than the several hours over which they are observed to maintain a well-defined identity [*Gondarenko and Guzdar*, 2004b].

[*Kelley*, 1989] indicates that the GDI can produce irregularities over the whole range 100s of metres up to ~30km. However, modelling work seems to favour approximately 1km irregularities [*Chaturvedi et al.*, 1994; *Gondarenko and Guzdar*, 1999; 2001; *Gondarenko et al.*, 2003; *Gondarenko and Guzdar*, 2004a; b]. From this we can see that the GDI may produce GPS L1 band scintillations directly (see the results of the 1st Fresnel Zone analysis in section 2.1.3) but is more likely to be the start of a cascade process creating shorter wavelength irregularities.

2.3.2 Turbulence

Laminar flow cannot cause irregularities to form in the ionosphere: even though the velocity may vary across a region of plasma, there is no significant mixing, so a gradient in electron concentration remains smooth. Turbulent flow has a tendency to mix the fluid; in ionospheric plasma it can generate irregularities [*Kelley*, 1989].

If an electric field that varies in time in a random fashion is applied, then the ensuing **E×B** drift of the ionospheric plasma will be random, too. Although the action of neutral molecules in the atmosphere does reduce the electric field mapped from the magnetosphere, the approximation that magnetic field lines represent equipotential lines is good enough for many purposes [*Hargreaves*, 1992]. Such an electric field from space communicated to the ionosphere would induce an **E×B** drift if it has a component perpendicular to **B** as discussed in the previous section.

Plasma in the magnetosphere flows in a turbulent fashion almost all the time and that turbulence creates a varying electric field as the inverse of an **E×B** drift [*Kelley*, 1989]. This field is mapped to the ionosphere in the polar regions, rather than at lower latitudes, because of the magnetic field geometry and generates the polar cap flow pattern. Because it varies with the turbulent motion of the magnetospheric plasma, the motion it induces in the F- and E-layer plasma is also turbulent, thus generating irregularities. The variations in the electric field can be viewed as modulations of a D.C. signal. The D.C. component generates the large scale flow pattern and is involved with the GDI process. The modulations cause turbulence. The spatial wavelengths of the irregularities are determined by the spatial wavelengths of the electric field modulations and can thus occur at all scales contained in the electric field spectrum up to a maximum determined by the gradient scale-length of the electron concentration itself (see sections 2.31 and 2.3.2). This means that turbulence occurring in a plasma patch will generate irregularities on scales at and below the maximum necessary for amplitude scintillation of a GPS L1 band signal to be detected by a ground-based receiver (see section 2.1.3).

Turbulent mixing cannot create irregularities in the absence of an electron-concentration gradient and is therefore a process that competes with the GDI: This effect will only be important if the GDI is absent or less intense. This final point is important in relation to polar-cap patches and is considered in more detail in the section on Growth Rates, below. The question, "Does the GDI or turbulent mixing dominate irregularity formation in polar-cap patches?" is one question this research attempts to answer.

2.3.3 The Kelvin-Helmholtz Instability

This process can be witnessed on a beach; waves on the surface of the water are generated by the wind, via the Kelvin-Helmholtz Instability. There is no requirement for two different fluids in order to generate this type of wave, as long as there is a "velocity shear" present within the single fluid. A velocity shear consists of a boundary surface between regions with different flow velocities. The two regions could be flowing in different directions or in the same direction at different speeds.

In the Polar Regions two scenarios can be imagined where velocity shears exist in ionospheric plasma: The first is at the boundaries of convecting patches, where patch-plasma is moving at some **E×B** drift velocity and the background plasma is stationary or moving at a neutral wind velocity. The second is where irregularities in electron concentration are moving past each other in opposite directions, driven by some other mechanism of generation. An example of where this might occur is on the boundaries of lower and higher concentration regions developing by the Gradient Drift Instability (see fig.2.10). One model of the evolution of convecting plasma patches shows exactly this

two step process of the GDI leading to Kelvin-Helmholtz Waves [*Gondarenko and Guzdar*, 1999].

This mechanism is one way that Gradient Drift Waves too large to directly cause GPS L1 band scintillations (km or greater scale wavelengths) could nevertheless be the progenitors of irregularities small enough to be responsible for such scintillations. The K-H waves themselves are smaller in scale than the originating Gradient Drift Waves, but they in turn generate gradients in electron concentration that have approximately the same orientation as the larger-scale edge-of-patch gradient. This means that the GDI might occur at a scale below that of the K-H waves. In turn, even smaller K-H waves might then form. This type of process is called a frequency-cascade, as each instability leads to a further instability operating at a shorter wavelength (higher spatial frequency) than itself. Since patches are up to 200km across, the largest scale Gradient Drift Waves to form would be of the order of 10s of kilometres and a cascade of only two orders of magnitude would yield irregularities small enough for amplitude scintillation on the GPS L1 band to be observable by a ground-based receiver. (See section 2.1.3.)

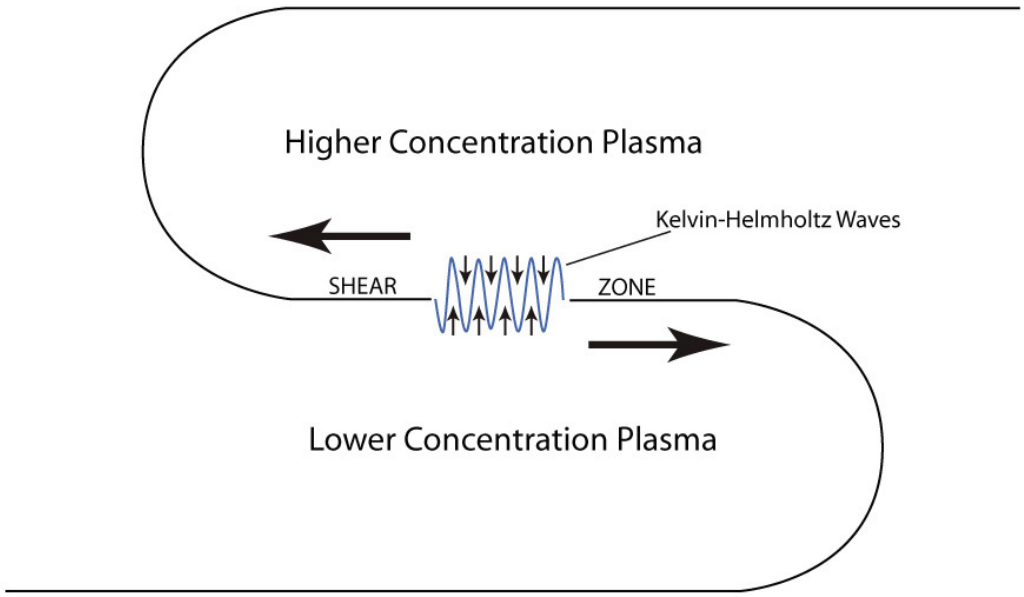

Fig.2.6: A Gradient Drift Wave developing subsidiary waves via the Kelvin-Helmholtz Instability. The arrows show the direction of motion of plasma.

2.4 Growth Rates

In order to determine what conditions allow a perturbation to grow and what conditions suppress it, it is usual to try to derive a "growth rate" for the waves. Sometimes a threshold or other condition for unstable growth is apparent when this is done. Growth rate calculations form a crucial aspect of the research presented in later chapters so they are considered in some detail here.

By definition unstable perturbations grow proportionally to $e^{\gamma t}$ where t = time and γ is defined as the growth rate [*Hargreaves*, 1992]. The growth rate γ for the one dimensional Rayleigh – Taylor Instability is given below. In this example a constant magnetic field is attempting to hold up a plasma against the force of gravity.

The only unstable solutions are those with an imaginary component; these are defined by

$$-g\frac{(\partial n_0/\partial x)}{n_0} > \frac{1}{4}k^2 v_{i0}^2 \qquad (2.26)$$

and the growth rate is defined as the imaginary part:

$$\gamma = \mathrm{Im}(\omega) \approx \left(-g\frac{(\partial n_0/\partial x)}{n_0}\right)^{1/2} \qquad (2.47)$$

where:
n_o= background ion concentration
g = acceleration due to gravity (assumed constant)
k = wavelength of the perturbation wave.
$\mathbf{v}_{i0}$ = constant ion drift velocity
(See Appendix 2 for a full derivation of eqns.(2.26) and (2.47).)

These two results are significant: eqn.(2.26) is an instability condition and eqn.(2.47) is the instability growth rate. Equation (2.26) states the circumstances in which we can expect unstable growth of perturbations; equation (2.47) indicates how fast those perturbations will grow.

Here g was defined as the acceleration due to gravity but nothing in the derivation relies on this; some force **g** has to be present and directed perpendicularly to both $\mathbf{B_0}$ and $\mathbf{v}_{i0}$, but the nature of this force is irrelevant to the result so long as it is constant. This means that driving forces other than gravity can give rise to very similar unstable behaviour if the relative geometry of the forces and fields is the same: The case of the ionospheric Gradient Drift Instability is an important example with gravity replaced by an electric field and the resulting irregularities propagating horizontally rather than vertically.

A very idealised and simple case has been used in the above analysis but it can be extended in many ways; use of two or three dimensions, inclusion of an electron drift, $v_{e0} \neq 0$ or inclusion of sources or sinks of plasma in the Continuity Equation, for example. The nature of $\frac{\partial n_0}{\partial x}$ has not been examined at all in the above analysis and could influence the growth rate in profound ways depending on what form it takes. Generalised to a greater number of dimensions, $\frac{\partial n_0}{\partial x} \rightarrow \frac{\nabla n_0}{n_0}$. This term appears in many growth rate equations.

In an ionospheric situation, many simplifying assumptions are very approximate at best or not valid at all, the geometry of the forces, fields and plasma may not be ideally simple and there may be more than one process competing to dominate the behaviour of the plasma. For example, the F-layer at the geo-magnetic equator may not be horizontal, thereby modifying the required component of ∇n_0 and the presence of a neutral wind in any region has the effect of modifying the applicable electric field ($\mathbf{E'} = \mathbf{E} + \mathbf{U} \times \mathbf{B_0}$, where $\mathbf{U}$ = neutral wind velocity, see [*Kelley*, 1989] for further details). The analysis above gives a flavour of how to acquire growth-rate equations from theory and the matter will be left there; the equations for various processes discussed later in this section will be merely presented and discussed, not derived, although reference will be made to source material where derivations can be found.

In the polar cap, patches may be influenced by the GDI and turbulence (see section 2.2, above). The dominant process could be found if the growth rate of each process could be specified for the prevailing conditions.

The remainder of this section discusses growth-rate equations of interest with regard to polar-cap patches, as these are crucial to the research presented later.

2.4.1 The Gradient Drift Instability

The instability condition $\mathbf{E} \times \mathbf{B} \cdot \nabla n_0 > 0$ states that there must be a component of plasma drift in the same direction as the electron concentration gradient if irregularities are to grow. Since the whole patch is drifting and the electron concentration gradient is horizontal, one would expect that the irregularities would preferentially initiate on the trailing half of the patch where this condition will be met. This does not exclude the possibility that once irregularities have started to form they penetrate into the leading half of the patch. Where $\mathbf{E} \times \mathbf{B} \cdot \nabla n_0$ is negative, the effect is reversed and fluctuations will tend to be damped out. This means that the leading half of a polar-cap patch will not initiate gradient drift waves. Assuming that no other scintillation generating processes were taking place on a patch, scintillation would first be detected on the farthest trailing edge of the patch and it would progress toward the front of the patch as time went on. Care has to be taken in regard to the definition of "trailing edge": From the two-cell pattern shown in fig.3.2 it can be seen that the velocity of a patch can vary in direction over time, so the "trailing edge" can be a different part of the patch at different times. The shape of the patch may also evolve as time goes on, also possibly affecting the definition of "trailing edge"[*Kivanc and Heelis*, 1997].

The simplest approach to calculating a GDI growth rate is a one-dimensional equation. With increasing sophistication and accuracy, two- and three-dimensional equations can be used, including more of the known behaviour of the high-latitude F-layer and its interaction with any E-layer that may be present.

As mentioned by [*Sojka et al.*, 1998], in a collisional plasma, the one-dimensional form is given by

$$\gamma_{GD} = \frac{v_{\parallel}}{L} \tag{2.28}$$

and in a collisionless or "inertial" plasma by

$$\gamma_{GD} = \left(\frac{v_{\parallel}}{L} \nu_{in} \right)^{1/2} \tag{2.29}$$

with

$$L = \frac{n_0}{\nabla n_0},$$

and where:

γ_{GD} = Gradient Drift Instability growth-rate

$v_{\parallel}$ = $\mathbf{E} \times \mathbf{B}$ drift velocity component parallel to ∇n_0

L = electron concentration gradient scale length

ν_{in} = ion-neutral collision rate

n_o= background ion concentration.

Note that ∇n_0 is taken in the horizontal plane only.

The version studied by [*Sojka et al.*, 1998] is the one for the inertial regime, eqn.(2.29): Substituting for L we see that $\gamma_{GD} = \left(v_{\parallel} \nu_{in} \frac{\nabla n_0}{n_0} \right)^{1/2}$ and this looks remarkably similar to eqn.(2.47) for the idealized one dimensional Rayleigh-Taylor Instability. This is no surprise as both come from a one dimensional analysis of instabilities that have different driving forces (**g, E**) but are otherwise identical in basic principle.

A salient feature of this equation is that it is independent of the wavelength of the initial perturbations. This is a significant weakness: Models of the GDI that have no wavelength dependence show the polar-cap patch losing its integrity as a separate entity in much less time than is observed in reality. This is because the long-wavelength irregularities tear the patch apart swiftly [*Gondarenko and Guzdar*, 2004b].

More detailed analyses exist [*Chaturvedi et al.*, 1994; *Gondarenko and Guzdar*, 2004b; *Kelley*, 1989] that include possible consequences of the presence of an E-layer as well as an F-layer, inhomogeneous conductivity of the whole ionosphere and a rate of decay of irregularities through diffusion. These analyses are of significance because they introduce a wavelength dependence that more nearly matches observations; that is they suppress long-wavelength irregularity growth rates, allowing a patch to maintain a stable identity over a period of hours as is observed for real polar-cap patches, whilst allowing for generation of shorter wavelength irregularities that lead directly or by cascade to scintillation.

2.4.2 Turbulence

Turbulent mixing is unlike any other irregularity generating process discussed in this document as it is not an instability of the plasma itself. Nevertheless, it would be useful to think of turbulence in terms directly comparable to those of plasma instabilities. In other words it is highly desirable to try to obtain a "growth rate", γ_T, that can be directly compared to other growth rates obtained above. In order to do this (following the argument in [*Kelley*, 1989]) we recognize that the electric field, $\mathbf{E_T}$, mapped to the ionosphere must be structured, i.e. a super-position of many wavelengths:

The growth rate must therefore be a function of these wavelengths, λ. We can define the growth-rate as,

$$\gamma_{m(k)} = \frac{E_{T(k)}}{B_0 L} \tag{2.30}$$

for any wavenumber, $k = \frac{2\pi}{\lambda}$, with the gradient scale-length, L, defined as $L = \frac{n_0}{\nabla n_0}$.

To get an equation independent of wavelength. γ_T is defined as,

$$\gamma_T = \left(\int_{\Delta k} \left[\gamma_{m(k)} \right]^2 dk \right)^{1/2}, \tag{2.31}$$

which is the root mean-square of $\gamma_{m(k)}$. Substituting eqn.(2.30) into eqn.(2.31) we find

$$\gamma_T = \frac{\left(\int_{\Delta k} \left[E_{T(k)} \right]^2 dk \right)^{1/2}}{B_0 L}. \tag{2.32}$$

This leaves open the question of what range, Δk, to use. Since wavelengths shorter than L are not important, the lower limit needs to be $k_L = 2\pi / L = 2\pi \frac{\nabla n_0}{n_0}$ and there is no upper limit i.e. $k = \infty$. Hence

$$\gamma_T = \frac{\left(\int_{K_L}^{\infty} \left[E_{T(\kappa)} \right]^2 dk \right)^{1/2}}{B_0 L} \tag{2.33}$$

In order to perform this integration knowledge of the exact nature of $\mathbf{E}_{T(\kappa)}$ is required. This would best be obtained from observation.

The only requirements for this turbulent mixing are an electron concentration gradient and an electric field mapped to the ionosphere from the magnetosphere. No particular orientation of gradient is required, unlike the GDI case, as it is assumed that the direction of the fluctuations is random and therefore perpendicular to the electron concentration gradient some of the time.

2.4.3 Kelvin-Helmholtz Waves

This type of wave occurs at the boundary between volumes of fluid travelling at different velocities – a velocity shear. In the polar cap patch case the fluid is a plasma and the Earth's magnetic field provides a damping force on the formation of K-H Waves, specifically, the magnetic tension. This can be understood by analogy to the wind-water situation. The surface tension of the water is attempting to pull the surface into the lowest area (and hence energy) configuration. This force must be overcome if waves are to form. In the case of a magneto-plasma the magnetic field is attempting to maintain the lowest energy configuration and must be overcome for waves to form. It seems highly likely that a threshold for the formation of K-H Waves exists because of this. Referring to fig.2.10 it can be seen that if K-H Waves are to cascade from the shear zones of Gradient Drift Waves, the magnetic field and the plane of the velocity interface (not the direction of the shear) must be parallel to each other. In this configuration, the appropriate dispersion relation is given by [*Mikhailovskii*, 1992] as:

$$\left(\omega - kV_a\right)^2 + \left(\omega - kV_b\right)^2 - 2kC_A^2 = 0 \tag{2.34}$$

where:

V_a = plasma velocity, zone a

V_b = plasma velocity, zone b

C_A = the Alfven Speed:

$$C_A^2 = \frac{1}{4\mu_0}\left(\frac{1}{\rho_a} + \frac{1}{\rho_b}\right)\left(B_a^2 + B_b^2\right) \tag{2.35}$$

where:

ρ_a = mass density of the plasma, zone a

ρ_b = mass density of the plasma, zone b

B_a = magnetic field strength, zone a

B_b = magnetic field strength, zone b

μ_0 = permeability of free space.

Across a velocity shear in a polar-cap patch B_0 can be considered not to change significantly $\therefore$ eqn.(2.35) becomes

$$C_A^2 = \frac{1}{4\mu_0}\left(\frac{1}{\rho_a} + \frac{1}{\rho_b}\right)\left(2B_0^2\right). \tag{2.36}$$

In order to derive a growth-rate, γ_{KH}, for Kelvin-Helmholtz Waves eqn. (2.34) must be for solved ω and the imaginary part taken: First expand all the terms in eqn. (2.34) and collect similar ones:

$$2\omega^2 - 2k\left(V_a + V_b\right) + k^2\left(V_a + V_b\right) - 2k^2\left(V_a^2 + V_b^2 - 2C_A^2\right) = 0 .$$

This is a quadratic so now solve for ω using $\omega = \frac{-b \pm \sqrt{b^2 - 4ac}}{2a}$:

$$\omega = \frac{2k\left(V_a + V_b\right) \pm \sqrt{4k^2\left(V_a + V_b\right)^2 - 8k^2\left(V_a^2 + V_b^2 - 2C_A^2\right)}}{4}. \tag{2.37}$$

For unstable growth there must be an imaginary component of ω, or in other words the square root in eqn.(2.37) must be negative. Hence

$$4k^2\left(V_a + V_b\right)^2 \le 8k^2\left(V_a^2 + V_b^2 - 2C_A^2\right)$$

for instability. Expanding both sides and collecting terms yields

$$0 \le V_a^2 + V_b^2 - 2V_a^2V_b^2 - 4C_A^2,$$

or, re-arranging,

$$4C_A^2 \le \left(V_a - V_b\right)^2.$$

Taking the square-root of both sides leaves us with

$$2C_A \le \left(V_a - V_b\right). \tag{2.38}$$

Eqn.(2.38) is the condition necessary for unstable growth of K-H Waves that was anticipated.

Next, defining the growth-rate, γ_{KH}, as the imaginary part of the solution for ω, given by eqn.(2.37):

$$\gamma_{KH} = \frac{\left[4k^2\left(V_a + V_b\right)^2 - 8k^2\left(V_a^2 + V_b^2 - 2C_A^2\right)\right]^{1/2}}{4} \tag{2.39}$$

which can be simplified to

$$\gamma_{KH} = k\left[\frac{1}{4}\left(V_a + V_b\right)^2 - \frac{1}{2}\left(V_a^2 + V_b^2 - 2C_A^2\right)\right]^{1/2}$$

$\Rightarrow$

$$\gamma_{KH} = \frac{k}{2}\left[\left(V_a + V_b\right)^2 - 2\left(V_a^2 + V_b^2 - 2C_A^2\right)\right]^{1/2} \tag{2.40}$$

Comparing eqns.(2.38) and (2.40) it can be seen that the instability condition is independent of wavelength but the growth-rate is quicker for shorter wavelengths.

This analysis has assumed a step change in both velocity and plasma density across an infinitesimal boundary and would have to be modified if gradients in either were present, as is likely in the case of polar cap patches.

2.5 Imaging

To obtain values for n_0 and ∇n_0 3-dimensional, time varying images of the free electron concentration of the ionosphere are required.

Ionospheric imaging is the process of reconstructing a view or "image" of the state of the ionosphere from observational data. A number of types of algorithm have been developed to this end and are discussed in detail in [*Kunitsyn*, 2003]. A review of ionospheric imaging giving a snapshot of the current state of the art and possibilities for future developments and applications is given by [*Bust and Mitchell*, 2008]. Only a brief overview of the nature of the problem is given here, along with a brief discussion of the particular imaging algorithm used in the research presented here. For further details, see the references already cited and [*Spencer and Mitchell*, 2007].

Current ionospheric imaging algorithms attempt to reconstruct the plasma distribution in the ionosphere (in terms of electron concentration) in fully global scope, accounting for three spatial dimensions and time evolution. This is done by using calculations of ray path TEC from data collected by globally distributed GPS receivers and occasionally other sources of TEC data such as ionosondes. The basic idea is to use the known TEC values along the ray paths between receivers and GPS satellites to solve for the electron concentration everywhere, using the approach of tomography.

In true tomography, such as is applied in medical imaging by CAT and NMR scanners, a very large number of ray paths are generated by moving the source and receiver. These are mapped onto a grid and the tomographic algorithm solves for each element of the grid with a low error because multiple ray paths traverse each element. In

the ionospheric case, such a number and distribution of ray-paths does not exist as the number of GPS receivers required is utterly impractical. This means that in general there is not one unique, lowest error, solution for any given ionospheric imaging problem.

In order to overcome this, ionospheric imaging algorithms rely on models of typical ionospheric behaviour to constrain the image solutions to ones realistic for the ionosphere. When imaging the polar regions, particular problems arise because structures such as plasma patches can be moving very rapidly. One approach to dealing with such structures is to "forecast" the motion using a model of the convective motion of the plasma, then generate another ionospheric image as normal and apply a Kalman Filter to decide how the ultimate solution should be weighted between the data and model based reconstructions.

Since this research is confined to the northern polar cap, an algorithm specifically designed for imaging the region was chosen. This algorithm, Multi-Instrument Data Assimilation System 2.0 (MIDAS 2.0) uses the Kalman filter approach described in the previous section. See [*Spencer and Mitchell*, 2007] for a full description of the algorithm.

Chapter 3: Modelling the GDI Growth Rate

3.1 Introduction

The overall aim of this Thesis is to elucidate the relative importance of different mechanisms of generating scintillation at the GPS L1 band frequency in the northern polar region on the Earth's ionosphere. The initial aspect of the research was to develop a model of the Gradient Drift Instability growth rate (γ_{GD}) based upon the ionospheric imaging algorithm, Multi-Instrument Data Assimilation System 2.0 (MIDAS 2.0). The values of γ_{GD} are used to determine mean amplitudes for Gradient Drift Waves. The extent of the correlation between these mean amplitudes and the scintillation indices, S_4 and σ_ϕ is then determined. This is done for several geo-magnetic storm periods, as detailed later.

The model consists of implementing a calculation of the equation

$$\gamma_{GD} = \left(v_{\|} \nu_{in} \frac{\nabla n_e}{n_e} \right)^{1/2}, \qquad (3.1)$$

where,

$v_{\|} = \mathbf{E} \times \mathbf{B}$ drift velocity component parallel to ∇n_0,

ν_{in} = ion-neutral collision rate,

n_e = background electron concentration.

This must be done in such a manner that γ_{GD} is known, across all three spatial dimensions, as it varies in time, for the duration of the storm analysed. MIDAS 2.0 is particularly well suited for this as its output consists of three three-dimensional matrices that represent the volume of the ionosphere that is being imaged. Each element of a matrix represents a voxel volume of the ionosphere. Output consists of one matrix, the elements of which are values of electron concentration and two matrices, the elements of which are perpendicular components of electric field strength. This means that, in eqn.(3.1), n_e is known and both ∇n_e and $v_{\|}$ can be calculated directly from the MIDAS 2.0 results. The drift velocities are calculated from the output of the Weimer Model of the polar-cap electric field [*Eriksson et al.*, 2002; *Picone et al.*, 2002; *Weimer*, 1995; 1996; 2001a; b; 2005a; 2005b; *Winglee et al.*, 1997]. The Weimer Model is a statistical model and is used by MIDAS 2.0 to aid the imaging of fast moving plasma structures. MIDAS 2.0 itself deploys a Kalman Filter to determine the extent to which it should rely on the Weimer Model or assimilated observational data when calculating the final reconstruction of the ionosphere [*Bust and Mitchell*, 2008; *Spencer and Mitchell*, 2007]. In the studies presented here, GPS receiver data is the only type of observational data assimilated by MIDAS 2.0. The algorithm is flexible in terms of the exact definition of the grid of voxels used and the time interval between sequential images of the ionosphere.

The remaining parameter in eqn.(3.1), ν_{in}, is calculated using the Mass Spectrometer Incoherent Scatter (MSIS) model of the neutral atmosphere [*Picone et al.*, 2002] and the Chapman Equation:

$$\nu_{in} = \left(2.6\times10^{-9}\right)\left(n_n + n_i\right) A^{-1/2} \qquad (3.2)$$

where

ν_{in} = ion-neutral collision rate,

n_n = neutral concentration,

n_i = ion concentration,

A = mean molecular weight of the ions and neutral species,

w = $2.6\text{x}10^{-9}$ $kg^{1/2}m^3s^{-1}$ (a constant).

The MSIS model gives results for the composition and density of the neutral atmosphere as it varies with altitude, latitude, longitude and time, so n_n and A can be calculated directly from its output, if the ions are assumed all to be O^+. (At F-layer altitudes the principal donator of free electrons is atomic oxygen [*Hargreaves*, 1992]. At other altitudes this assumption is less accurate, but in the night-time polar cap almost all the ionisation will be in the F-region.) It is assumed that the quasi-neutral approximation applies throughout the ionosphere, so the ion concentration is taken to be equal to the electron concentration and the values can be drawn directly from the MIDAS 2.0 results.

Using these data it is possible to calculate the GDI growth rate for every voxel in every MIDAS 2.0 spatial grid i.e. γ_{GD} is modelled through-out the whole volume of the reconstructed ionosphere and for the whole period under analysis, using the time interval and voxel spacing originally selected for the MIDAS 2.0 reconstructions. The area covered by the reconstructions used through-out all the research presented in this thesis is shown in fig.3.1. This region is imaged from 140km to 1660km in altitude.

The primary significance of this model of γ_{GD} when compared with other work on models of the Gradient Drift Instability such as [*Chaturvedi et al.*, 1994; *Gershman and Ponyatov*, 1988; *Gondarenko and Guzdar*, 1999; 2004a; b; *Kersley et al.*, 1989; *Sojka et al.*, 1998] is that it relies more heavily on observational data than any of them. In this research, the state of the ionosphere is defined by MIDAS 2.0 using observational data, influenced to some extent by models of the ionosphere. The drift velocity is based on model output. The ion-neutral collision rate is calculated from model output. Eqn.(3.1) for γ_{GD} is derived from Magneto-hydro-dynamic theory, rather than an empirical model. The calculated values of γ_{GD} are dominated by the observational data inputs and the Weimer drift velocities, since ν_{in} is the smallest factor in the equation. The fact that the results are more accurately based on the observed state of the ionosphere means that studies based on them should more accurately reflect the real behaviour of the ionosphere.

In this study the results for γ_{GD} were taken and used to calculate mean amplitudes for Gradient Drift Waves growing unstably in the ionosphere, as plasma moves via the polar cap circulation pattern. Scintillation observations (S_4 and σ_ϕ) taken from various GPS receivers stationed in the polar cap were then compared with the calculated mean

amplitudes by calculating correlation co-efficients. This was done for a number of geo-magnetic storm periods as detailed in the next section.

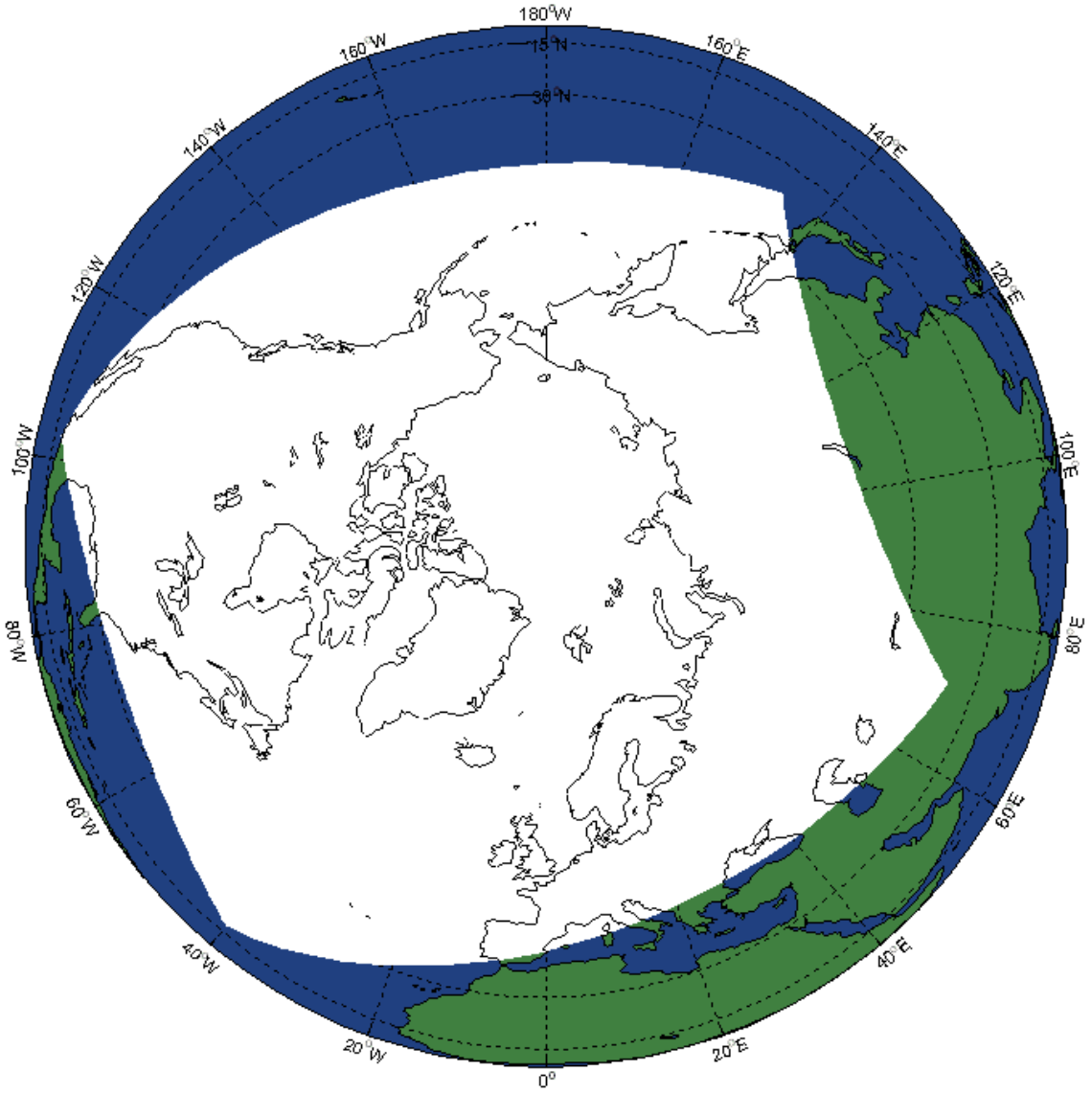

Fig.3.1: Geographical area covered by the MIDAS 2.0 grid. The area covered by the grid is shown in white.

3.2 Method

The spatial grid used by MIDAS 2.0 is divided into voxels by latitude, longitude and altitude surfaces. Because of the curvature of the earth, the resulting grid voxels are not of equal size. The separation of the dividing surfaces can be specified by the user. In all the studies in this thesis an altitude interval of 40km is used, giving the grid a depth of 38 voxels. The total altitude range is 140km to 1660km.

In order to discover the optimum latitude/longitude division, a number of grids were defined then the algorithm was run for each, using the same input data and time period: 09.00 UT, Oct 30th to 12.00 UT Oct 31st, 2003, inclusive. Ten minute time intervals between each reconstruction were used in all cases. All other parameters in the algorithm were set identically in each case. The resulting TEC map images were compared with independently supplied all-sky camera images for the same time period. The all-sky camera is stationed in Qaanaaq Greenland (76º, 32' lat. / 68º, 50' long.)

The latitude/longitude grid separations tested in this way were the 16 possible combinations of integer values 2 through 5, in degrees. The two combinations that gave TEC map images most similar to the all-sky camera images were 4º x 4º and 4º x 2º, latitude x longitude. Because the latter combination gives better resolution (i.e. a greater total number of voxels in the grid) whilst giving equally good results, a 4º x 2º, latitude x longitude grid definition was chosen for all subsequent research (see fig.3.2).

Having defined the optimum grid, MIDAS 2.0 was used to produce reconstructions of the ionosphere for a number of geo-magnetic storm periods, as detailed in table 3.1. Ten minute intervals between individual images were used through-out.

The storm periods selected (see table 3.1) were chosen simply to maximise the available scintillation receiver data.

Dates of Storms Used in this Analysis			
Storm 1	Storm 2	Storm 3	Storm 4
30th Oct 2003	24-28th July 2004	8-11th Nov 2004	14-16th May 2005

Table 3.1: Dates of Storms analysed in this thesis.

Values of γ_{GD} were subsequently calculated for each voxel of each reconstruction, by using eqns.(3.1) and (3.2) in the manner described in the Introduction.

Scintillation observations were recorded by GSV4004 GPS receivers. These receivers record data at a rate of 50Hz and subsequently calculate statistical data at 1 minute intervals. The receivers used in this and subsequent studies are stationed as shown in table 3.2 and fig.3.3. Data were not available from all stations at all times.

Locations of GPS Scintillation Receivers Used		
Station Name	Latitude (Geographic)	Longitude (Geographic)
Athabasca	54.7ºN	113.3ºW
Calgary	51.1°N	114.1°W
Kiruna	67.9ºN	20.4ºE
Sodankyla	67.4ºN	26.6ºE
Svarlbard	78.9ºN	11.9ºE
Tromso	69.6º N	19.2ºE
Yellowknife	62.5°N	114.5ºW

Table 3.2: Locations of GPS scintillation receivers, data from which are used in this thesis.

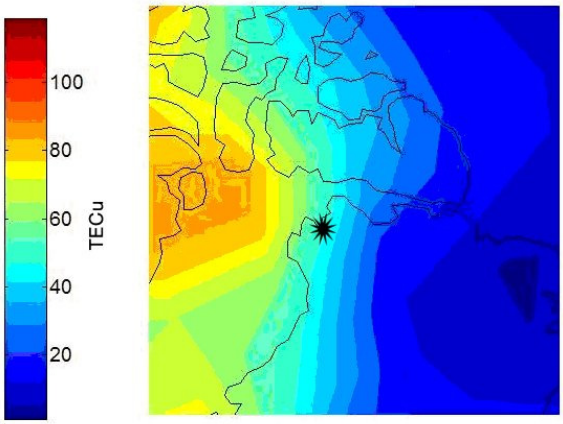

Fig.3.2a: 4º x 2º, latitude x longitude TEC map, 22.00 30th October, 2003

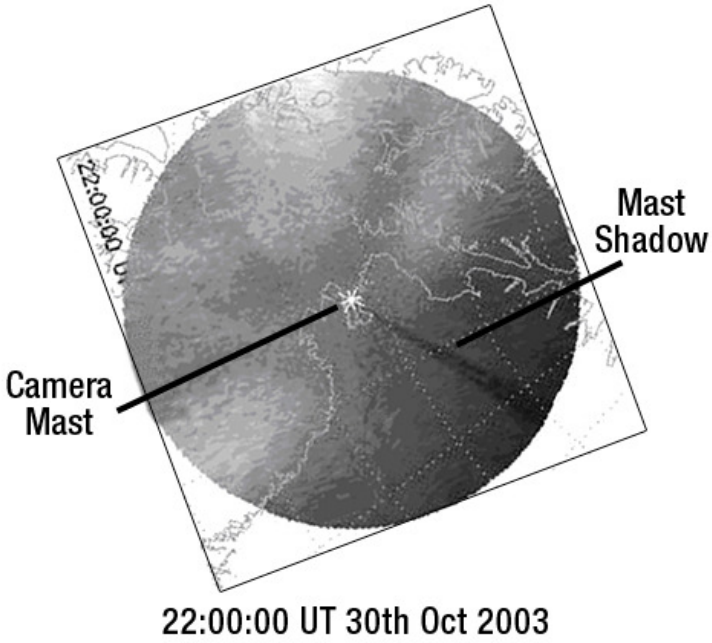

Fig.3.2b: All-sky Camera 630nm light image, 22.00 30th October, 2003

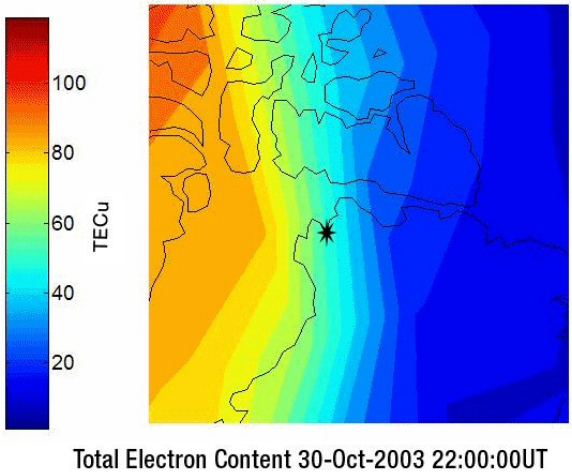

Fig.3.2c: 4º x 4º, latitude x longitude TEC map, 22.00 30th October, 2003

Scintillation observations from the receivers come in the form of S_4 and σ_ϕ values. The σ_ϕ values are available over the mean times of 1, 3, 10, 30 and 60 seconds. (See section 2.1.1 for the definitions of S_4 and σ_ϕ.) The elevation and azimuth of all GPS satellites detected by the receiver is also recorded and given as part of the 1 minute data. This information can be used to calculate the position of the ionospheric pierce point of all received signals, if an arbitrary altitude for the pierce point is selected. (The ionospheric pierce point is the point where a signal ray intersects with the ionosphere. The ionosphere is assumed to be an infinitely thin layer at a specific altitude for these purposes.) These pierce points were mapped to the nearest voxel in the MIDAS 2.0 grids. Since the MIDAS 2.0 grid is updated only every ten minutes but scintillation data, including elevation and azimuth of satellites is updated every minute, it is possible that multiple observations exist mapped to the same grid voxel during the same ten minutes.

Fig.3.3: Locations of GPS Scintillation Receiver Stations used in this Thesis.

The growth rate, γ_{GD}, can take on positive, negative or zero values and in general will vary through time. The amplitude of the actual Gradient Drift Waves, will vary accordingly, however, it can only be positive or zero. Since the waves are the cause of the variations in electron concentration that ultimately cause a radio wave to scintillate, it is the amplitudes of these waves that are of true interest. Computing a correlation co-efficient between the observed scintillation indices and the instantaneous

growth rate at the voxel containing the ionospheric pierce point of the observation, at the time of the observation is straight-forward. This does not give an indication of the wave amplitude at that time and location, though. It would be useful to have knowledge of how the plasma has been affected by the GDI through time as

$$\mathrm{A} \propto e^{\gamma t} \tag{3.3}$$

by definition. (A = amplitude of an unstable wave, t = time, γ = growth rate.) If the value of γ_{GD} is known from t = 0 to t = time of scintillation observation, then it would be possible to calculate a mean amplitude for a Gradient Drift Wave over the same time interval, as follows:

Assume that there is a series of known values of γ_{GD}, each assumed to be constant for ten minutes. The mean amplitude is then given by,

$$\overline{\mathrm{A}} = \left(\int_0^t \mathrm{E}_0 e^{\gamma t} dt - \mathrm{E}_0 t \right) / t \tag{3.4}$$

where,

$\overline{\mathrm{A}}$ = Mean amplitude,

E_0 = Initial (unperturbed) electric field value,

t = Total time elapsed,

$\gamma = \sum_j \gamma_j$, γ_j = the jth GDI growth rate in the series.

This can by evaluated analytically:

$$\int_0^t \mathrm{E}_0 e^{\gamma t} dt = \left[\mathrm{E}_0 e^{\gamma t} / \gamma \right]_0^t = \left(\mathrm{E}_0 / \gamma \right) \left(e^{\gamma t} - 1 \right) \tag{3.5}$$

and, if γt is small, $e^{\gamma t} \simeq 1 + \gamma t + \left(\frac{\gamma^2 t^2}{2!} \right)$, hence $e^{\gamma t} - 1 = \gamma t + \left(\frac{\gamma^2 t^2}{2!} \right)$

$$\therefore \qquad \overline{\mathrm{A}} = \frac{\left(\frac{E_0}{\gamma} \right) \left[\gamma t + \left(\frac{\gamma^2 t^2}{2!} \right) \right] - E_0 t}{t}. \tag{3.6}$$

Eqn.(3.6) simplifies to:

$$\overline{\mathrm{A}} = \frac{\mathrm{E}_0 \gamma t}{2}. \tag{3.7}$$

Obtaining a series of values for γ_{GD} is possible because MIDAS 2.0 provides values for the plasma drift velocity, as computed by the Weimer Model, and updated every ten minutes along with the electron concentration values. Converting the velocities to units of voxels per second and ignoring possible vertical motion, it is possible to trace the motion of a plasma packet back through time, to an accuracy of the nearest voxel. As values of γ_{GD} are calculated for all voxels at all times, the series of values at ten minutes intervals can be found and used in eqn.(3.7). A correlation co-efficient can then be calculated for all observations and their associated mean amplitude values. In the absence of theoretical grounds for expecting any specific type of positive correlation (e.g. 1.5 power, linear, square root) and being constrained by available time to testing only one specific correlation, the linear correlation co-efficient was selected. This represents both the simplest possible relation and, near the origin, other possible correlations approximate to the linear correlation anyway (if extreme powers for the correlation are excluded).

Analyses were conducted on a daily basis, with the first MIDAS 2.0 output at 00.00 UT and the last at 23.50 UT of the same day. This means that for the first output grid, only the instantaneous growth rate is known. For the last, potentially 24 hours of history is known. It is possible that the Weimer drift velocity indicates that a plasma packet has left the voxel grid entirely. In such circumstances, a hole would appear in the grid, so it is assumed that a new plasma packet replaces it, with a new series of γ_{GD} starting from t = 0 at the time of appearance of the new packet. Because a plasma packet could appear at any time it is, in general, not possible to predict the length of time that the mean amplitude must be calculated over and mean amplitudes will have been calculated over various lengths of time between ten minutes and 24 hours. The amplitude of the wave is arbitrarily assumed to be zero at the start of the available time series. This means that initial values of the growth rate equal to or less than zero have no impact and can be ignored, as can every such value that comes before the first positive value.

When multiple scintillation observations have ionospheric pierce points occurring in the same voxel in the same ten minute time interval, mean values of the scintillation indices are calculated and used subsequently for the calculation of the correlation co-efficients.

Since the choice of ionospheric altitude is crucial but arbitrary in this analysis, it was repeated for every altitude step in the voxel grid.

3.3 Results

Table 2 shows which scintillation receiver stations' data were used for each day analysed. All available data for a given day was employed but not all stations were recording on all days. If a station was recording at all for a particular day, then it recorded for the entire day. When calculating correlation co-efficients, there was no discrimination between stations by means of statistical weighting.

Figs.3.4 – 3.13 show the results of these analyses. Only the correlation co-efficients with p-values < 5% are plotted. (It is assumed that the assessed values are normally distributed and the p-values are for a normal distribution.) The vertical error bars are $\pm$ 20km, representing the height range of a voxel. The horizontal error bars represent the 95% confidence limits for the correlation co-efficients. No results are available at altitudes greater than 500km because no ray-paths from GPS satellites to scintillation receivers go through voxels at such altitudes. Plots for S_4 and σ_ϕ(3s) correlations for each storm period are presented, showing the results for each assumed ionospheric pierce-point (IPP) altitude. If no results appear at a given altitude then no correlation co-efficients with p-values < 5% were found during that storm period at that assumed IPP altitude. There are no σ_ϕ(3s) correlation co-efficients with p-value < 5% for October 30th 2003 or May 14-16th 2005 so σ_ϕ(10s) results are shown instead. The results for σ_ϕ over mean time intervals longer than those shown in the graphs are similar to those in the figures.

When interpreting the graphs shown in figs.3.4-3.12, the most important factor is whether or not, at any given altitude, there are positive or negative values and how many of each. Positive correlations without negative correlations at a given altitude, make a case for the GDI process occurring and vice versa. When positive and negative correlations appear at a given altitude the interpretation is more ambiguous, depending on how many of each there are, their exact values and confidence ranges as shown by the error bars.

Scintillation Receiver Data Used							
Storm 1: October 2003							
	Station						
	Athabasca	Calgary	Kiruna	Sodankyla	Svarlbard	Tromso	Yellowknife
30th	√				√		√
Storm 2: July 2004							
	Station						
	Athabasca	Calgary	Kiruna	Sodankyla	Svarlbard	Tromso	Yellowknife
24th			√	√	√	√	
25th			√	√	√	√	√
26th			√	√	√	√	√
27th			√	√	√	√	√
28th			√	√	√	√	√
Storm 3: November 2004							
	Station						
	Athabasca	Calgary	Kiruna	Sodankyla	Svarlbard	Tromso	Yellowknife
8th			√	√	√	√	
9th			√	√	√	√	
10th			√	√	√	√	
11th			√	√	√	√	
Storm 4: May 2005							
	Station						
	Athabasca	Calgary	Kiruna	Sodankyla	Svarlbard	Tromso	Yellowknife
14th		√	√	√	√	√	√
15th		√	√	√	√	√	√
16th		√	√	√	√	√	√

Table 3.3: Scintillation receiver stations used for each day analysed. When data is available for a day it covers all 24hrs of that day.

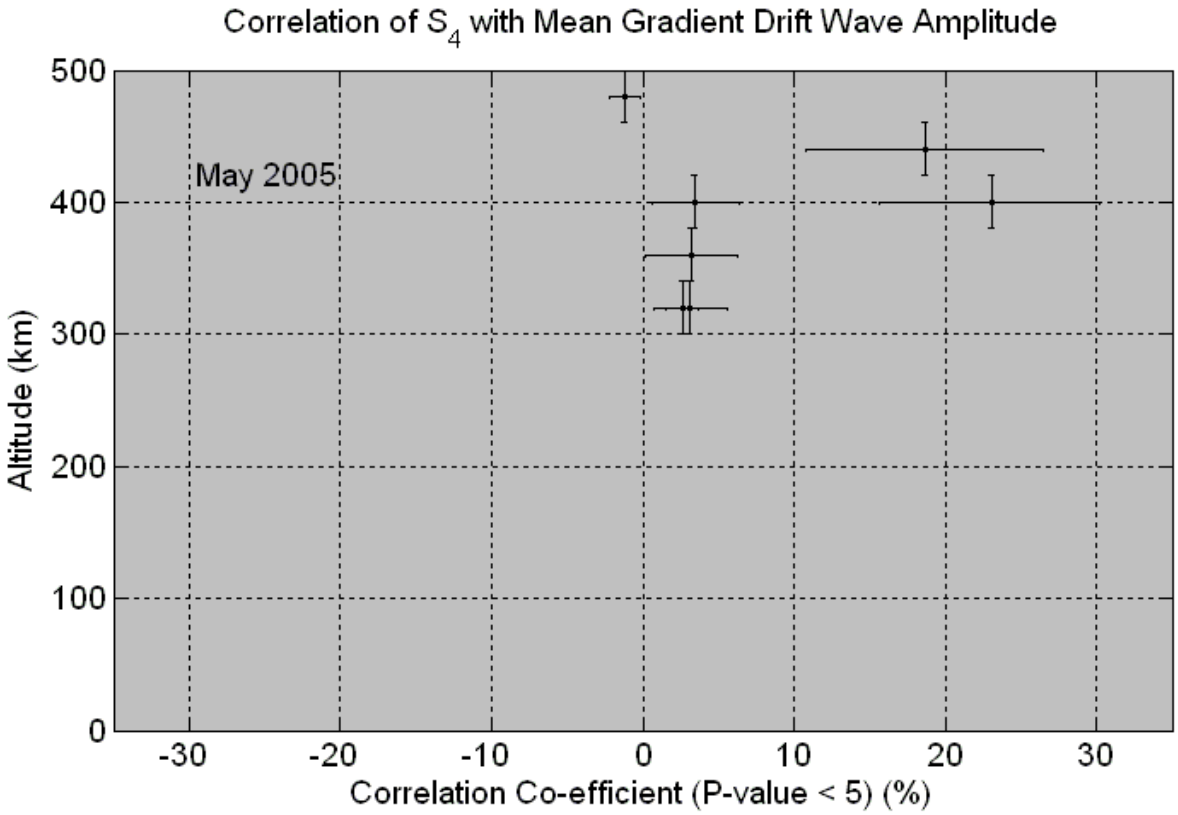

Fig.3.4: Correlation of S_4 with Modelled Mean Gradient Drift Wave Amplitude (May 2005 storm).

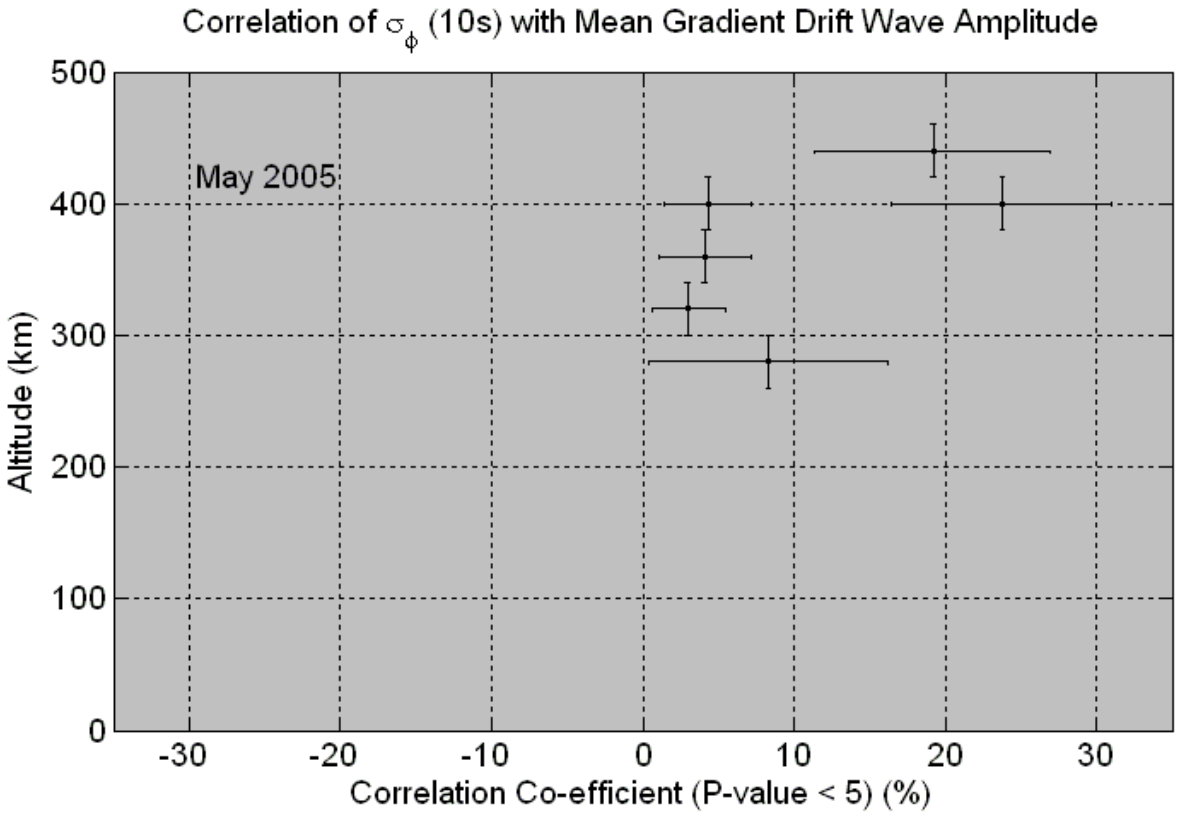

Fig.3.5: Correlation of σ_ϕ(10s) with Modelled Mean Gradient Drift Wave Amplitude (May 2005 storm).

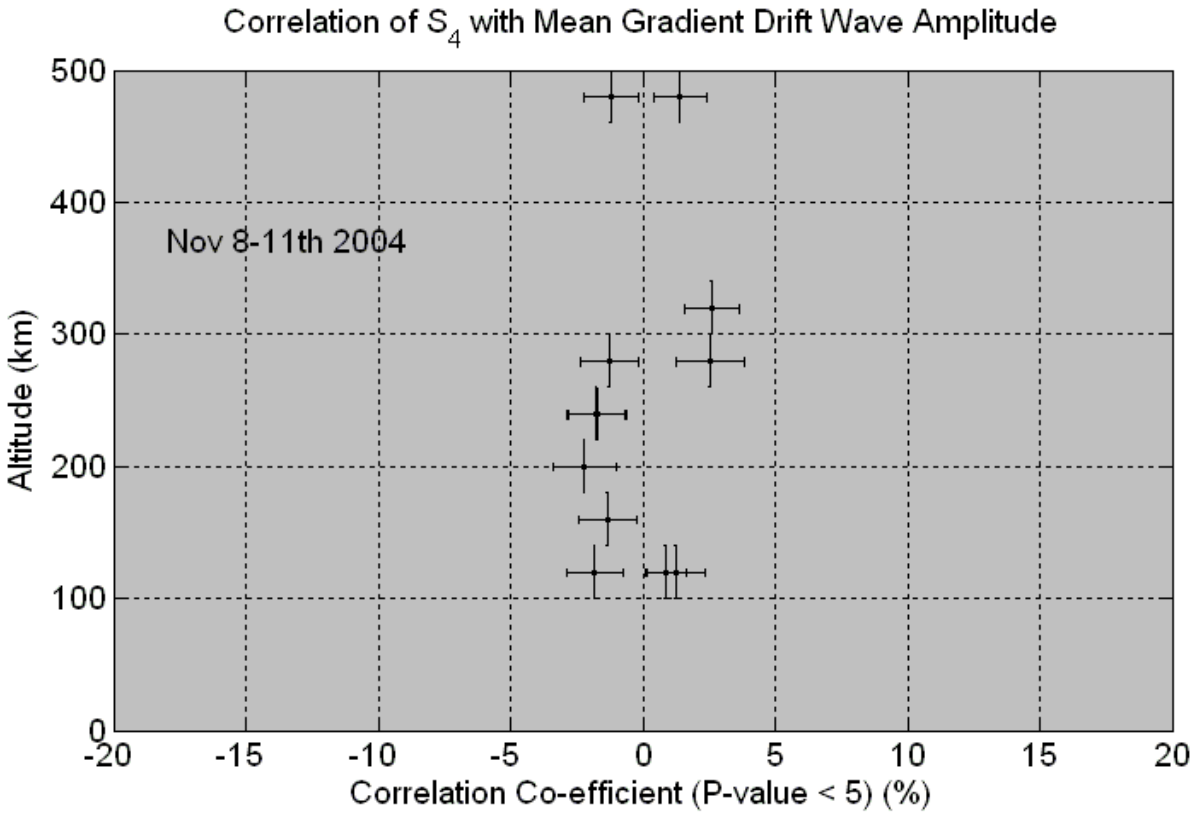

Fig.3.6: Correlation of S_4 with Modelled Mean Gradient Drift Wave Amplitude (November 2004 storm).

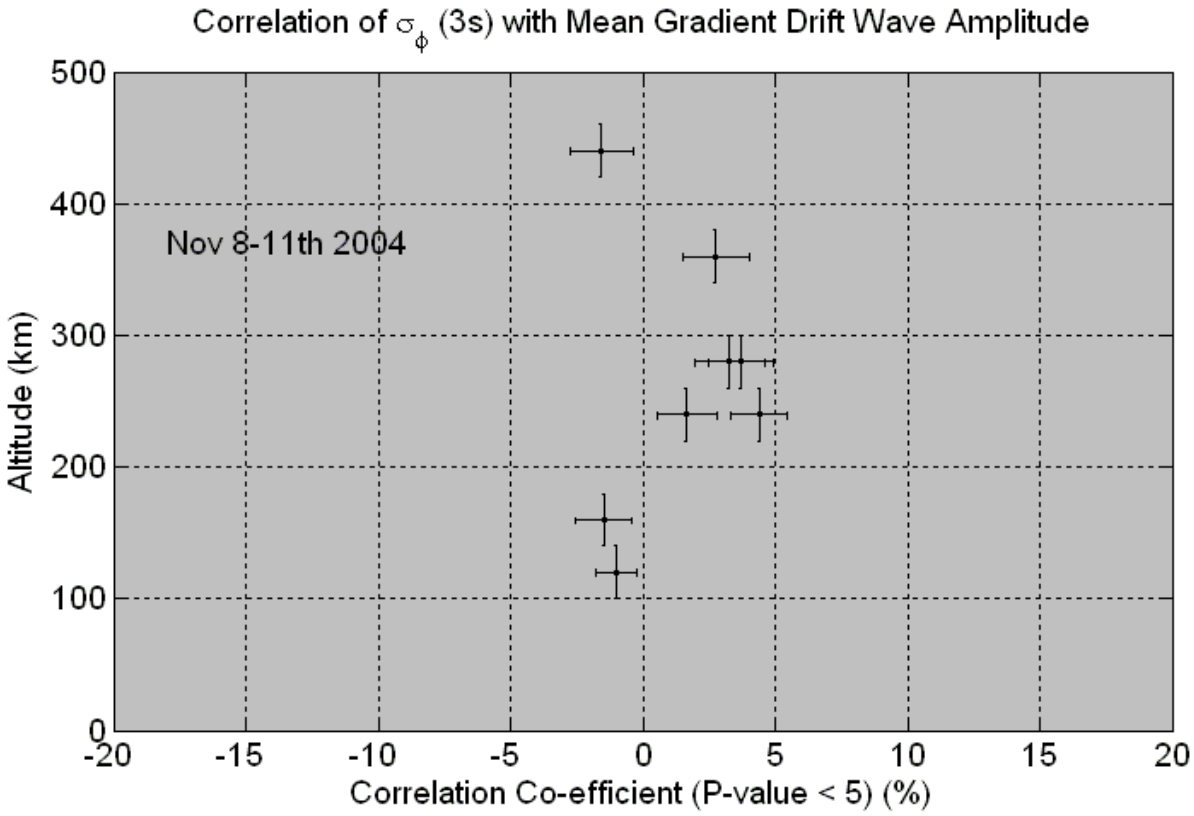

Fig.3.7: Correlation of σ_ϕ (3s) with Modelled Mean Gradient Drift Wave Amplitude (November 2004 storm).

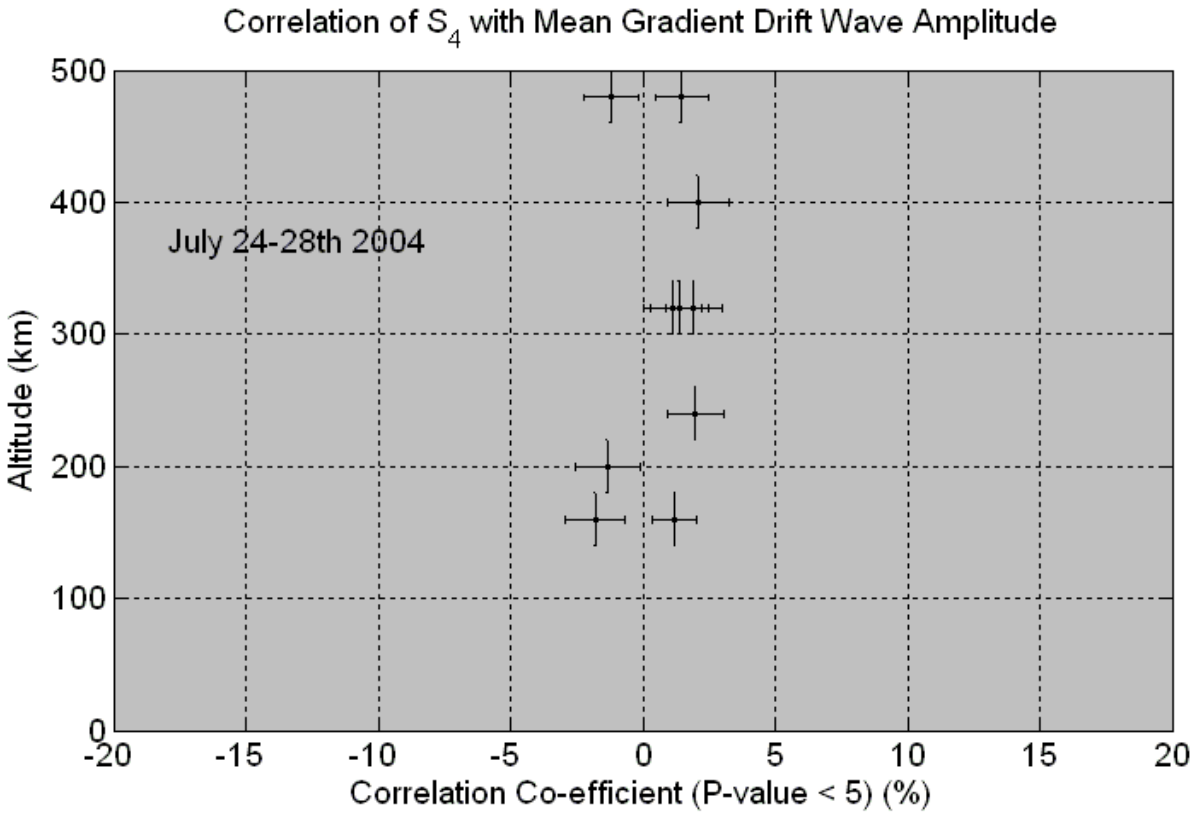

Fig. 3.8: Correlation of S_4 with Modelled Mean Gradient Drift Wave Amplitude (July 2004 storm).

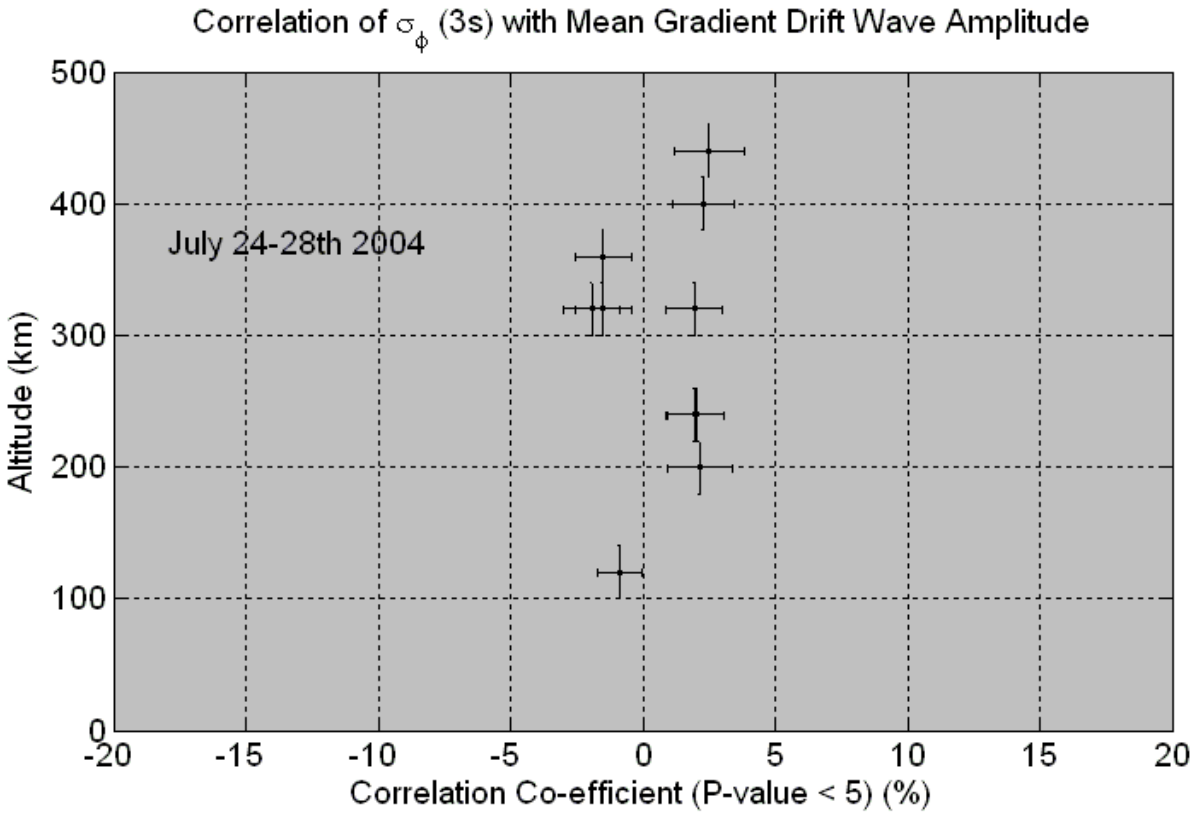

Fig.3.9: Correlation of σ_ϕ (3s) with Modelled Mean Gradient Drift Wave Amplitude (November 2004 storm).

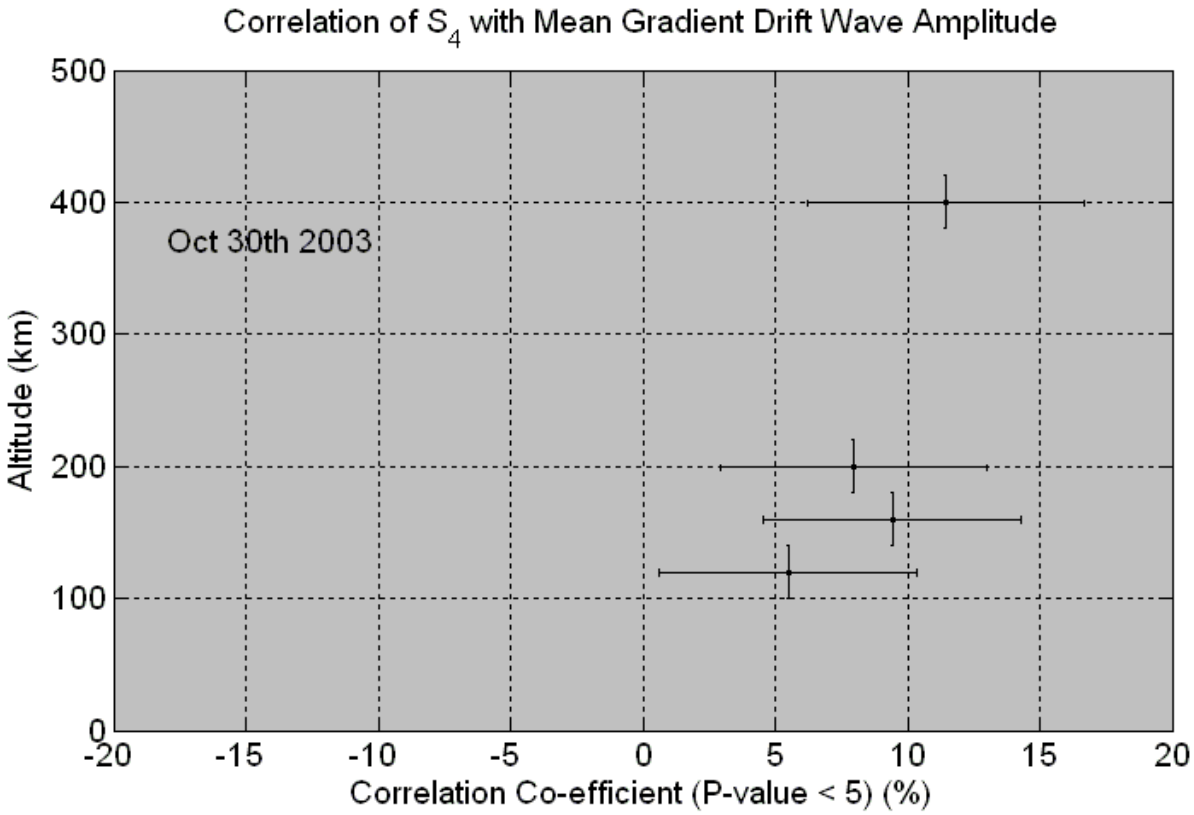

Fig. 3.10: Correlation of S_4 with Modelled Mean Gradient Drift Wave Amplitude (October 30th 2003 storm).

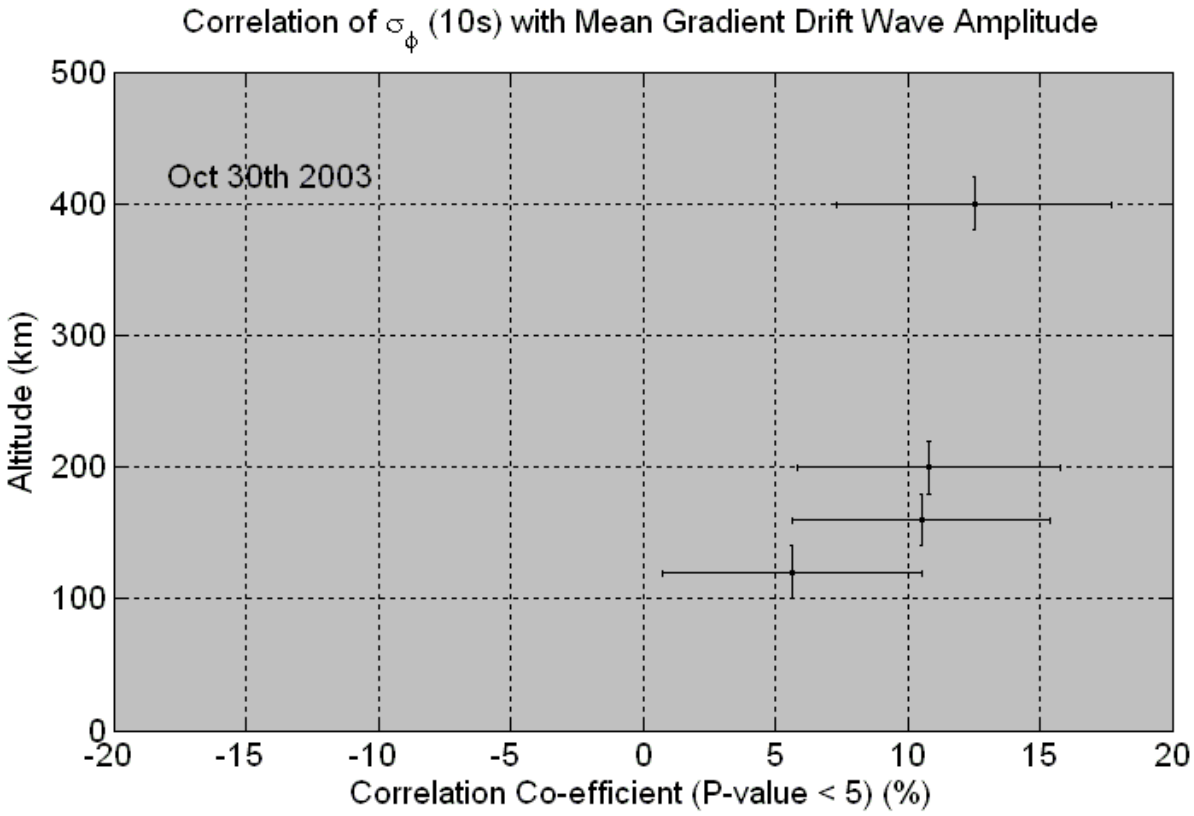

Fig.3.11: Correlation of σ_ϕ (10s) with Modelled Mean Gradient Drift Wave Amplitude (October 30th 2003 storm).

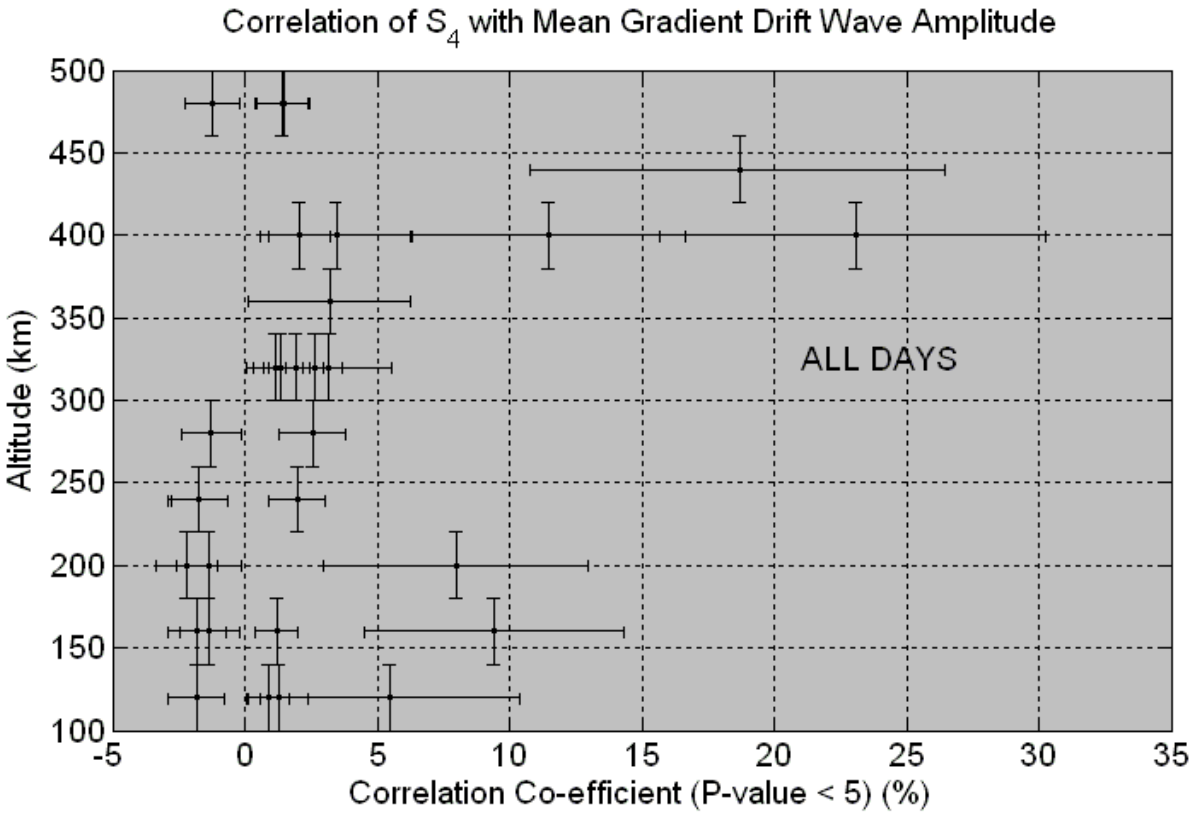

Fig.3.12a: Correlation of S_4 with Modelled Mean Gradient Drift Wave Amplitude (All Days).

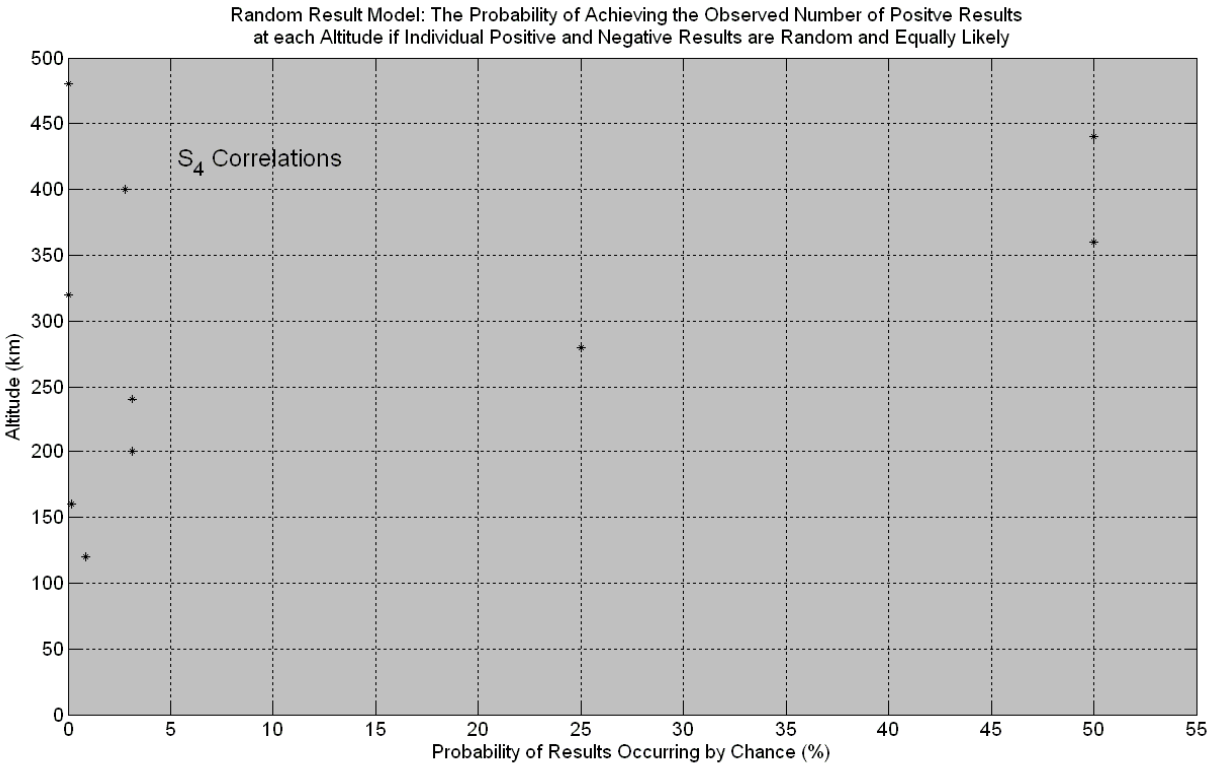

Fig.3.12b: Random Result Model: The probability of achieving the observed number of positive results at each altitude in fig3.12a if individual positive and negative results are random and equally likely.

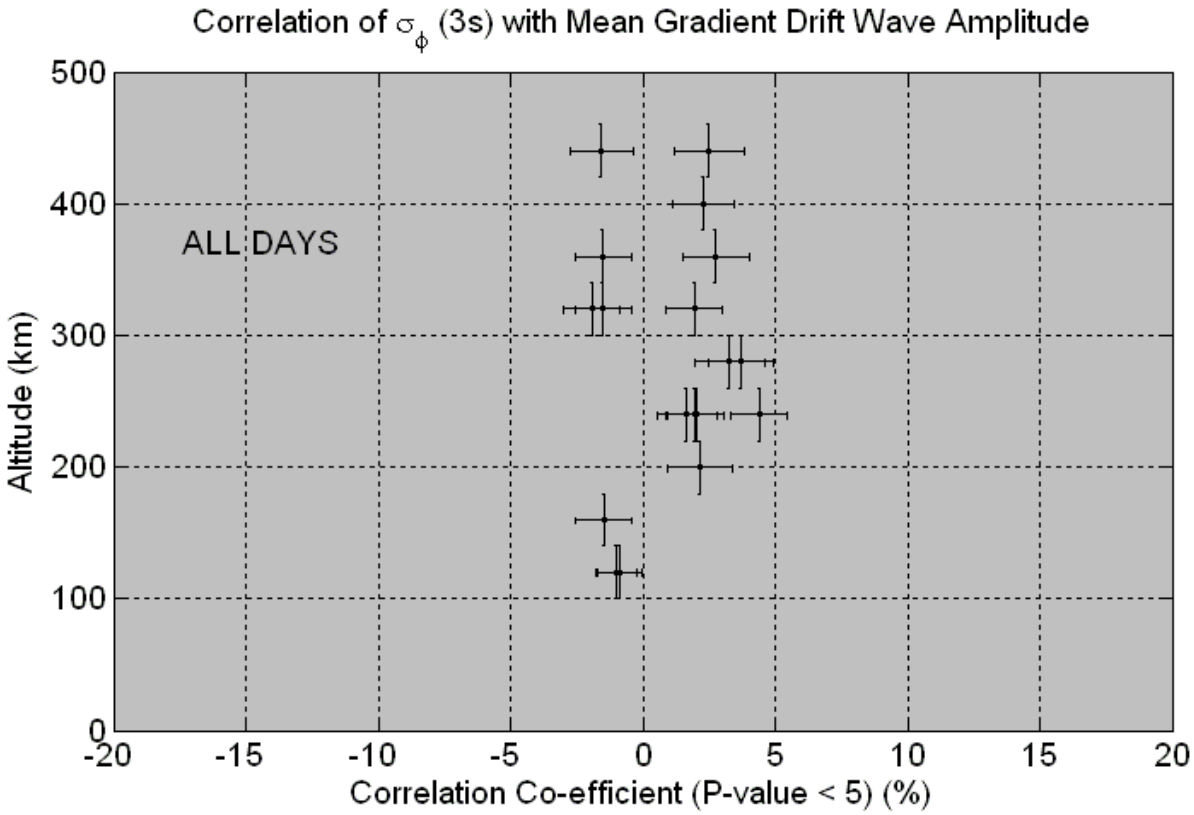

Fig.3.13a: Correlation of σ_ϕ(3s) with Modelled Mean Gradient Drift Wave Amplitude (All Days).

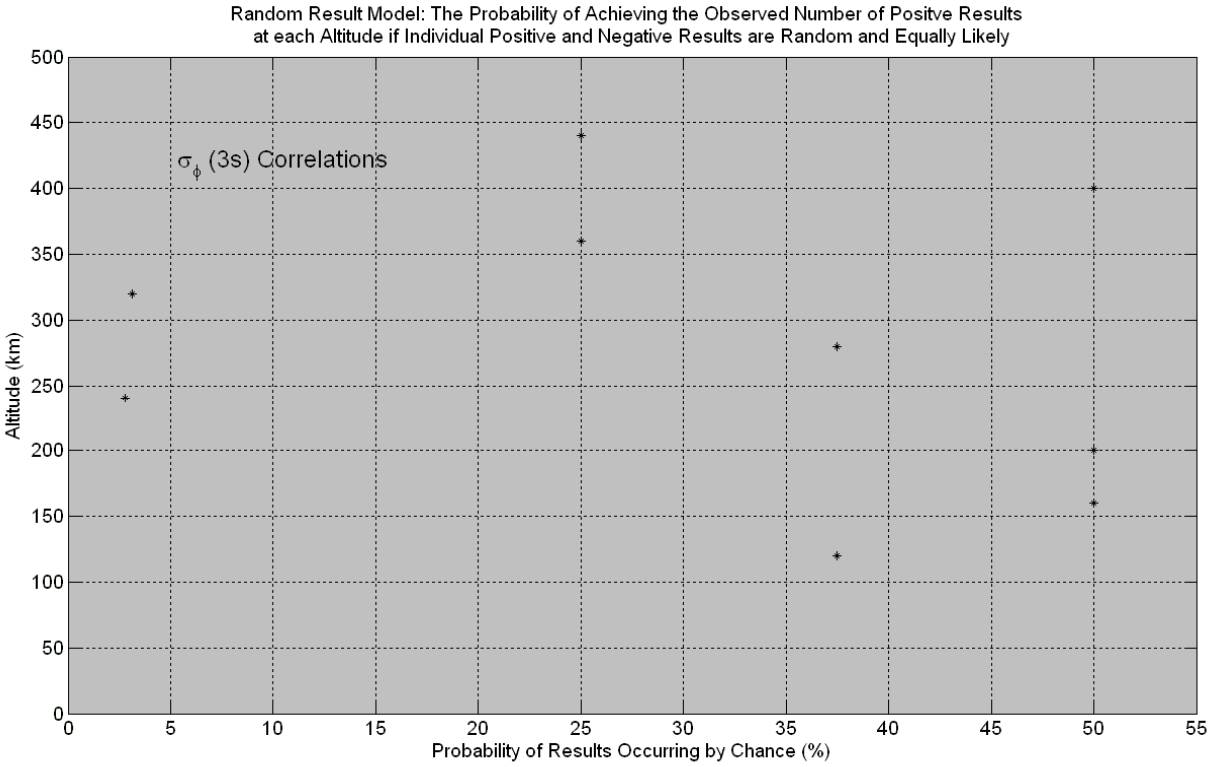

Fig.3.13b: Random Result Model: The probability of achieving the observed number of positive results at each altitude in fig.3.1a if individual positive and negative results are random and equally likely.

Figs. 3.12a and 3.13a show the same results collating all analysed days on to one graph each for S_4 and σ_ϕ(3s) correlations. Figs.3.12b and 3.13b show the results of a simple statistical model that calculates the probability of achieving the observed number of positive results at each altitude in figs.3.12a and 3.13a if individual positive and negative results are random and equally likely. Mathematically,

$$P = \frac{n!}{x!(n-x)!} p^x (1-p)^{n-x}, \qquad (3.8)$$

where,
P = probability of the observed number of positive results
n = the total number of results
x = the number of positive results
p = the probability of an individual result being positive (assumed = 0.5). On the graphs the values of P have been multiplied by 100 to give a percentage probability.
The complete results for all days analysed are tabulated in Appendix 3.

3.4 Conclusions

Correlation co-efficients with low values but with associated p-values < 5% imply statistically weak but significant correlations, in this case between the calculated mean GDW amplitudes and the scintillation indices S_4 and σ_ϕ.

Fig.3.12a, S_4 correlations for all days analysed, shows an altitude range (300 – 460km) where there are positive correlation data points but no negative ones. The results at 320km and 400km are unlikely to occur randomly, according to fig.3.12b; at 360km and 440km too few results exist to allow the probability of any outcome to be small (< 10%). At all other altitudes the results are more equivocal, with at least one result on each side of the zero line.

Fig.3.13a, σ_ϕ(3s) correlations for all days analysed, shows an altitude range of 200 – 300km where there are positive correlation data points but no negative ones. The 240km results are unlikely to occur by chance, according to fig.3.13b. The rest of the results in the 200 – 300km have too few data points for any of the outcomes to have a low probability of occurring by chance.

Hence there is an apparent conflict between the altitude range showing the best correlations using the S_4 index and the altitude range showing the best correlations using the σ_ϕ(3s) index, when considering together all the days analysed. This conflict is less apparent when considering each storm period individually (figs.3.4 – 3.11).

Thin phase screen theory predicts more severe amplitude scintillation at lower altitudes but no change in the severity of phase scintillation (for a given PSD graph slope). Hence at lower altitudes similar correlation results would be expected from σ_ϕ and S_4; this is not seen in figs.3.12a and 3.13a. It also predicts that σ_ϕ would have no dependence on altitude and hence the correlation co-efficients would be similar at all altitudes, which is not observed in fig.3.13a. (Altitudes above 300km show weaker evidence for positive correlation than do those in the range 200 – 300km.)

The model presented here should not be expected to conform to the predictions of thin phase screen theory, however. In a thin phase screen model it is assumed that scintillation is imposed on the signal passing through it. The model presented here does not; it takes observed values of scintillation indices (which will vary from indicating definite ionospheric effects to being so small as to represent noise rather than ionospheric scintillation) and asks is there linear correlation between the observations and theoretically calculated plasma instability events? In other words, there is no assumption of ionospheric scintillation occurring on every ray-path.

Where both positive and negative correlation co-efficients occur (low and very high altitudes) it is likely that low electron concentration values prevail. In such circumstances the model can give high values for γ_{GD} because the $1/n_0$ term dominates in eqn.(3.1) but the possibility of generating irregularities is in fact negligible, precisely because the electron concentration is too small.

The fact that there is a range of altitudes (as opposed a single altitude) giving only positive correlations is unsurprising given that the analysis is spread over a number of days and the whole of the MIDAS 2.0 grid where signal ray paths are observed, covering a wide geographical area: prevailing conditions will vary and the height range 200-460km is plausible for scintillation activity.

In summary, the novel modelling technique developed and presented here predicts a weak but significant correlation between the S_4 and σ_ϕ indices calculated from GPS L1 band receivers and the Gradient Drift Instability mechanism of generating plasma irregularities in the polar ionosphere, during magnetic storm conditions.

Chapter 4: Modelling the Turbulence Growth Rate

4.1 Introduction

This analysis looks at the possibility of turbulent plasma flow generating irregularities that subsequently cause scintillation on L1 band GPS signals. It deliberately pursues a method as similar as possible to that of the previous analysis (the GDI mechanism) so that the results are directly comparable.

A model is developed analogous to that for the GDI growth rate: A calculation of the turbulence growth rate, γ_T, (an equivalent to γ_{GD}) is calculated for each time and voxel of the MIDAS 2.0 grid. Again mean amplitudes are determined from the values of γ_T. The extent of the linear correlation between these mean amplitudes and the scintillation indices, S_4 and σ_ϕ is then evaluated. The results are then compared with those from the GDI model.

An equation for γ_T is needed. This is defined below, following [*Kelley*, 1989]. First $\varphi_T(k)$, the growth rate for any given wavenumber, k, is defined:

$$\varphi_T(k) = \frac{E(k)\nabla n_e}{B n_e}. \tag{4.1}$$

Because the expression for γ_{GD} in eqn.(3.1) is independent of wavenumber, eqn.(4.1 is not directly comparable. The required equation will use the root mean square of all values of $\varphi_T(k)$ over the relevant range, $k_L \to \infty$. Mathematically,

$$\gamma_T = \frac{\left[\int_{k_L}^{\infty} E(k)^2 dk\right]^{1/2} . \nabla n_e}{B n_e} \tag{4.2}$$

k_L, the shortest relevant wavenumber is defined as $k_L = 2\pi \frac{\nabla n_e}{n_e}$.

The magnetic field strength B is obtained from the IGRF model. The IGRF model is a model of the Earth's magnetic field requiring only spatial co-ordinates and a date as inputs and giving the magnetic field strength as output. The model extends beyond ionospheric altitudes so results for all grid voxels and times can be obtained [*Macmillan and Maus*, 2005; *Maus et al.*, 2005a; b; *Maus et al.*, 2005c]. $\frac{\nabla n_e}{n_e}$ is calculated directly from the MIDAS 2.0 results. E(k) is needed to perform the integral, however, and this is difficult to obtain: There are few published electric field spectra so the ideal case of specifying E(k) at all times and locations from directly observed data is

impossible. Some assumption about the nature of E(k) must be made in order to progress.

[*Mounir et al.*, 1991] used ARCAD-AUREOL-3 observations to obtain values of the electric field. (The ARCAD-AUREOL-3 satellite had a polar orbit and instruments for measuring the in-situ electric field as two perpendicular components, one being in the local horizontal plane.) The measurements of this component of the electric field from several orbits were used to obtain power spectral density graphs. Linear least squares fits to the data (plotted as log-log graphs) were obtained and the slopes of the resulting straight lines calculated. Slopes obtained in such a manner are referred to as the "spectral indices" of the graphs. A bar-chart of the occurrence of the spectral indices is also presented by [*Mounir et al.*, 1991]. The most frequently occurring spectral indices were in the range 1.6 to 1.8. These data allow a calculation to be made that gives values for the integral,

$$\int_{k_L}^{\infty} E(k)^2 dk . \tag{4.1}$$

The data presented in this paper are all that could be obtained that allow eqn.(4.1) to be solved. They are not ideal as the fading frequency range for a GPS L1 band signal cannot be expected to be identical to that shown in [*Mounir et al.*, 1991] for the ARCAD-AUREOL-3 satellite. This introduces a source of error into the value of the spectral index that is not readily quantifiable.

From fig.4.1 it can be seen that

$$\log(E(k)^2) = -\rho \log(k) + \log(\beta) \tag{4.2}$$

or

$$E(k)^2 = \beta k^{-\rho} \tag{4.3}$$

where ρ = the modulus of the spectral index (the minus sign is present because the slope is always negative) and β = a constant obtained from the graph by evaluating $\beta = C.10^{-\rho}$.

Substituting eqn.(4.3) into eqn.(4.1) gives

$$\int_{k_L}^{\infty} E(k)^2 dk = \int_{k_L}^{\infty} \beta k^{-\rho} dk \Rightarrow \beta \left[\frac{k^{1-\rho}}{1-\rho} \right]_{K_L}^{\infty} \tag{4.4}$$

$$\Rightarrow 0 - \beta k_L^{1-\rho} / (1-\rho) = \beta k_L^{1-\rho} / (\rho - 1) . \tag{4.5}$$

To progress from here, the expression for k_L and values for the constants ρ and β must be substituted into eqn.(4.5). The value 1.6 was selected for ρ as it is in the range of most frequently occurring values according to the bar chart presented by [*Mounir et al.*, 1991] and the range 1.4 to 1.6 occurs much more frequently than the range 1.8 to 2.0. Only one graph of the power spectral density is presented by [*Mounir et al.*, 1991] so there is little choice but to calculate β directly from it: $\beta = 4.27 \times 10^{-5}$ (see fig.4.1). Making these substitutions gives

$$\int_{k_L}^{\infty} E(k)^2 dk = \frac{4.27 \times 10^{-5} . \left[2\pi . (\nabla n_e / n_e) \right]^{-0.6}}{0.6} . \tag{4.6}$$

Substituting this into eqn.(4.2) for γ_T yields

$$\gamma_T = \left(\frac{4.27\text{x}10^{-5}.\left[2\pi.\left(\nabla n_e/n_e\right)\right]^{-0.6}}{0.6} \right)^{1/2} .\left(\frac{\nabla n_e}{n_e B} \right), \qquad (4.7)$$

and simplifying slightly:

$$\gamma_T = \left(\frac{4.27\text{x}10^{-5}}{0.6} \right)^{1/2} .\left[2\pi.\left(\nabla n_e/n_e\right)\right]^{-0.3} .\left(\frac{\nabla n_e}{n_e B} \right). \qquad (4.8)$$

Eqn.(4.8) is the turbulence growth rate required for the model used in this analysis.

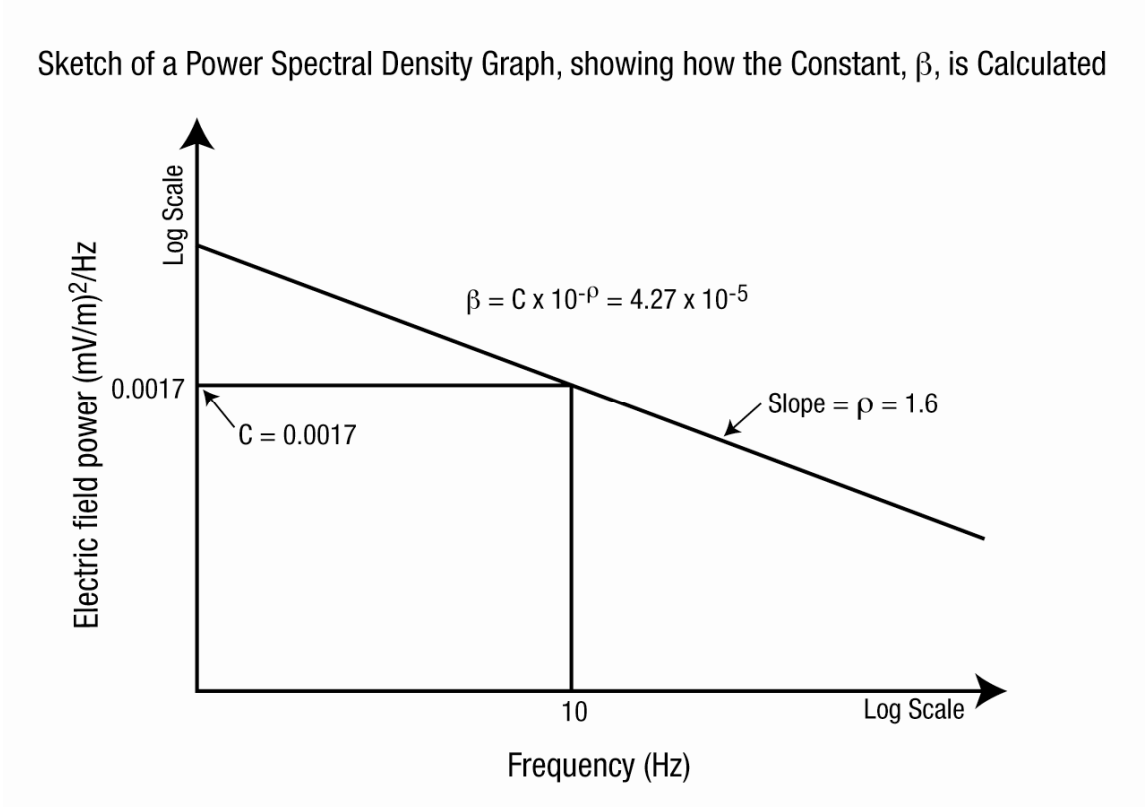

Fig.4.1: Sketch of a straight line fit to an Aureol 3 satellite data power density spectrum. After [*Mounir et al.*, 1991].

This type of model of the effects of turbulence has not been presented in the literature previously.

4.2 Method

Because the model of turbulence presented here and the GDI model presented previously need to be as similar as possible in order for a meaningful comparison to be made, no changes were made to the parameters used by the MIDAS 2.0 algorithm. That is, the voxel grid definition, time interval length and all other user-variable parameters were left exactly as for the GDI analysis. Similarly, direct comparison requires that the same time periods be analysed (see table 3.1). The same GPS receiver stations' observations were employed (see table 3.3).

The same method is employed for calculating the mean amplitude of waves generated by turbulence as was used for the GDI case (see section 3.2) except that γ_{GD} is replaced by γ_T throughout.

4.3 Results

The results of this analysis are presented in the same fashion as for the GDI work: Figs.4.2- 4.9 show the correlation co-efficients with p-values < 5%, for each individual storm period. (It is assumed that the assessed values are normally distributed and the p-values are for a normal distribution, as for the GDI results.) Again the vertical error bars are $\pm$ 20km, representing the height range of a voxel and the horizontal error bars represent the 95% confidence limits for the correlation co-efficients. Plots for S_4 correlations for each storm are shown. Plots for σ_ϕ(3s) correlations are shown, except where there were no correlations with p-value < 5%: In these circumstances a plot of σ_ϕ(10s) correlations with p-value < 5% is presented instead. Results for each assumed altitude of Ionospheric Pierce Point are shown on each graph – if no results appear at a specific altitude then no correlations with p-value < 5% were found at that assumed altitude of IPP. Results for σ_ϕ averaged over longer times are similar to the graphs shown.

When interpreting the graphs in figs.4.2 - 4.12, the most important factor is whether or not, at any given altitude, there are positive or negative values and how many of each. Positive correlations without negative correlations at a given altitude, make a case for the turbulence process occurring and vice versa. When positive and negative correlations appear at a given altitude the interpretation is more ambiguous, depending on how many of each there are, their exact values and confidence ranges as shown by the error bars.

Figs.4.10a and 4.11a show the same results collating all analysed days on to one graph each for S_4, σ_ϕ(3s) and σ_ϕ(10s) correlations. Figs.4.10b, and 4.11b show the results of the same statistical model as used in the GDI analysis: The probability of achieving the observed number of positive results at each altitude in figs.4.10a and 4.11a if individual positive and negative results are random and equally likely:

$$P = \frac{n!}{x!(n-x)!} p^x (1-p)^{n-x}, \qquad (4.9)$$

where,
P = probability of the observed number of positive results
n = the total number of results
x = the number of positive results
p = the probability of an individual result being positive (assumed = 0.5). On the graphs the values of P have been multiplied by 100 to give a percentage probability.
The complete results for all days analysed are tabulated in Appendix 4.

4.4 Conclusions

Figs.4.10a and 4.11a, the results for all days analysed, show an overall picture of little correlation between the modelled mean turbulent wave amplitude and the scintillation indices S_4 and σ_ϕ. The equivalent graphs for the GDI case, figs.3.12a and 3.13a, show stronger correlation, particularly when the chosen ionospheric pierce points are at plausible ionospheric altitudes (200-440km).

Looking in more detail at individual storm periods the situation revealed is not so straightforward. Comparison of the turbulence case with the GDI case shows two storms, July and November 2004, where results suggest approximately equal evidence of correlation between the mean wave amplitudes and the S_4 observations. In the July 2004 case the σ_ϕ(3s) results also look approximately equally positive for correlations with each mechanism. The other two storms analysed (October 30th 2003 and May 2005) show the GDI mechanism as correlating better than the turbulence mechanism.

In summary, the turbulence process of plasma irregularity generation sometimes correlates with observed scintillation indices approximately as well as the GDI process.

These results do not, however, indicate one way or the other, which process is dominating the formation of irregularities over a given time or volume of ionosphere, except where the GDI process has significant positive correlation and the turbulence process has not, or vice versa. The linear correlation co-efficient takes no account of the difference in absolute size of the results contained in the two data sets, modelled mean wave amplitude due to the GDI process and modelled mean wave amplitude due to the turbulence process. It is possible that whilst equally well correlated with the scintillation observations, the mean amplitudes from the GDI model are always larger than the equivalent mean amplitudes for the turbulence process, or vice versa. In such circumstances the process with consistently larger mean wave amplitudes would dominate the process of irregularity formation in plasma patches. This topic is raised in more detail in section 6.2, Future Work.

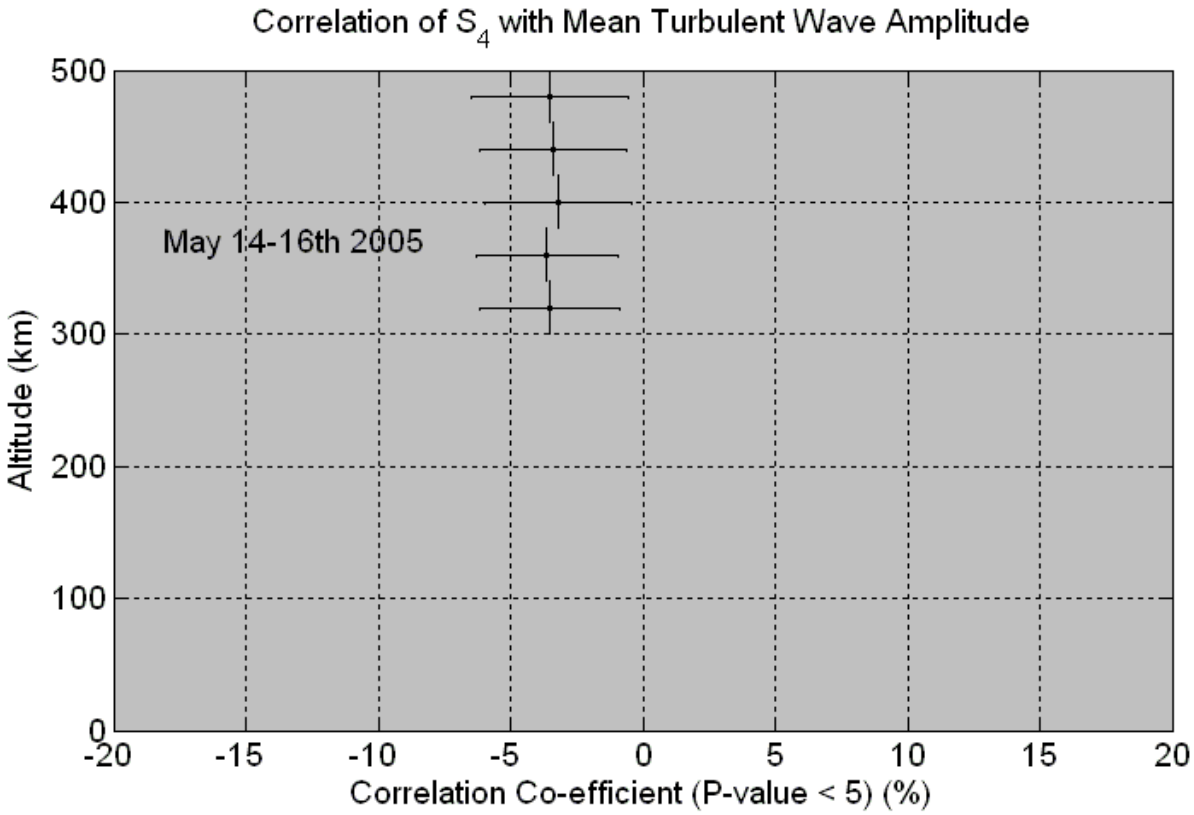

Fig.4.2: Correlation of S_4 with Modelled Mean Turbulent Wave Amplitude (May 2005 storm).

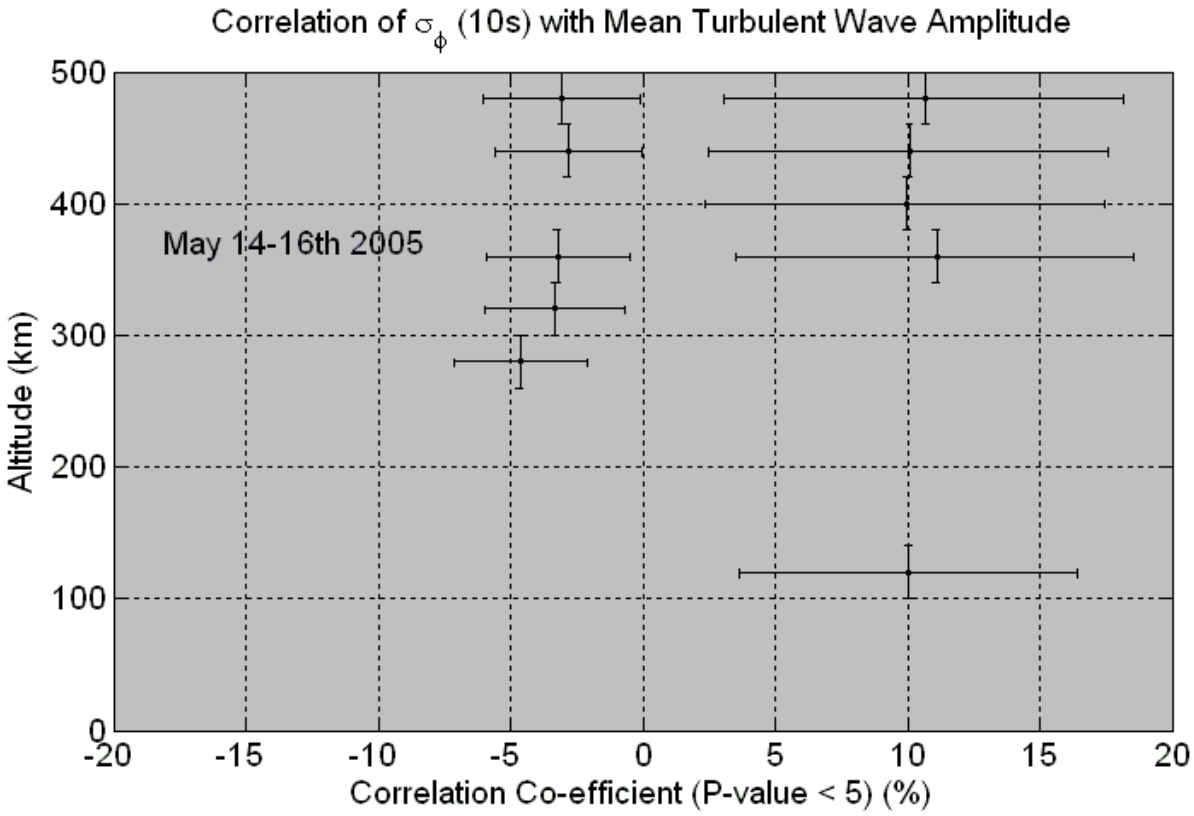

Fig.4.3: Correlation of σ_ϕ (10s) with Modelled Mean Turbulent Wave Amplitude (May 2005 storm).

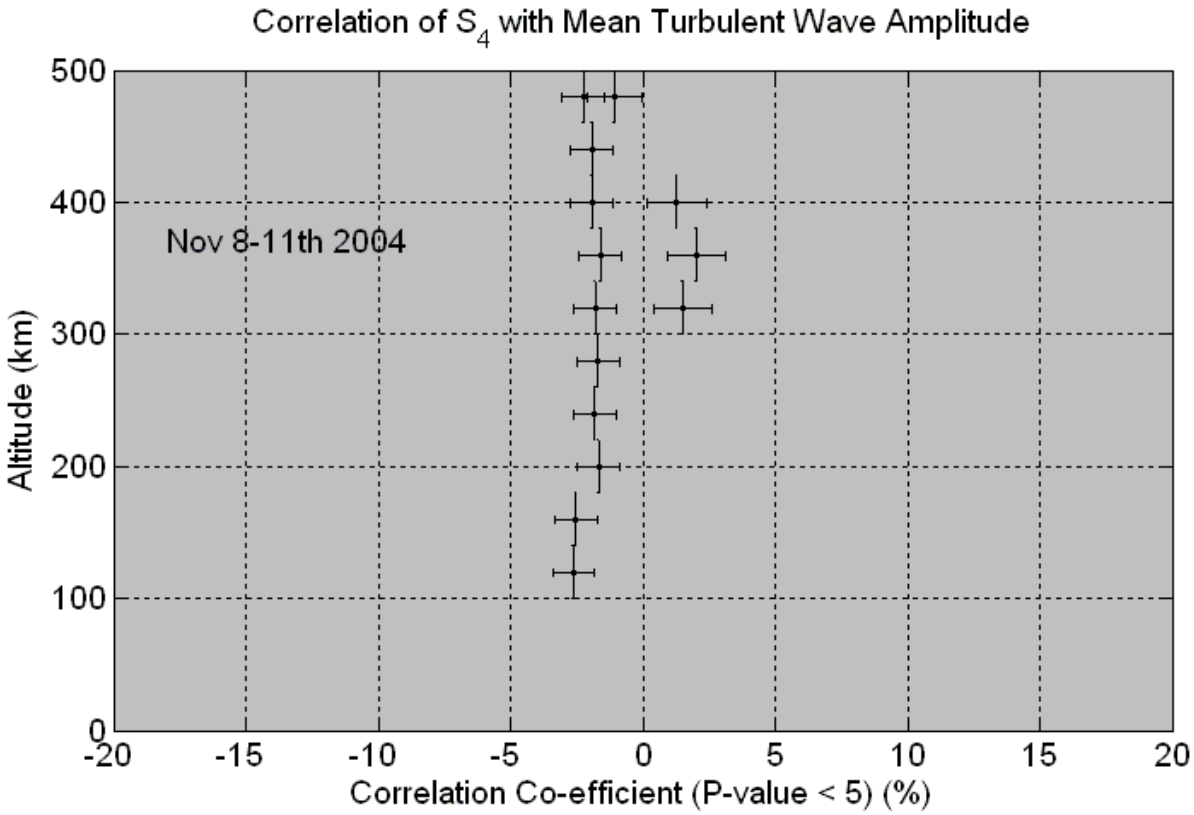

Fig.4.4: Correlation of S_4 with Modelled Mean Turbulent Wave Amplitude (November 2004 storm).

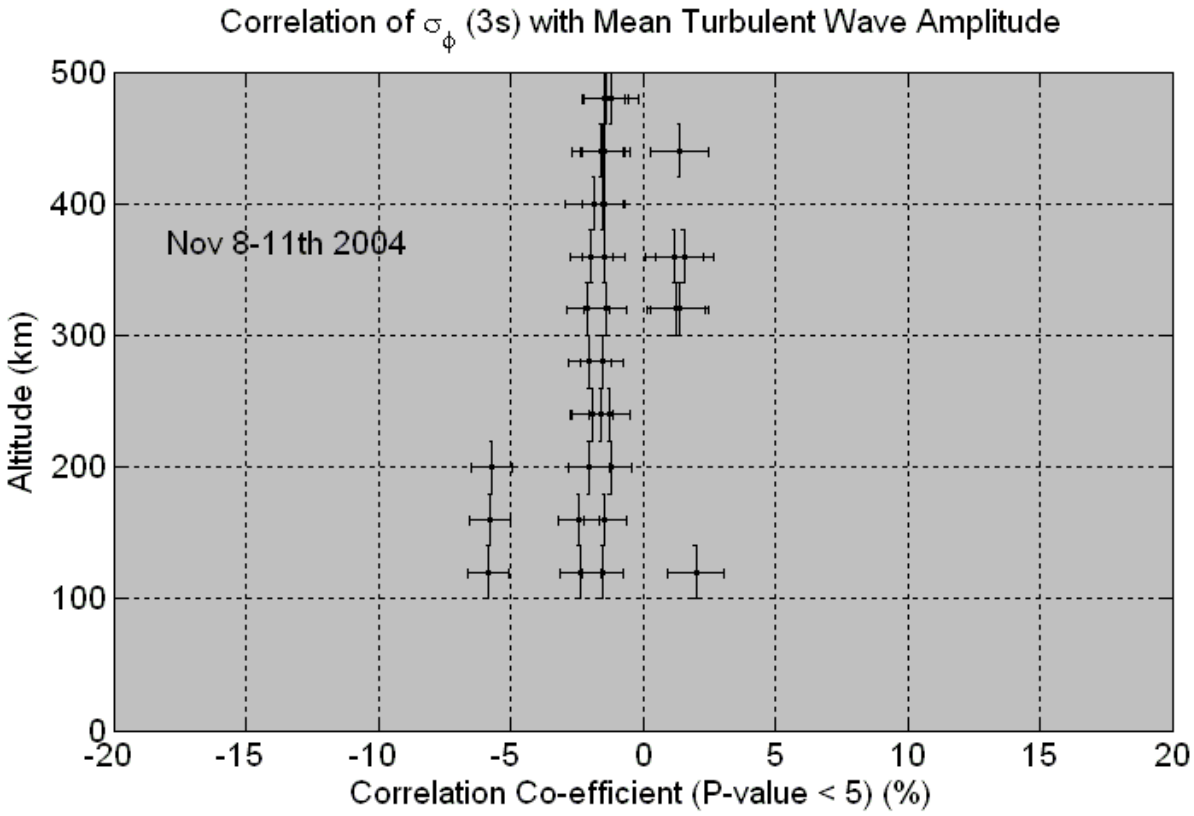

Fig.4.5: Correlation of σ_ϕ (3s) with Modelled Mean Turbulent Wave Amplitude (November 2004 storm).

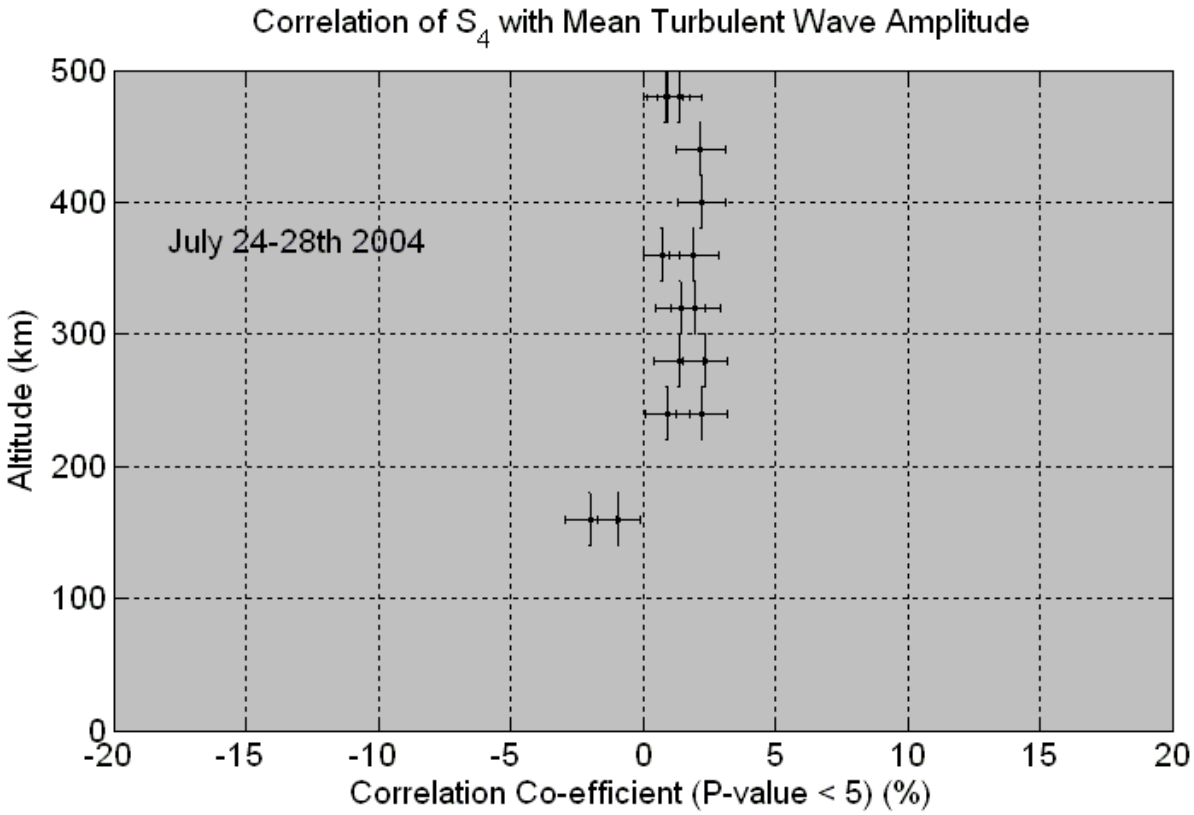

Fig.4.6: Correlation of S_4 with Modelled Mean Turbulent Wave Amplitude (July 2004 storm).

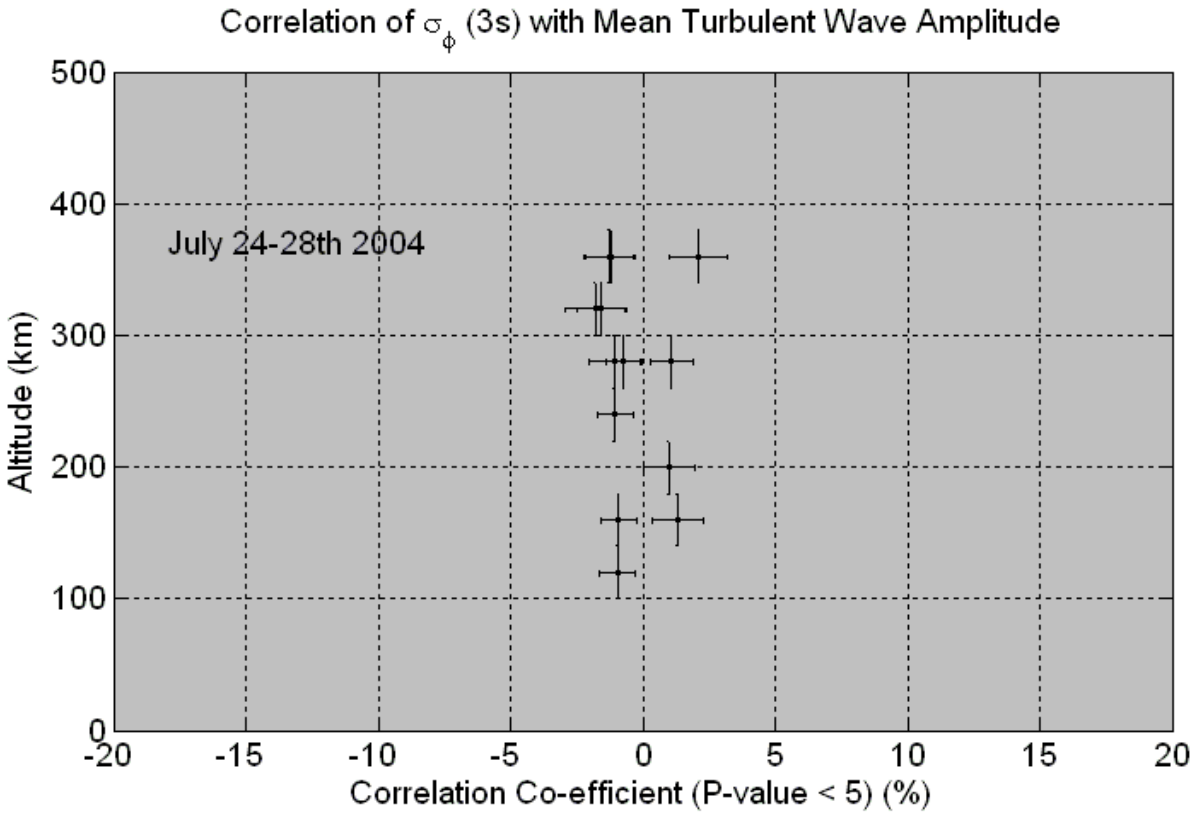

Fig.4.7: Correlation of σ_ϕ(3s) with Modelled Mean Turbulent Wave Amplitude (July 2004 storm).

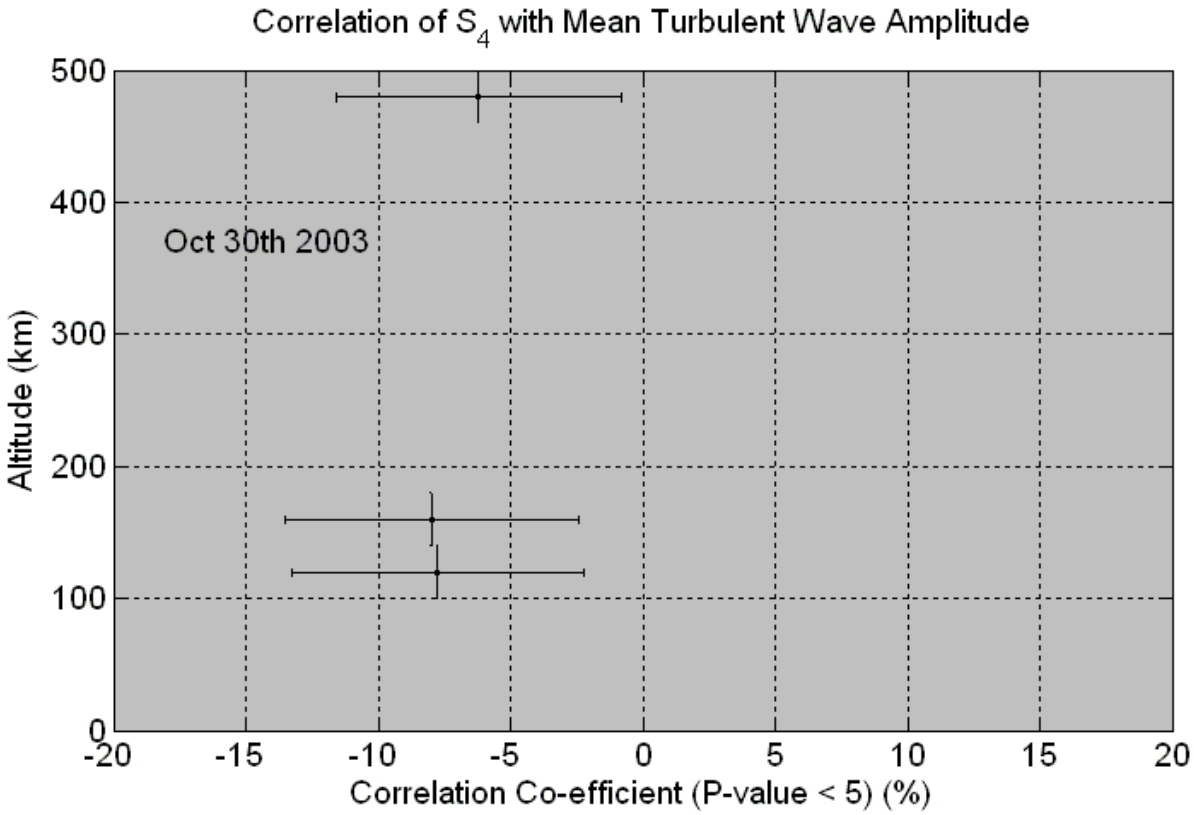

Fig.4.8: Correlation of S_4 with Modelled Mean Turbulent Wave Amplitude (October 30th 2003 storm).

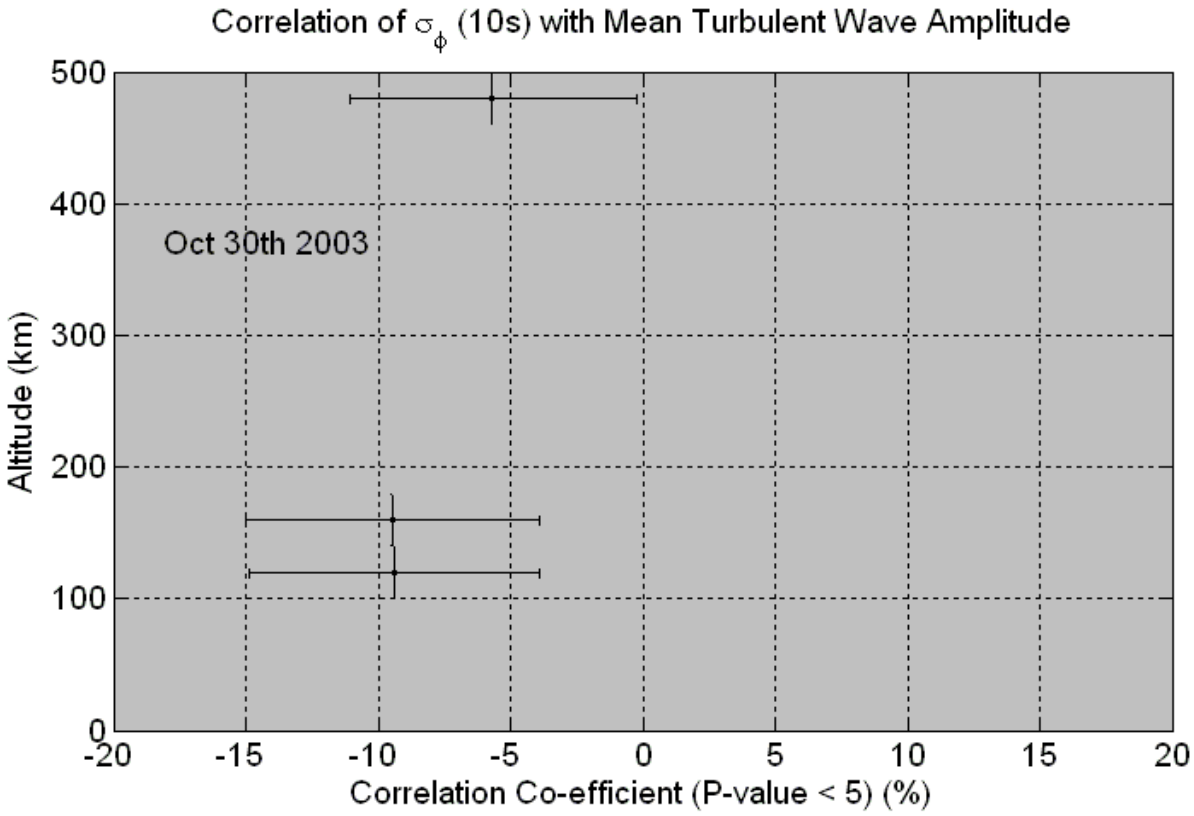

Fig.4.9: Correlation of σ_ϕ(10s) with Modelled Mean Turbulent Wave Amplitude (October 30th 2003 storm).

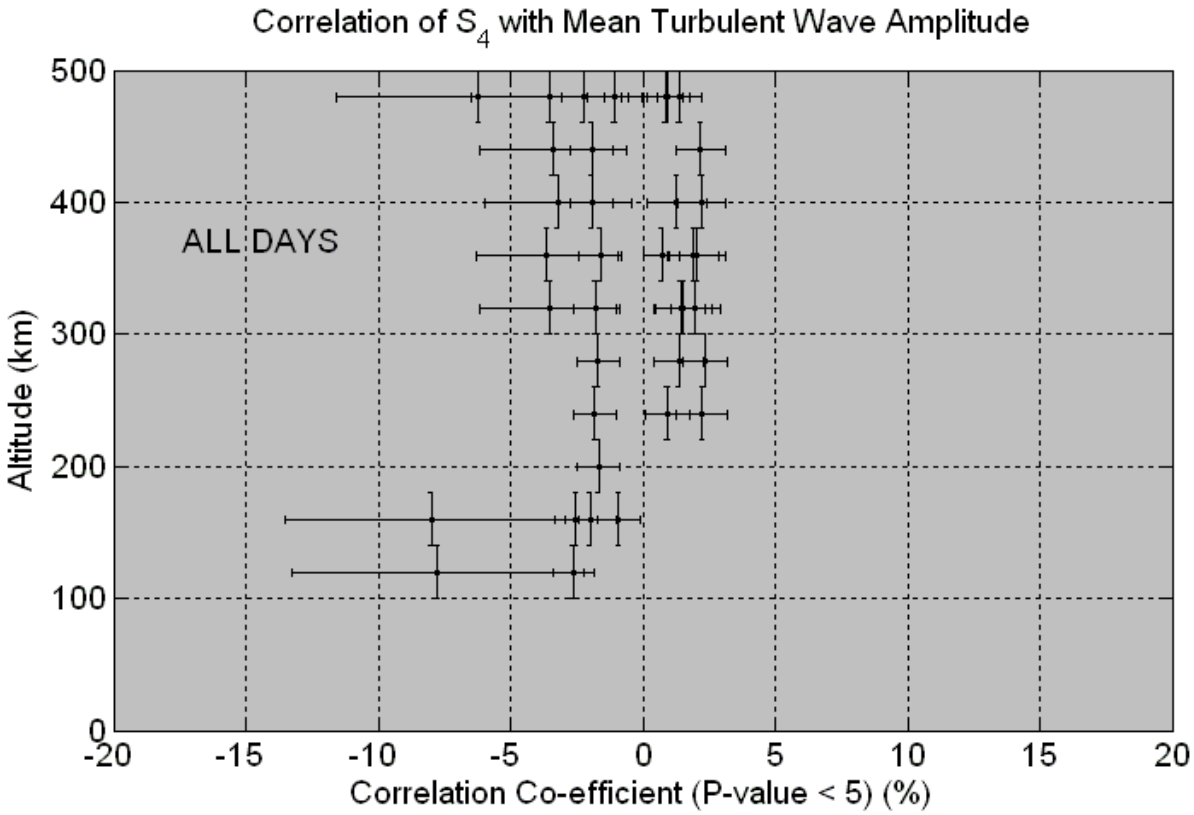

Fig.4.10a: Correlation of S_4 with Modelled Mean Turbulent Wave Amplitude (All Days).

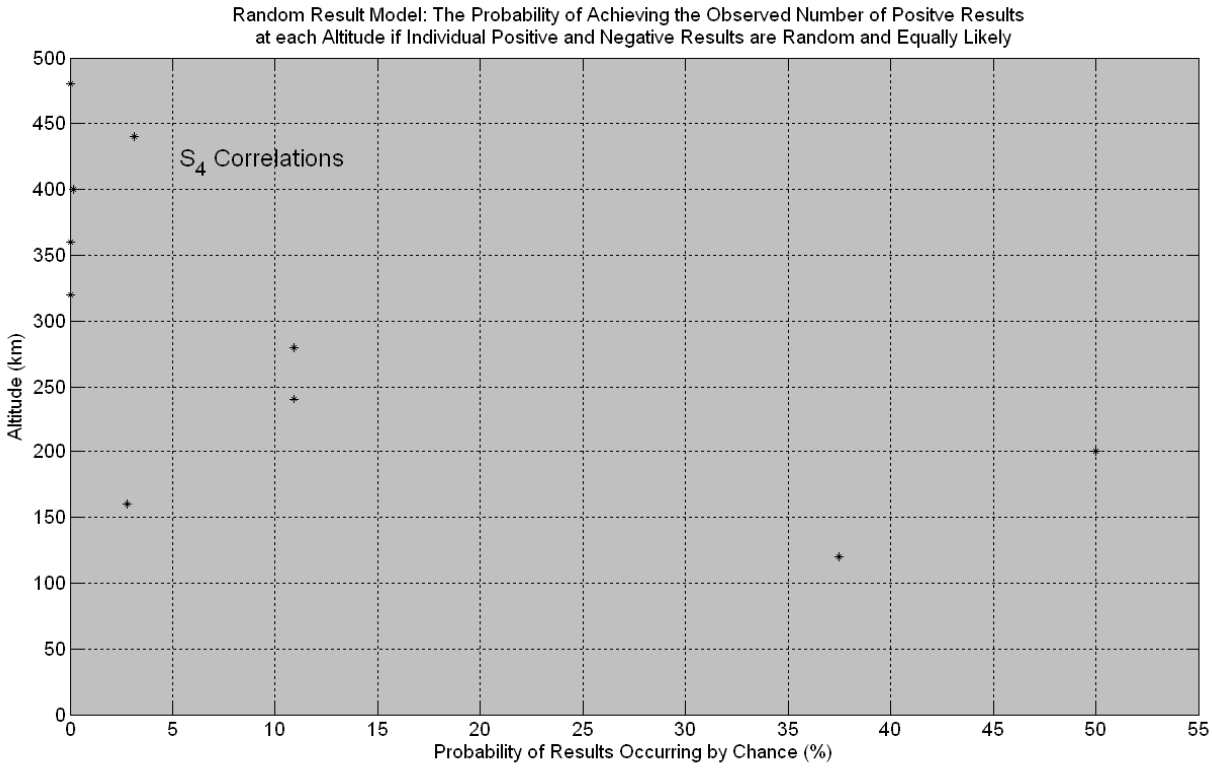

Fig.4.10b: Random Result Model: The probability of achieving the observed number of positive results at each altitude in fig.4.10a if individual positive an negative results are random and equally likely.

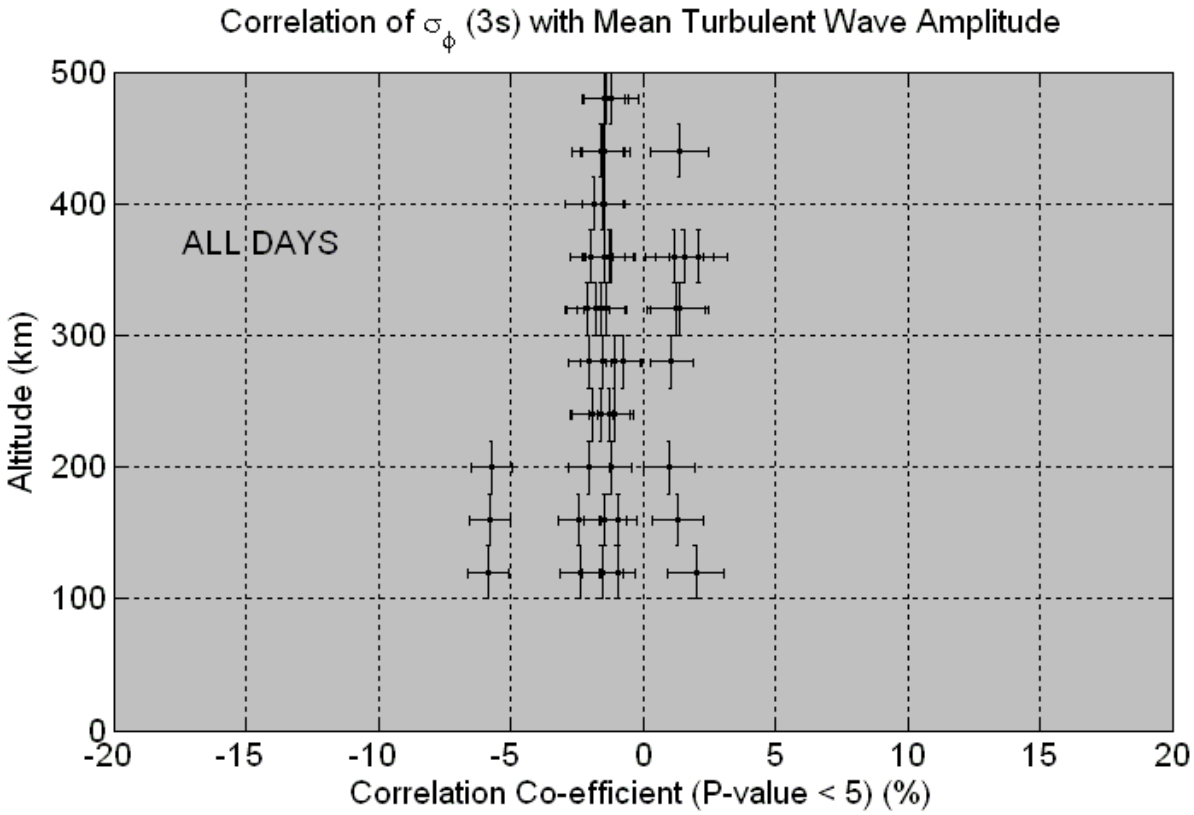

Fig.4.11a: Correlation of σ_ϕ(3s) with Modelled Mean Gradient Drift Wave Amplitude (All Days).

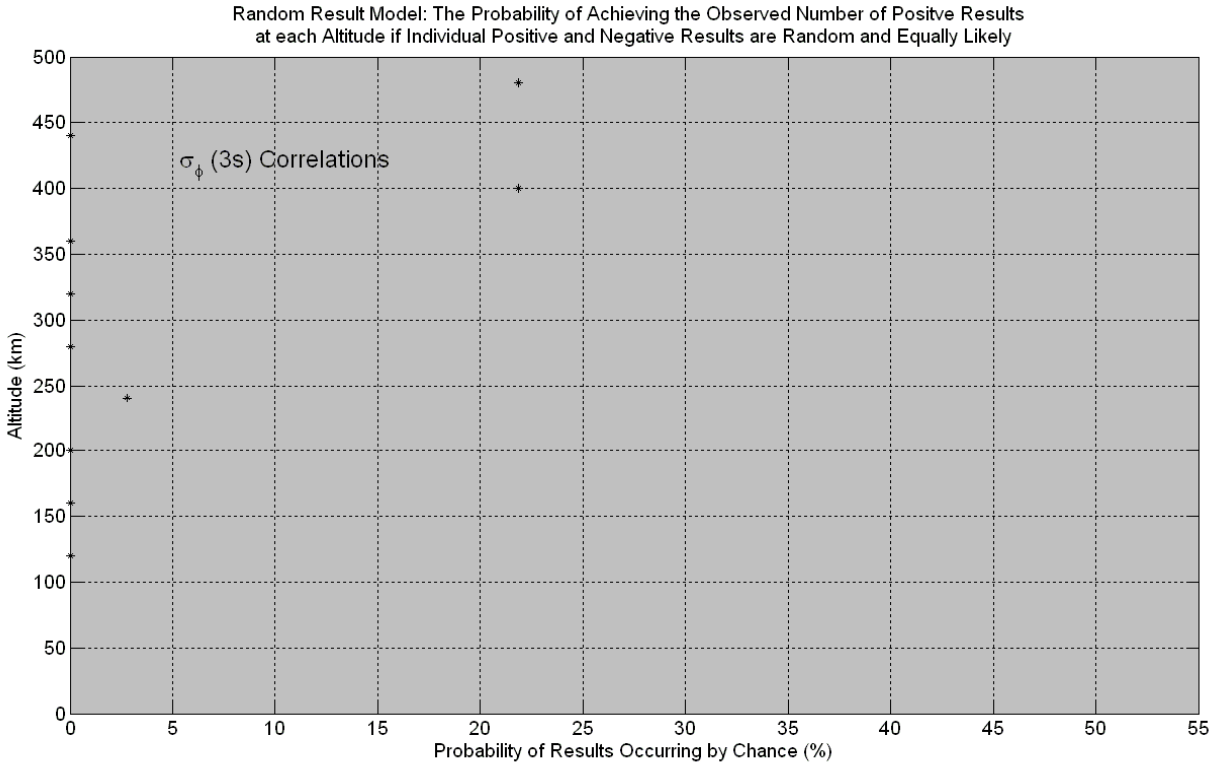

Fig.4.11b: Random Result Model: The probability of achieving the observed number of positive results at each altitude in fig.4.11a if individual positive an negative results are random and equally likely.

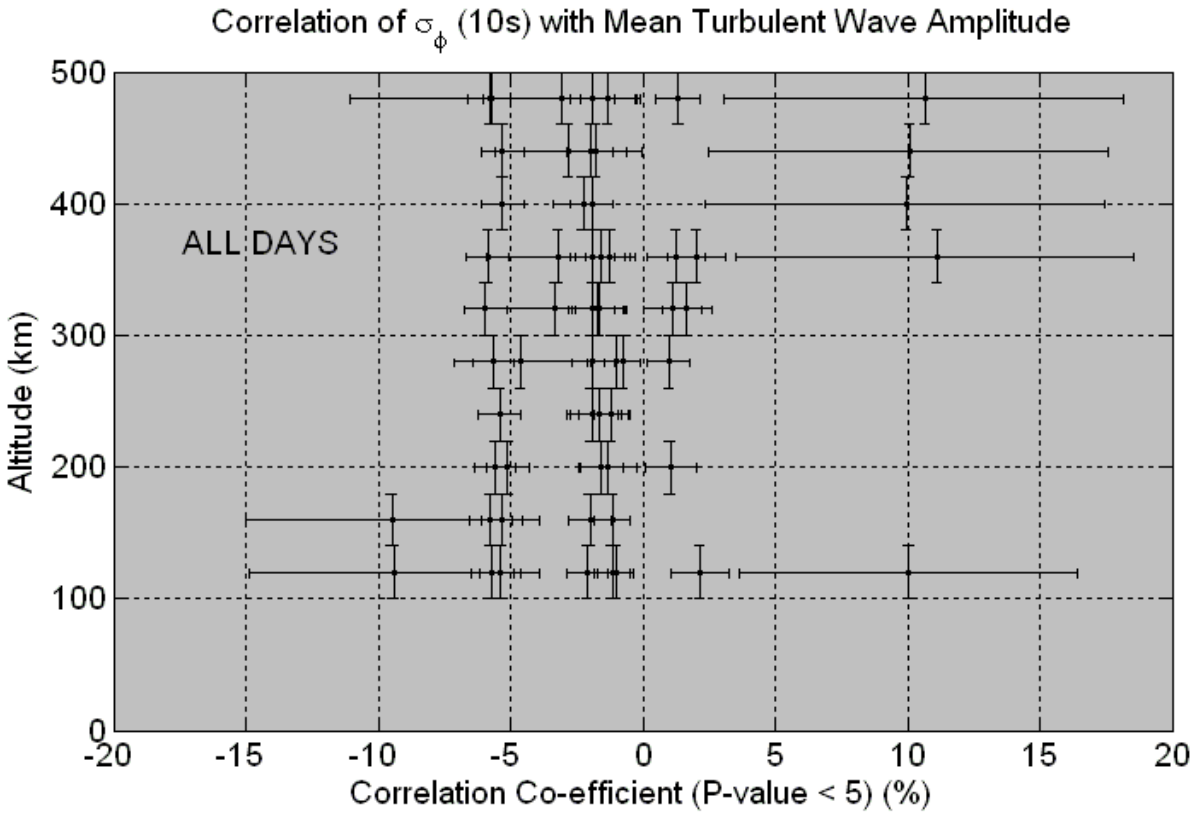

Fig.4.12a: Correlation of σ_ϕ(10s) with Modelled Mean Gradient Drift Wave Amplitude (All Days).

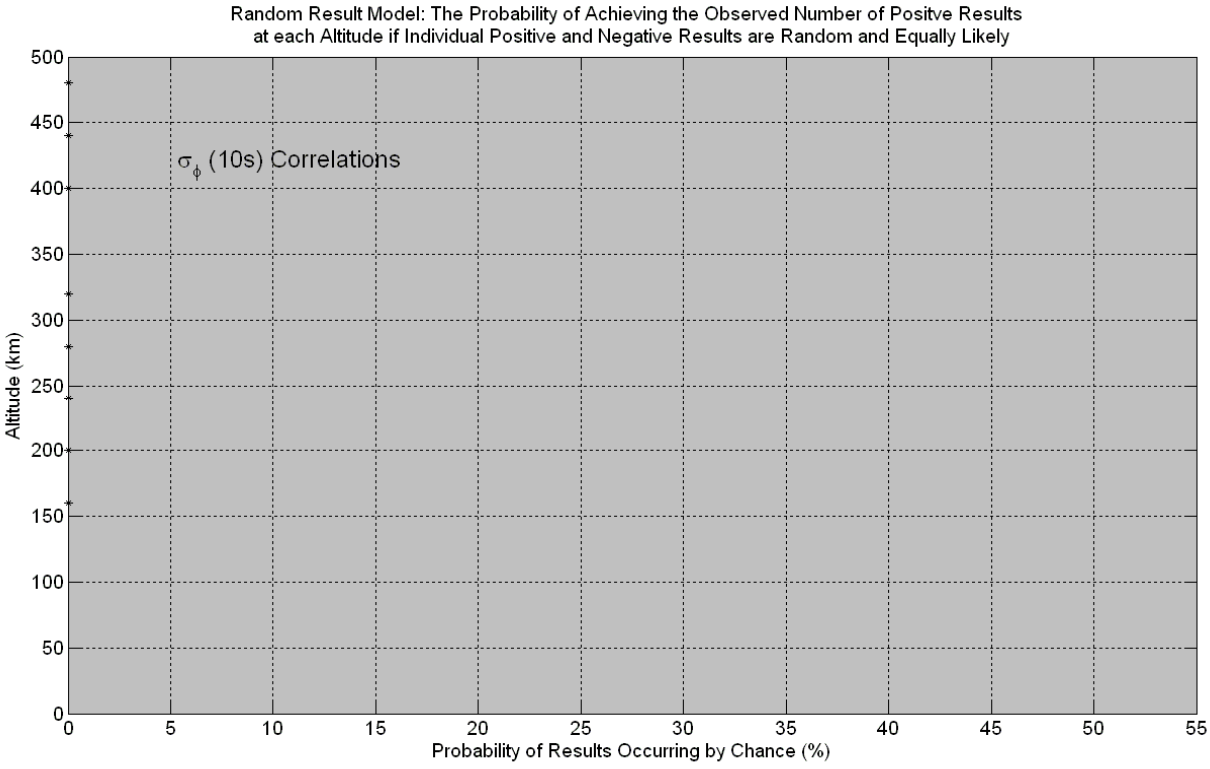

Fig.4.12b: Random Result Model: The probability of achieving the observed number of positive results at each altitude in fig.4.12a if individual positive an negative results are random and equally likely.

Chapter 5: DMSP Velocity Data and the GDI Growth Rate

5.1 Introduction

The Defence Meteorological Satellites Program (DMSP) is run by the United States Air Force. Several of the satellites launched in the program carry instruments useful to ionospheric scientists. These instruments include SSI/ES (Special Sensor for Ions and Electrons), which consists of a Langmuir Probe, a Retarding Potential Analyser, a plasma drift meter and a scintillation monitor. The satellites have polar orbits at approximately 840km altitude [*NGDC*, 2006].

The velocity data are recorded by the plasma drift meter as three mutually perpendicular components, one of which is along the direction of motion of the satellite, another perpendicular to the direction of motion. These data are of interest because they can be used in the model of the GDI growth rate discussed in Chapter 3. As described there, the model implements the equation

$$\gamma_{GD} = \left(v_{\|} \nu_{in} \frac{\nabla n_0}{n_0} \right)^{1/2} \tag{5.1}$$

for every voxel of the MIDAS 2.0 grid, using the Weimer Model to provide values for $v_{\|}$. DMSP SSI/ES velocity data can replace the Weimer Model velocity values with the advantage of being genuine observations of the plasma motion and with the disadvantage of being restricted only to the position of the satellite at any given time. This does, however, allow the possibility of comparing values of γ_{GD} resulting from both sources, along the path of the satellite.

5.2 Method

Data sets from the SSI/ES instrument aboard three satellites (designated f13, f14 and f15) are available for the time periods analysed in previous sections of this thesis. The same time periods are used for this analysis. However, data from satellite f14 is considered unreliable because of an equipment failure so it is not used here. Individual velocity measurements are given a rating from 1 to 3 regarding reliability, with 1 being optimum: no measurements with a reliability rating other than 1 are used in this analysis. The vertical component of the velocity is ignored as the locally horizontal velocity is needed in eqn.(5.1).

The data set for each orbit gives velocity measurements every four seconds along with the satellite altitude, latitude and longitude and universal time. From this information, at any given time, the voxel of the MIDAS 2.0 grid containing the satellite can be calculated. The GDI growth rate can then be calculated for this voxel as described in section 3.2. Using the assumption that geo-magnetic field lines are equipotential lines, the values for γ_{GD} in the voxels along the field line as it approaches the surface of the earth can also be calculated: the plasma drift velocity will have the

same value because neither the magnetic nor electric field strength changes significantly along the field line under this assumption and they are the only variables in the drift velocity equation.

Where more than one velocity measurement is recorded in the same voxel in the same ten minute time interval, the mean of all measurements is taken for use in calculating γ_{GD}. (The MIDAS 2.0 voxel grids update every ten minutes – see section 3.1.)

It is now possible to compare these results with the results for the same time periods and voxels from the original γ_{GD} calculations using the Weimer Model.

5.3 Results

Fig.5.1 shows the GDI growth rates calculated by the model, where DMSP velocity data is available and using that data in the calculation, for all four storm periods analysed in previous chapters. Fig.5.2 shows the GDI growth rates for the same positions and times, using the Weimer Model output to calculate velocities. Points where the growth rate is zero for both the Weimer Model and the corresponding DMSP data based calculations are neglected because in this situation the electron concentration is zero. Comparison of these two figures shows that the DMSP data based calculations can be an order of magnitude bigger than the corresponding Weimer Model based results.

Fig.5.3 is a histogram of the occurrence of GDI growth rates as calculated from DMSP velocity data, using one thousand equal-width bins. Fig.5.4 is the equivalent histogram, using the same number and width of bins, for the Weimer Model based GDI growth rates. It can be seen that both distributions are centred on zero and that the DMSP based values have an inter-quartile range an order of magnitude larger than that for the Weimer Model based values.

5.4 Conclusions

The fact that the inter-quartile range, as well as some individual results, of the GDI growth rates calculated using DMSP velocity data are an order of magnitude larger their equivalents calculated using Weimer Model output, suggests that the GDI growth rates calculated in Chapter 3, are in general smaller in magnitude than they in reality should be. Since the distributions of growth rate values, however calculated, are centred on zero it is very likely that the under-estimate applies equally to positive and negative growth rates.

This under-estimation of the GDI growth rate magnitudes can be explained by the fact that the Weimer Model is a statistical model. Such a model will give more weight to “typical”, that is magnetically quiet, times than to magnetically disturbed times, as quiet conditions prevail much more often. However, all the time periods analysed in this thesis are a-typical; magnetic storm times were chosen. During magnetic storms, electric fields mapped to the ionosphere are stronger; the auroral ovals

are pushed toward the equator and hence the polar-cap regions expand [*Hargreaves*, 1992]. The Weimer Model, weighted toward magnetically quiet conditions, will not accurately reproduce these features and hence the velocities calculated from it will be smaller – ultimately leading to smaller growth rate magnitudes being calculated by the over-all model.

It is not clear what effect this general under-estimation of the GDI growth rate would have on the correlation co-efficients presented in Chapter 3: Larger positive growth rates are countered by larger negative ones and if the velocity of the plasma packets is higher, they will spend less time in the MIDAS 2.0 grid, thus allowing less time for Gradient Drift Waves to build in amplitude when growth rates are positive.

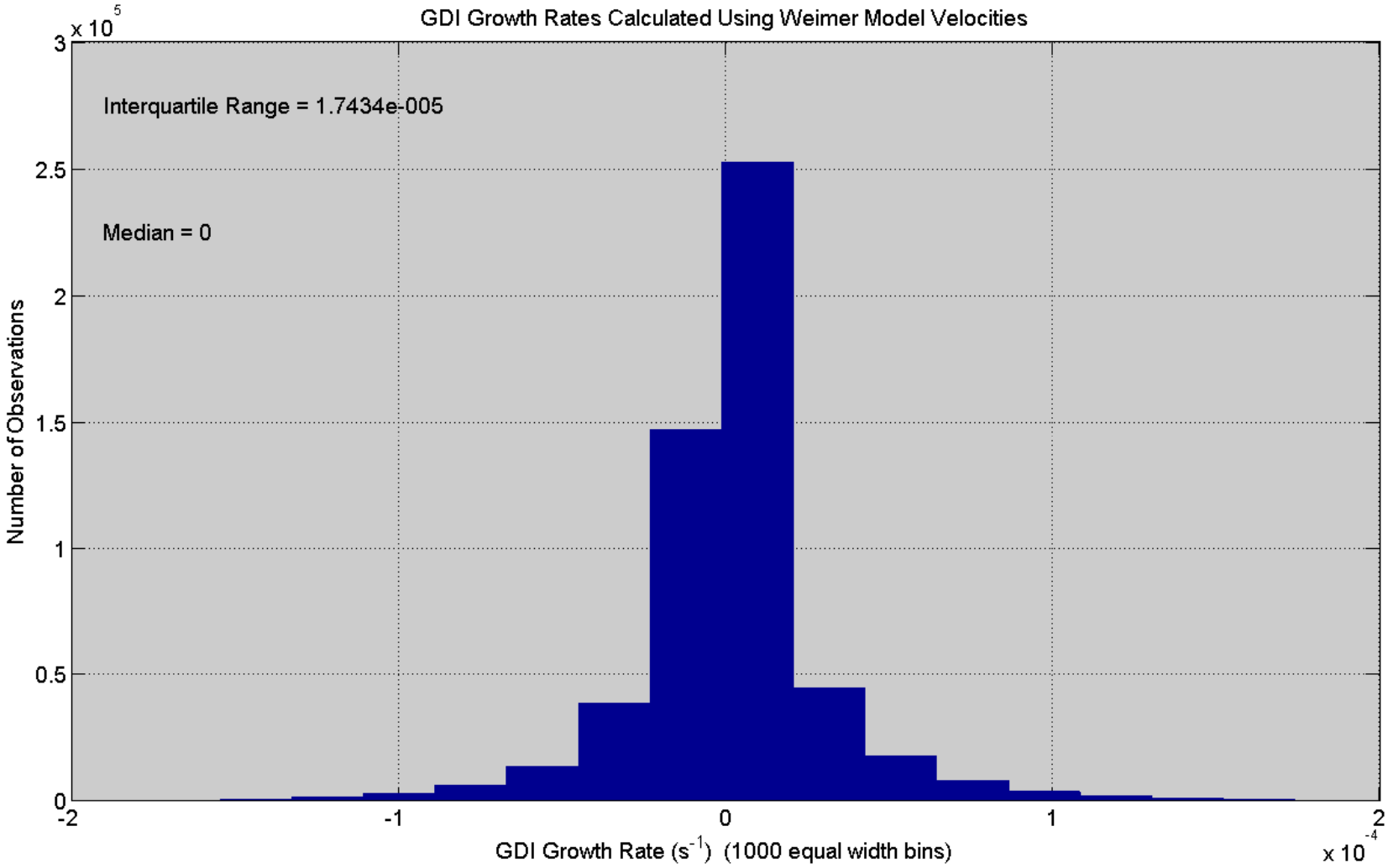

Fig.5.1: GDI growth rate values calculated using the Weimer Model.

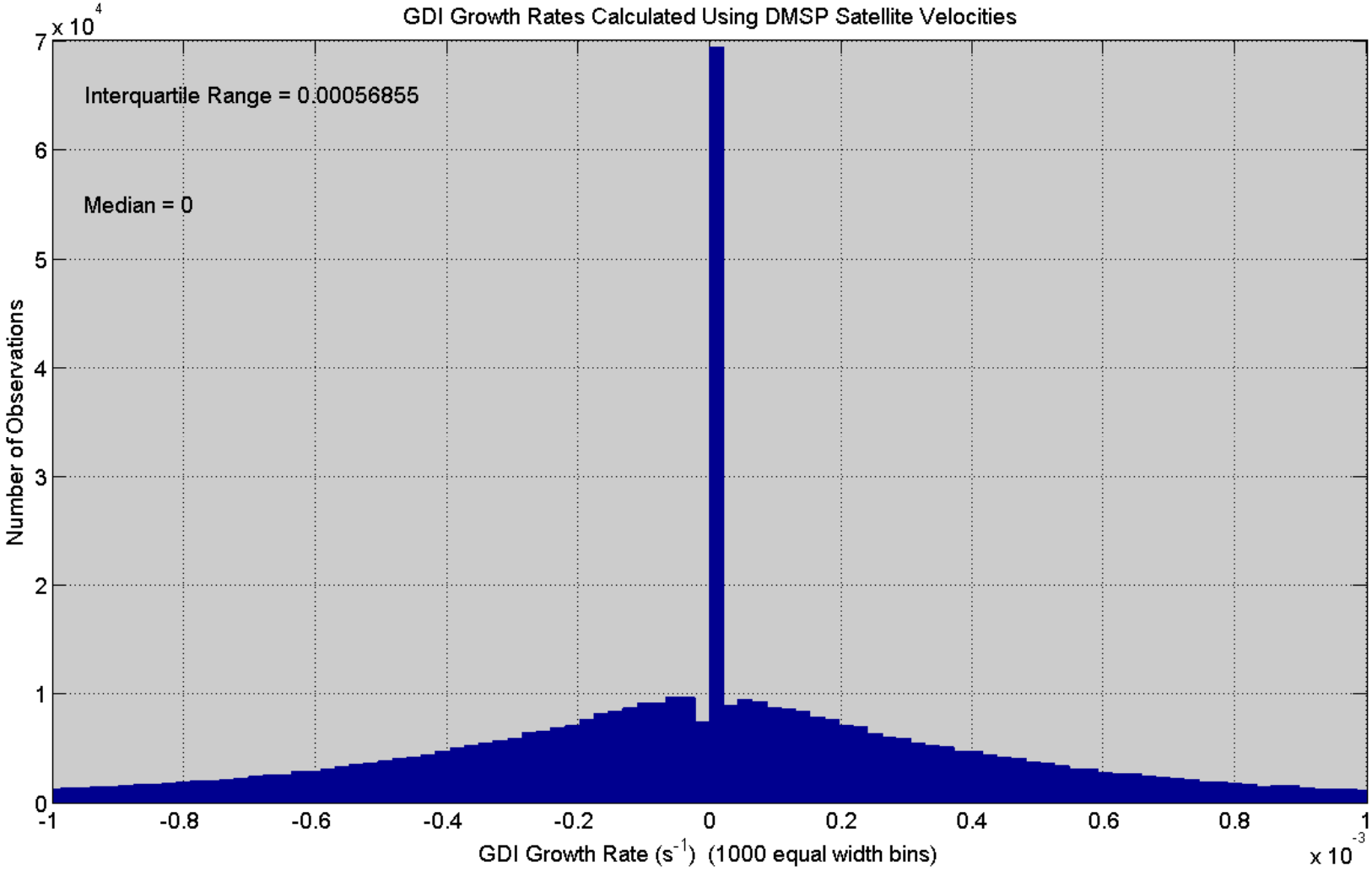

Fig.5.2: GDI growth rate values calculated using DMSP satellite velocity data.

Chapter 6: Conclusions and Future Work

6.1 Conclusions

The modelling approach developed in this thesis, according to the results presented in Chapter 3, shows that, during magnetic storm conditions, the Gradient Drift Instability mechanism of creating plasma irregularities has a weak but significant linear correlation with observed values of the scintillation indices S_4 and σ_ϕ as recorded by L1 band GPS scintillation receivers. The results of Chapter 4 show that turbulent plasma flow impressed on the ionosphere from the magnetosphere by electric field mapping can also show a weak but significant linear correlation, in similar circumstances. Such a correlation is, however, less likely than the correlation with the GDI mechanism. The turbulent process is sometimes (i.e. two out of four storm periods analysed) seen to be approximately as well correlated as the GDI process but never more so.

When the linear correlation co-efficients for the GDI and turbulence processes are approximately equal, one cannot conclude that each process is equally responsible for generating plasma irregularities. The process which has the (consistently) higher mean wave amplitudes will dominate plasma irregularity formation. The correlation co-efficient, as a statistical measure, takes no account of the magnitudes of the data used: It is possible that the mean wave amplitudes calculated for the GDI process could be for the most part larger, smaller or approximately equal to those calculated for the turbulence process, whilst still giving approximately the same value for the correlation co-efficient. Without looking at the mean amplitudes in question one cannot say whether one process is dominating irregularity formation or not. This point is discussed again in 6.2 on future work below.

The use of DMSP data (Chapter 5) suggests that the magnitude of GDI growth rates (whether positive or negative) is under-estimated by the model. This can be explained by the use of the Weimer Model to calculate velocities. The Weimer Model is a statistical model but the time periods under study are all magnetic storm times and therefore a-typical. These a-typical conditions will carry little weight in a statistical model. During a magnetic storm, the auroral oval will move equator-ward and the electric fields imposed on the polar ionosphere will have greater magnitude than during magnetically quiet times [*Hargreaves*, 1992]. Hence the Weimer Model, taking little account of these effects, will tend to under-estimate the magnitude of the electric fields and any velocity calculated from them.

It is not clear what effect this over-all under-estimate of velocities will have on the mean amplitudes of waves calculated by the model and hence on the linear correlation co-efficients: Larger positive growth-rates would tend to increase wave amplitudes but, equally, bigger negative growth rates would

suppress them; higher drift velocities would tend to transport plasma out of the MIDAS 2.0 grid faster, thus allowing less time for wave amplitudes to increase.

Both models give varying results depending on the altitude at which scintillation is assumed to occur. The altitude range 200-440km is realistic for scintillation occurrence in the polar ionosphere. The further outside this range in either direction the lower the likely electron concentration and hence the lower the likelihood of irregularities with significant variations in electron concentration forming. (A steep gradient in electron concentration cannot form if there is nowhere where the electron concentration is high.) Choosing an arbitrary altitude and assuming that all scintillation activity occurs there is not entirely satisfactory, however, and an alternative approach is discussed in the next section.

The research presented in this thesis addresses the question "What mechanism dominates the process of generating plasma irregularities in polar cap patches that cause GPS L1 band scintillation?" Over-all, the results presented suggest that the process of electric-field mapped turbulence generation in the polar ionosphere needs to be studied more thoroughly than here-to-fore, as there may be circumstances when this process is significant in determining the behaviour of plasma in polar cap patches, leading to scintillation of L1 band GPS signals. That said, there are times when the GDI process shows significant correlation and the turbulence process does not, implying that the GDI process is completely dominant at these times. The reliance wherever possible on observational data and particularly on electron concentration data from an assimilative imaging algorithm strengthens this conclusion.

The novel modelling technique developed and presented here has proved successful in elucidating understanding of which physical processes that might lead to L1 band scintillation are active in the polar ionosphere during magnetic storm conditions. This success shows the utility of ionospheric imaging as a tool for research, that efforts to improve the models presented here would be beneficial and that similar modelling approaches should be considered for use in other topics of research.

6.2 Future Work

As there was insufficient time available, only the linear correlation co-efficients between the mean irregularity amplitudes and the observed scintillation indices were assessed. Checking for better correlation at other powers, e.g. in the range 0.5 to 1.5 may be worthwhile.

The models of the GDI and Turbulence growth rates presented in this thesis could both be improved by replacing the assumption of an altitude where scintillation is occurring, at all times and across the entire latitude-longitude are covered by the MIDAS 2.0 grid, with a less arbitrary, more realistic approach. This can be done by instead assuming that the scintillation is occurring at the altitude where the electron concentration is at its highest, as determined along the ray path between the GPS satellite and the scintillation receiver. For example, in

fig.6.1, if the value of n_4 is larger than that of n_1, n_2, n_3, n_5 or n_6, then it would be assumed that scintillation is occurring at the altitude of n_4 and the growth rate would be calculated for that voxel and compared with the scintillation indices recorded for that ray path. This would take into account the likelihood that the peak of electron concentration will vary according to the presence or absence of plasma patches along a particular ray path. The result would be a single correlation co-efficient for each process (GDI and turbulence) that should be more accurate than any one such result from the model as it stands.

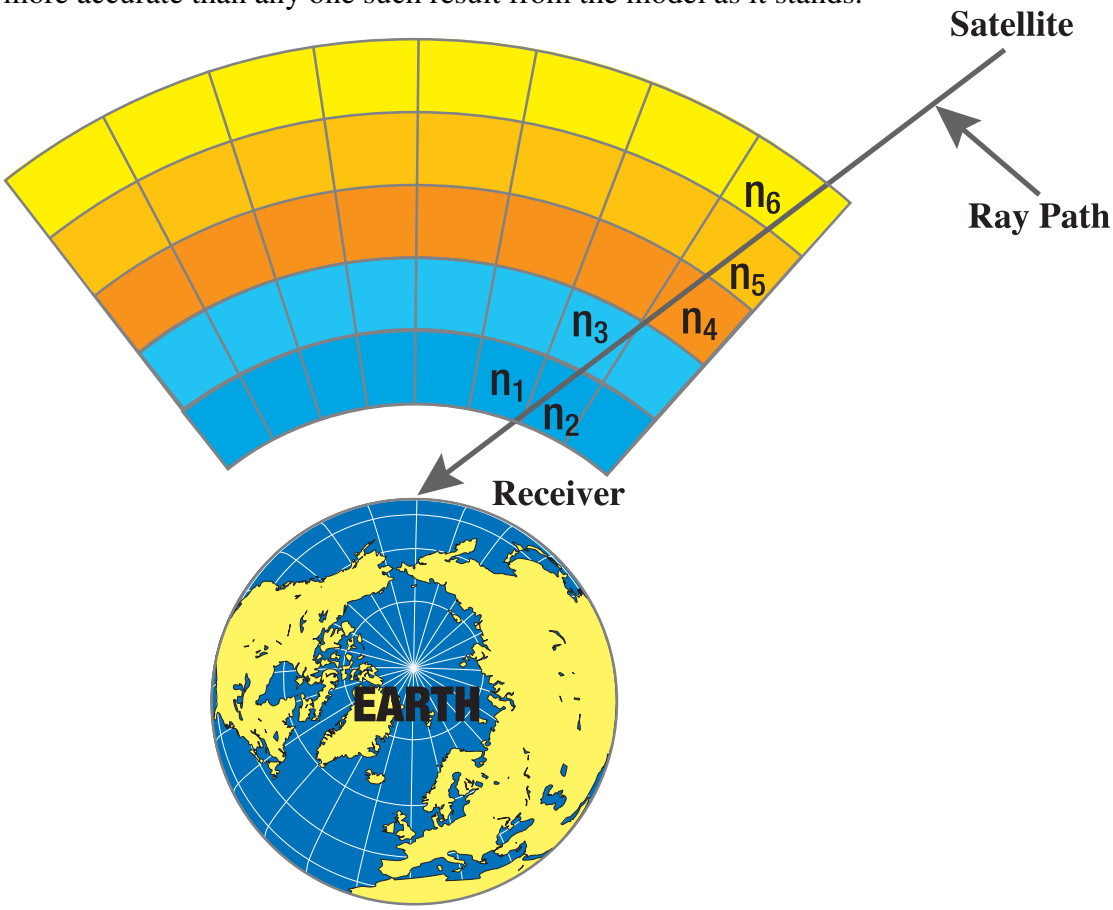

Fig.6.1: Ray path through multiple voxels. Of the voxels traversed, one will have a peak value for electron concentration, n.

Whilst more sophisticated equations exist for calculating growth rates, implementing them for each voxel of the MIDAS 2.0 grid is less likely to improve the accuracy of the models than improving the accuracy of the parameters in the existing equation. The three most important factors in that equation are the n_0, ∇n_0 and the velocity. The first two of these can be improved by having a finer grid for the imaging algorithm, but only if there is sufficient observational data assimilated into the imaging algorithm, otherwise too few voxels contain data from observations and the reconstructed image reverts to that of the background model used by the algorithm. Ionospheric imaging algorithms that adapt the size of voxels to the available assimilated data (i.e. using smaller voxels where more observational data is available) are discussed in [*Bust and Mitchell*, 2008]. Use of such an algorithm would allow the most accurate

knowledge of n_0 and ∇n_0 for any particular region and thus increase the accuracy of the growth rates calculated.

The problem of increasing the accuracy of the velocity figures used is less tractable. The use of DMSP satellite data has demonstrated that the Weimer Model under-estimates plasma drift velocities in magnetic storm conditions. Replacing it with a different model of the polar-cap electric field might improve accuracy but it would be desirable to base plasma drift velocities on some kind of observational data. DMSP or other satellite electric field or plasma drift velocity measurements all suffer from the problem of being limited to the satellite track – universal coverage of the voxel grid in space and time is not possible by this method.

One possible approach is to use the successive output from the imaging algorithm to calculate drift velocities. Instead of calculating growth rates for every voxel in the grid at every time, only values for voxels containing part of a plasma patch would be acquired. The velocity of the patch would be calculated based on its motion between successive reconstructions by the imaging algorithm. (These would be ten minutes apart in the case of the MIDAS 2.0 algorithm used for this thesis.) This leaves open the question of how to define a plasma patch for purposes of tracking its motion, in a way that can be automated. It may be possible to adapt the program "Track" developed by Hodges for automated tracking of low-pressure weather systems to this task [*Bengtsson et al.*, 2006; *Hodges*, 1998; 1999; *Hodges et al.*, 2003; *Hodges*, 2008; *Hopsch et al.*, 2007; *Hoskins and Hodges*, 2005].

The approach of only calculating growth rates for the patches has the added advantage of not diluting the results with growth rates calculated for regions of the grid where there are only very low background levels of ionisation, where irregularities could not in fact form, regardless of the theoretical growth rate.

Finally, with reference to the turbulence model, each calculation of γ_T relies on a value for the constant, β, taken from a graph in [*Mounir et al.*, 1991]. It is used because it is the only value available. (See fig.4.1.) It is, however, exceedingly unlikely that this value is exactly the same in all circumstances. Better knowledge of the turbulent spectrum of the polar-cap electric field would aid this model tremendously. Obtaining the satellite data used by [*Mounir et al.*, 1991] might allow a more flexible or accurate decision to be made regarding the value of β.

The conclusion drawn from the analyses presented here, that turbulence might in some circumstances be of equal significance to the GDI process in determining the way irregularities form in polar cap plasma patches shows a need for further study: turbulence has not been as thoroughly investigated as the GDI process.

One way the work presented here could be further developed, is in examining the values of mean wave amplitude calculated. If the GDI and

turbulence processes show approximately equal linear correlation with observed scintillation index values, it does not automatically follow that each process is equally responsible for generating irregularities. If the mean wave amplitudes calculated for the GDI process are consistently higher than those for the turbulence process, then despite the similar correlation with scintillation indices, the GDI process would control the development of irregularities. If the situation was reversed and wave amplitudes for the turbulence process were consistently higher, then turbulence would be controlling irregularity formation. If the mean wave amplitudes were similar in magnitude, then neither process would be dominating the plasma's behaviour.

It would be helpful to create a numerical model of the turbulence process and compare it with the similar work already done for the GDI case. Does the development of turbulence on a plasma patch show any differences with the development of the GDI on an equivalent patch? Would any such differences be directly observable in any way? Would the irregularity patterns formed affect transmitted L1 band GPS signals in any measurably different way?

In principle, the use of the modelling technique developed here is not restricted to study of polar-cap plasma patches. It may be possible to apply it to the similar questions of how irregularities form in auroral arcs or equatorial plasma bubbles. In each of these cases, the fundamental problem would be how to image the phenomena with sufficient accuracy in the first place. Certainly specific experiments and probably specific imaging algorithms would have to be developed to tackle these questions. In both these cases, optical imaging might be more appropriate than radio imaging.

Any situation where theoretical knowledge of some parameter is required might be amenable to a similar approach, if imaging or tomographic algorithms are available. As an illustrative example (that has not been considered thoroughly), imagine a reconstruction of the Earth's interior, obtained from earthquake wave-propagation data. Theoretical knowledge of plastic flow might be useable to obtain a model of convective circulation in the mantle, having applied the appropriate data to the appropriate flow and deformation equations, for each voxel in the reconstruction.

Appendix 1: Full Derivation of the 1-Dimemensional Rayleigh-Taylor Instability Growth Rate

In order to determine what conditions allow a perturbation to grow and what conditions suppress it, it is usual to try to derive a "growth rate" for the waves. Sometimes a threshold or other condition for unstable growth is apparent when this is done. Growth rate calculations form a crucial aspect of the research presented in later chapters so they are considered in some detail here.

By definition unstable perturbations grow proportionally to $e^{\gamma t}$ where t = time and γ is defined as the growth rate [*Hargreaves*, 1992]. Below, the growth rate γ is derived for the one dimensional Rayleigh – Taylor Instability, in order to illustrate how equations for growth rates can be obtained. In this example a constant magnetic field is attempting to hold up a plasma against the force of gravity. (The following argument is based on that given by [*Chen*, 1984].)

Assume that a wave **k** propagates in the y direction; $\mathbf{k} = k\hat{\mathbf{y}}$. Also assume that there is a constant ion drift velocity $\mathbf{v}_{i0}$ and the wave adds a small perturbation drift, $\mathbf{v}_{i1}$, and then write the equation of motion for the ions. In the unperturbed state:

$$\mathrm{Mn}_0 \left(\mathbf{v}_{i0} \cdot \nabla\right) \mathbf{v}_{i0} = \mathrm{en}_0 \mathbf{v}_{i0} \times \mathbf{B_0} + \mathrm{Mn}_0 \mathbf{g}, \quad (8.1)$$

Where:
M = the mass of one ion
n_o= Background ion concentration
$\mathbf{B_0}$ = Constant magnetic field
g = acceleration due to gravity (assumed constant)
e = charge on one electron.
Eqn.(8.1) is the equation of motion from a stationary perspective, rather than one moving at the fluid velocity. The first objective is to obtain an expression for $\mathbf{v}_{i0}$. Since $\mathbf{v}_{i0}$ is defined as constant, $\left(\mathbf{v}_{i0} \cdot \nabla\right) \mathbf{v}_{i0} = 0$, eqn.(8.1) reduces to

$$0 = \mathrm{en}_0 \mathbf{v}_{i0} \times \mathbf{B_0} + \mathrm{Mn}_0 \mathbf{g}.$$

Taking the cross product with $\mathbf{B_0}$ and solving for $\mathbf{v}_{i0}$:

$$0 = \mathrm{en}_0 \mathbf{v}_{i0} \times \mathbf{B_0} \times \mathbf{B_0} + \mathrm{Mn}_0 \mathbf{g} \times \mathbf{B_0} \Rightarrow 0 = \mathrm{en}_0 \mathbf{v}_{i0} B_0^2 + \mathrm{Mn}_0 \mathbf{g} \times \mathbf{B_0}$$

$\Rightarrow$

$$\mathbf{v}_{i0} = \frac{\mathrm{M}\left(\mathbf{g} \times \mathbf{B_0}\right)}{\mathrm{eB}_0^2} = -\frac{g\hat{\mathbf{y}}}{\Omega_{\mathrm{Ci}}}, \quad (8.2)$$

where $\Omega_{Ci} = eB_0/M$; this is the ion cyclotron frequency, the frequency with which an ion rotates in a uniform magnetic field.

Next we take the ion equation of motion and add the perturbation:

$$\begin{aligned} &M(n_0+n_1)\left[\frac{\partial(\mathbf{v}_{i1}+\mathbf{v}_{i0})}{\partial t}+(\mathbf{v}_{i0}+\mathbf{v}_{i1})\times\nabla(\mathbf{v}_{i0}+\mathbf{v}_{i1})\right]= \\ &e(n_0+n_1)\left[\mathbf{E_1}+(\mathbf{v}_{i0}+\mathbf{v}_{i1})\times\mathbf{B_0}\right]+M(n_0+n_1)\mathbf{g} \end{aligned}, \qquad (8.3)$$

where:

n_1 = perturbation ion concentration

$\mathbf{v}_{i1}$ = perturbation velocity.

From here the ultimate aim is to derive an expression relating to the perturbations that allows us to define a growth-rate for them.

Multiplying eqn.(8.1) by $1+(n_0/n_1)$ gives

$$M(n_0+n_1)(\mathbf{v}_{i0}\cdot\nabla)\mathbf{v}_{i0}=e(n_0+n_1)\mathbf{v}_{i0}\times\mathbf{B_0}+M(n_0+n_1)\mathbf{g}. \qquad (8.4)$$

Subtracting eqn.(8.4) from eqn.(8.1) and neglecting second order terms yields

$$Mn_0\left(\frac{\partial\mathbf{v}_{i1}}{\partial t}+(\mathbf{v}_{i0}\cdot\nabla)\mathbf{v}_{i1}\right)=en_0\left(\mathbf{E_1}+\mathbf{v}_{i1}\times\mathbf{B_0}\right). \qquad (8.5)$$

Now assume that the perturbations have the form $\mathbf{v}_{i1}=\exp[i(ky-\omega t)]$ and $n_1\propto\exp[i(ky-\omega t)]$ i.e. a sine wave, with $i=\sqrt{-1}$ and angular frequency ω.

Substituting for $\mathbf{v}_{i1}$, results in

$$M(\omega-kv_{i0})\mathbf{v}_{i1}=ie(\mathbf{E_1}+\mathbf{v}_{i1}\times\mathbf{B_0}), \qquad (8.6)$$

having performed the differentiation and noticed that $(\mathbf{v}_{i0}\cdot\nabla)\mathbf{v}_{i1}=0$.

To solve this equation, first note that there can be no component of $\mathbf{v}_{i1}$ in the z direction. Next observe that there is no component of $\mathbf{E_1}$ in the x direction. This leaves

$$v_{ix}=\frac{ie}{m(\omega-kv_{i0})}(v_{iy}B_0) \qquad (8.7)$$

and

$$v_{iy}=\frac{ie}{m(\omega-kv_0)}(E_y-v_{ix}B_0). \qquad (8.8)$$

Substituting (8.8) into (8.7) and re-arranging gives

$$v_{ix}\left(1+\frac{e^2B_0^2}{m^2(\omega-kv_{i0})^2}\right)=-\frac{e^2B_0E_y}{m^2(\omega-kv_{i0})^2}. \qquad (8.9)$$

Substituting the ion cyclotron frequency, $\Omega_{Ci}=eB_0/M$ into eqn.(8.9) produces

$$v_{ix}\left(1+\frac{\Omega_{Ci}^2}{(\omega-kv_{i0})^2}\right)=-\frac{\Omega_{Ci}^2E_yB_0}{(\omega-kv_{i0})^2}. \qquad (8.10)$$

Assuming $\Omega_{Ci}^2 \gg (\omega\text{-}kv_{i0})^2$ i.e. $\left(1+\frac{\Omega_{Ci}^2 B_0^2}{(\omega\text{-}kv_{i0})^2}\right) \approx \frac{\Omega_{Ci}^2 B_0^2}{(\omega\text{-}kv_{i0})^2}$ and cancelling quantities where possible, the result is

$$v_{ix} = \frac{-E_y}{B_0}. \tag{8.11}$$

Repeating this process by substituting eqn.(8.7) into eqn.(8.8) with the same assumption that $\Omega_{Ci}^2 \gg (\omega\text{-}kv_{i0})^2$ gives

$$v_{iy} = \frac{iE_y(\omega\text{-}kv_{i0})}{B_0\Omega_{Ci}}. \tag{8.12}$$

Repeating the entire analysis from eqn.(8.1) for the electrons leads to:

$$v_{ex} = \frac{-E_y}{B_0} \tag{8.13}$$

and

$$v_{ey} = \frac{iE_y(\omega\text{-}kv_{e0})}{B_0\Omega_{Ce}} \approx 0$$

which, in comparison to v_{iy}, is so small that it can be neglected entirely:

$$v_{ey} = 0. \tag{8.14}$$

The Continuity Equation states that in a given volume:

> The number of particles entering – the number of particles leaving + the original number of particles = total number of particles.

Put in vector notation, and including perturbations, for the ions this is expressed as

$$\frac{\partial n_1}{\partial t} + \underbrace{\nabla\cdot(n_0 v_{i0})}_{2} + (\mathbf{v}_{io}\cdot\nabla)n_1 + \underbrace{n_1\nabla\cdot\mathbf{v}_{io}}_{4} + (\mathbf{v}_{i1}\cdot\nabla)n_0 + n_0\nabla\cdot\mathbf{v}_{i1} + \underbrace{\nabla\cdot(n_1\mathbf{v}_{i1})}_{7} = 0. \tag{8.15}$$

Term 7 is neglected as it contains only 2nd order components and is assumed to be insignificantly small. Terms 2 and 4 are both zero: Term 2 because $\mathbf{v}_{io}$ and ∇n_0 are perpendicular to each other. Term 4 because $\mathbf{v}_{io}$ is constant.

Remembering that $\mathbf{v}_{i1} \propto \exp[i(ky\text{-}\omega t)]$ and $n_1 \propto \exp[i(ky\text{-}\omega t)]$ we can go ahead and perform the various differentiations, resulting in

$$-i\omega n_1 + ikv_{i0}n_1 + v_{ix}\frac{\partial n_0}{\partial x} + ikn_0 v_{i0} = 0. \tag{8.16}$$

Substituting eqs.(8.11) and (8.12) into eqn.(8.16) and multiplying by $-i$ results in

$$(\omega - kv_{i0})n_1 + i\frac{E_y}{B_0}\frac{\partial n_0}{\partial x} + ikn_0\left(\frac{\omega - kv_{i0}}{\Omega_{Ci}}\right)\frac{E_y}{B_0} = 0. \tag{8.17}$$

Taking eqn.(8.15) and replacing ion quantities with electron quantities then performing the differentiation gives

$$-i\omega n_1 + \underbrace{ikv_{e0}n_1}_{2} + v_{ex}\frac{\partial n_0}{\partial x} + \underbrace{ikn_0 v_{e0}}_{4} = 0,$$

but Terms 2 and 4 = 0 since $v_{e0} = 0$, so

$$-i\omega n_1 + v_{ex}\frac{\partial n_0}{\partial x} = 0. \tag{8.18}$$

Substituting eqn.(8.13) into eqn.(8.18) yields

$$-i\omega n_1 - \frac{E_y}{B_0}\frac{\partial n_0}{\partial x} = 0.$$

Multiplying by $-i$ and re-arranging gives

$$\frac{E_y}{B_0} = \frac{i\omega n_1}{\partial n_0 / \partial x} \tag{8.19}$$

Now substitute eqn.(8.19) into eqn.(8.17):

$$(\omega - kv_{i0})n_1 - \omega n_1 - kn_0\left(\frac{\omega - kv_{i0}}{\Omega_{Ci}}\right)\frac{\omega n_1}{\partial n_0 / \partial x} = 0. \tag{8.20}$$

This simplifies to

$$(\omega\text{-}kv_{i0}) - \left(1 + kn_0\frac{(\omega\text{-}kv_{i0})}{\Omega_{Ci}(\partial n_0 / \partial x)}\right)\omega = 0$$

by dividing by n_1 and pulling out a factor of ω. This can be re-arranged to

$$\omega(\omega - kv_{i0}) = -\frac{v_{i0}\Omega_{Ci}}{n_1}\frac{\partial n_0}{\partial x}. \tag{8.21}$$

A final substitution, from eqn.(8.2) leaves

$$\omega(\omega - kv_{i0}) = \frac{g}{\Omega_{Ci}}\frac{\Omega_{Ci}}{n_1}\frac{\partial n_0}{\partial x}.$$

This needs to be solved for ω:

$$\omega^2 - kv_{i0}\omega - \frac{g(\partial n_0 / \partial x)}{n_0} = 0 \tag{8.22}$$

The quadratic, eqn.(8.22) has solutions

$$\omega = \frac{1}{2}kv_{i0} \pm \left(\frac{1}{4}k^2 v_{i0}^2 + g\frac{(\partial n_0 / \partial x)}{n_0}\right)^{1/2}. \tag{8.23}$$

The only unstable solutions are those with an imaginary component i.e. when

$$-g\frac{(\partial n_0 / \partial x)}{n_0} > \frac{1}{4}k^2 v_{i0}^2 \tag{8.24}$$

and the growth rate is defined as the imaginary part:

$$\gamma = \mathrm{Im}(\omega) \approx \left(-g\frac{(\partial n_0 / \partial x)}{n_0}\right)^{1/2}. \tag{8.25}$$

There are two significant results from this analysis, one is an instability condition, eqn.(8.24), the other is the instability growth rate, eqn.(8.25).

Equation (8.24) states the circumstances in which we can expect unstable growth of perturbations; equation (8.25) indicates how fast those perturbations will grow.

In this analysis **g** was defined as the acceleration due to gravity but nothing in the derivation relies on this; some force **g** has to be present and directed perpendicularly to both $\mathbf{B_0}$ and $\mathbf{v}_{i0}$, but the nature of this force is irrelevant to the result so long as it is constant. This means that driving forces other than gravity can give rise to very similar unstable behaviour if the relative geometry of the forces and fields is the same: The case of the ionospheric Gradient Drift Instability is an important example with gravity replaced by an electric field and the resulting irregularities propagating horizontally rather than vertically.

Appendix 2: Correlation of Mean Gradient Drift Wave Amplitude with Scintillation Indices: Full Results

The full results for all days analysed are tabulated in the subsequent pages of this appendix.

Table 8.1: Storm 1, Day 1 Results.

Storm 1, Day 1: 30th October 2003							
Assumed IPP Altitude		S_4	σ_ϕ(1s)	σ_ϕ(3s)	σ_ϕ(10s)	σ_ϕ(30s)	σ_ϕ(60s)
120 ± 20km	Correlation Co-efficient	5.50	No data	No data	5.65	5.65	No data
	Upper 95% Confidence Limit	10.4	No data	No data	10.5	10.5	No data
	Lower 95% Confidence Limit	0.59	No data	No data	0.75	0.75	No data
	P - Value	2.81	No data	No data	2.39	2.40	No data
160 ± 20km	Correlation Co-efficient	9.44	No data	No data	10.6	10.5	No data
	Upper 95% Confidence Limit	14.31	No data	No data	15.4	15.4	No data
	Lower 95% Confidence Limit	4.53	No data	No data	5.64	5.64	No data
	P - Value	0.0172	No data	No data	0.00270	0.0027	No data
200 ± 20km	Correlation Co-efficient	7.99	No data	No data	10.8	10.8	No data
	Upper 95% Confidence Limit	13.0	No data	No data	15.8	15.8	No data
	Lower 95% Confidence Limit	2.95	No data	No data	5.81	5.82	No data
	P - Value	0.193	No data	No data	0.00250	0.00250	No data
240 ± 20km	Correlation Co-efficient	-1.72	No data	No data	-1.87	-1.87	No data
	Upper 95% Confidence Limit	3.40	No data	No data	3.26	3.25	No data
	Lower 95% Confidence Limit	-6.84	No data	No data	-6.98	-6.98	No data
	P - Value	51.0	No data	No data	47.51	47.5	No data
280 ± 20km	Correlation Co-efficient	1.53	No data	No data	1.53	1.53	No data
	Upper 95% Confidence Limit	6.77	No data	No data	6.77	6.77	No data
	Lower 95% Confidence Limit	-3.71	No data	No data	-3.71	-3.71	No data
	P - Value	56.7	No data	No data	56.8	56.7	No data
320 ± 20km	Correlation Co-efficient	3.21	No data	No data	3.96	3.97	No data
	Upper 95% Confidence Limit	8.47	No data	No data	9.22	9.22	No data
	Lower 95% Confidence Limit	-2.07	No data	No data	-1.32	-1.31	No data
	P - Value	23.3	No data	No data	14.1	14.1	No data

Storm 1, Day 1: 30th October 2003 Continued							
360 ± 20km	Correlation Co-efficient	2.34	No data	No data	1.58	1.58	No data
	Upper 95% Confidence Limit	7.60	No data	No data	6.85	6.85	No data
	Lower 95% Confidence Limit	-2.93	No data	No data	-3.69	-3.69	No data
	P - Value	38.4	No data	No data	55.6	55.7	No data
400 ± 20km	Correlation Co-efficient	11.47	No data	No data	12.5	12.5	No data
	Upper 95% Confidence Limit	16.6	No data	No data	17.7	17.7	No data
	Lower 95% Confidence Limit	6.24	No data	No data	7.31	7.31	No data
	P - Value	0.00190	No data	No data	0.000300	0.000300	No data
440 ± 20km	Correlation Co-efficient	2.75	No data	No data	2.91	2.91	No data
	Upper 95% Confidence Limit	8.03	No data	No data	8.20	8.19	No data
	Lower 95% Confidence Limit	-2.55	No data	No data	-2.39	-2.40	No data
	P - Value	31.0	No data	No data	28.2	28.3	No data
480 ± 20km	Correlation Co-efficient	1.20	No data	No data	0.744	0.740	No data
	Upper 95% Confidence Limit	6.47	No data	No data	6.01	6.00	No data
	Lower 95% Confidence Limit	-4.07	No data	No data	-4.53	-4.53	No data
	P - Value	65.4	No data	No data	78.2	78.3	No data

Table 8.2: Storm 2 Day 1 Results.

Storm 2, Day 1: 24th July 2004							
Assumed IPP Altitude		S_4	σ_ϕ(1s)	σ_ϕ(3s)	σ_ϕ(10s)	σ_ϕ(30s)	σ_ϕ(60 s)
120 ± 20km	Correlation Co-efficient	-0.387	-0.491	-0.657	-0.641	-0.640	-0.640
	Upper 95% Confidence Limit	0.40	0.300	0.135	0.151	0.152	0.152
	Lower 95% Confidence Limit	-1.18	-1.28	-1.45	-1.43	-1.43	-1.43
	P - Value	33.6	22.4	10.4	11.3	11.3	11.3
160 ± 20km	Correlation Co-efficient	-1.80	-0.525	-0.509	-0.421	-0.419	-0.419
	Upper 95% Confidence Limit	-.679	0.601	0.618	0.706	0.708	0.708
	Lower 95% Confidence Limit	-2.92	-1.65	-1.64	-1.55	-1.55	-1.55
	P - Value	0.166	36.1	37.6	46.4	46.6	46.6
200 ± 20km	Correlation Co-efficient	-1.35	-0.542	-0.587	-0.559	-0.558	-0.558
	Upper 95% Confidence Limit	-0.114	0.694	-1.82	1.19	0.680	0.680
	Lower 95% Confidence Limit	-2.58	-1.78	0.65	-1.80	-1.79	-1.80
	P - Value	3.22	39.0	35.2	37.6	37.7	37.7
240 ± 20km	Correlation Co-efficient	-0.296	0.0793	0.182	0.0984	0.0967	0.0976
	Upper 95% Confidence Limit	0.792	1.17	1.27	1.19	1.19	1.19
	Lower 95% Confidence Limit	-1.38	-0.101	-0.909	-0.992	-0.993	-0.993
	P - Value	59.4	88.7	74.4	86.0	86.1	86.1
280 ± 20km	Correlation Co-efficient	0.591	-0.0942	-0.498	-0.539	-0.539	-0.539
	Upper 95% Confidence Limit	1.68	0.994	0.591	0.549	0.550	0.549
	Lower 95% Confidence Limit	-0.500	-1.18	-1.59	-1.63	-1.63	-1.63
	P - Value	28.6	86.5	37.0	33.2	33.2	33.2
320 ± 20km	Correlation Co-efficient	1.14	0.136	-0.238	-0.119	-0.118	-0.119
	Upper 95% Confidence Limit	2.22	1.22	1.06	0.962	0.964	0.963
	Lower 95% Confidence Limit	0.0595	-0.945	-1.11	-1.20	-1.20	-1.20
	P - Value	3.87	80.5	96.6	82.9	83.0	82.9

Storm 2, Day 1: 24th July 2004 Continued							
360 ± 20km	Correlation Co-efficient	1.06	-0.167	-.0289	-0.336	-0.336	-0.336
	Upper 95% Confidence Limit	5.48	0.917	0.796	0.748	0.752	0.748
	Lower 95% Confidence Limit	-0.0216	-1.25	-1.37	-1.42	-1.42	-1.42
	P - Value	5.48	76.3	60.2	54.3	54.4	54.3
400 ± 20km	Correlation Co-efficient	-0.543	-0.465	-0.302	-0.332	-0.331	-0.332
	Upper 95% Confidence Limit	0.538	0.618	0.781	0.751	0.752	0.752
	Lower 95% Confidence Limit	-1.62	-1.55	-1.39	-1.42	-1.14	-1.41
	P - Value	32.5	40.0	58.4	54.8	54.9	54.8
440 ± 20km	Correlation Co-efficient	-0.705	0.193	-0.222	-0.487	-0.0447	-0.0440
	Upper 95% Confidence Limit	0.631	1.53	1.12	1.29	1.30	1.30
	Lower 95% Confidence Limit	-2.04	-1.15	-1.56	-1.39	-1.38	-1.39
	P - Value	30.1	77.8	74.5	94.3	94.8	94.9
480 ± 20km	Correlation Co-efficient	1.46	-0.0204	-0.172	-2.68	-0.271	-0.272
	Upper 95% Confidence Limit	2.45	0.979	0.830	0.732	0.729	0.728
	Lower 95% Confidence Limit	0.460	-1.02	-1.17	-1.27	-1.27	-1.27
	P - Value	0.42	96.7	73.6	59.9	59.6	59.5

Table 8.3: Storm 2 Day 2 Results.

Storm 2, Day 2: 25th July 2004							
Assumed IPP Altitude		S_4	σ_ϕ(1s)	σ_ϕ(3s)	σ_ϕ(10s)	σ_ϕ(30s)	σ_ϕ(60s)
120 ± 20km	Correlation Co-efficient	0.262	-0.686	-0.860	-1.05	-1.05	-1.05
	Upper 95% Confidence Limit	1.08	0.135	-0.0385	-1.87	-1.87	-1.87
	Lower 95% Confidence Limit	-0.557	-1.51	-1.68	-0.223	-0.223	-0.225
	P - Value	53.1	10.2	4.02	1.27	1.27	1.26
160 ± 20km	Correlation Co-efficient	1.21	-0.186	-0.234	-0.219	-0.218	-0.217
	Upper 95% Confidence Limit	2.03	0.639	0.591	-1.05	-1.04	-1.04
	Lower 95% Confidence Limit	0.386	-1.01	-1.06	0.607	0.608	0.609
	P - Value	0.40	65.8	57.8	60.4	60.5	60.7
200 ± 20km	Correlation Co-efficient	-0.0146	0.297	0.346	1.00	1.00	1.00
	Upper 95% Confidence Limit	1.29	1.60	1.65	-0.307	-0.307	-0.306
	Lower 95% Confidence Limit	-1.31	-1.01	-0.960	2.31	2.31	2.31
	P - Value	98.2	65.6	60.4	13.4	13.4	13.3
240 ± 20km	Correlation Co-efficient	0.517	0.785	0.753	1.00	0.991	0.993
	Upper 95% Confidence Limit	1.67	1.94	1.91	-0.154	-0.165	-0.162
	Lower 95% Confidence Limit	-0.636	-0.370	-0.402	2.16	2.15	2.15
	P - Value	38.0	18.3	20.1	8.95	9.29	9.20
280 ± 20km	Correlation Co-efficient	0.422	-0.05	-0.316	-0.901	-0.910	-0.910
	Upper 95% Confidence Limit	1.80	1.34	1.07	-2.29	-2.30	-2.30
	Lower 95% Confidence Limit	-0.962	-1.44	-1.70	0.490	0.481	0.481
	P - Value	55.0	94.2	65.5	20.4	20.0	20.0
320 ± 20km	Correlation Co-efficient	-0.425	-0.627	-0.595	-0.722	-0.726	-0.724
	Upper 95% Confidence Limit	0.703	0.502	0.535	-1.85	-1.86	-1.86
	Lower 95% Confidence Limit	-1.55	-1.76	-1.73	0.409	0.405	0.407
	P - Value	46.0	27.6	30.2	21.1	20.8	20.9

Storm 2, Day 2: 25th July 2004 Continued							
360 ± 20km	Correlation Co-efficient	0.0839	-1.08	-1.02	-2.40	-2.40	-2.40
	Upper 95% Confidence Limit	1.47	0.320	0.372	-3.79	-3.80	-3.80
	Lower 95% Confidence Limit	-1.31	-2.47	-2.42	-1.00	-1.01	-1.01
	P - Value	90.6	13.1	15.1	0.0768	0.0753	0.0753
400 ± 20km	Correlation Co-efficient	0.0756	-1.29	-1.22	-2.48	-2.48	-2.48
	Upper 95% Confidence Limit	1.36	0.000800	0.0750	-3.78	-3.77	-3.77
	Lower 95% Confidence Limit	-1.21	-2.59	-2.51	-1.19	-1.19	-1.18
	P - Value	90.8	5.01	6.49	0.0170	0.0173	0.0175
440 ± 20km	Correlation Co-efficient	-0.0404	0.00710	0.148	0.0656	0.0836	0.0931
	Upper 95% Confidence Limit	94.3	1.11	1.25	-1.04	-1.02	-1.01
	Lower 95% Confidence Limit	-1.14	-1.10	-0.958	1.17	1.19	1.20
	P - Value	1.063	99.0	79.3	90.8	88.2	86.9
480 ± 20km	Correlation Co-efficient	-1.21	-0.7225	-0.634	-0.628	-0.627	-0.626
	Upper 95% Confidence Limit	-0.186	0.303	0.392	-1.66	-1.65	-1.65
	Lower 95% Confidence Limit	-2.23	-1.75	-1.66	0.40	0.401	0.402
	P - Value	2.05	16.7	22.6	23.1	23.2	23.3

Table 8.4: Storm 2 Day 3 Results.

Storm 2, Day 3: 26th July 2004							
Assumed IPP Altitude		S_4	σ_ϕ(1s)	σ_ϕ(3s)	σ_ϕ(10s)	σ_ϕ(30s)	σ_ϕ(60s)
120 ± 20km	Correlation Co-efficient	-0.429	-0.237	-0.290	-0.404	-0.403	-0.403
	Upper 95% Confidence Limit	0.345	-1.01	-1.07	-1.18	-1.18	-1.18
	Lower 95% Confidence Limit	-1.20	0.538	0.484	0.372	0.373	0.373
	P - Value	27.7	54.9	46.3	30.8	30.9	30.8
160 ± 20km	Correlation Co-efficient	0.665	-0.185	-0.319	-0.416	-0.417	-0.417
	Upper 95% Confidence Limit	-0.441	-1.29	-1.43	-1.53	-1.53	-1.53
	Lower 95% Confidence Limit	1.77	0.924	0.790	0.694	0.694	0.694
	P - Value	23.9	74.3	57.3	46.3	46.2	46.2
200 ± 20km	Correlation Co-efficient	0.766	-0.364	-0.392	-0.00784	-0.00881	-0.00962
	Upper 95% Confidence Limit	-0.328	-1.46	-1.49	-1.10	-1.11	-1.11
	Lower 95% Confidence Limit	1.86	0.73	0.703	1.09	1.09	1.09
	P - Value	17.0	51.4	48.3	98.9	98.7	98.6
240 ± 20km	Correlation Co-efficient	0.692	-0.391	-0.319	-0.670	-0.670	-0.670
	Upper 95% Confidence Limit	-0.392	-1.48	-1.40	-1.76	-1.76	-1.76
	Lower 95% Confidence Limit	1.78	0.694	0.767	0.417	0.417	0.416
	P - Value	21.1	48.0	56.5	22.7	22.7	22.7
280 ± 20km	Correlation Co-efficient	0.732	0.00885	0.197	0.143	0.136	0.136
	Upper 95% Confidence Limit	-0.348	-1.07	-0.885	-0.939	-0.946	-0.947
	Lower 95% Confidence Limit	1.81	1.09	1.28	1.23	1.22	1.22
	P - Value	18.4	98.7	72.2	79.6	80.5	80.6
320 ± 20km	Correlation Co-efficient	-0.472	-1.34	-1.51	-2.09	-2.08	-2.09
	Upper 95% Confidence Limit	-1.54	-2.41	-2.58	-3.16	-3.15	-3.15
	Lower 95% Confidence Limit	0.592	-0.278	-0.446	-1.03	-1.02	-1.02
	P - Value	38.4	1.35	0.543	0.0119	0.0127	0.0127

Storm 2, Day 3: 26th July 2004 Continued							
360 ± 20km	Correlation Co-efficient	-0.00300	-0.742	-0.620	0.0347	0.0311	0.0334
	Upper 95% Confidence Limit	-1.07	-1.82	-1.69	-1.04	-1.04	-1.04
	Lower 95% Confidence Limit	1.07	0.331	0.453	1.11	1.11	1.11
	P - Value	99.7	17.5	25.7	95.0	95.5	95.1
400 ± 20km	Correlation Co-efficient	-0.483	-1.23	-0.999	-0.928	-0.923	-0.923
	Upper 95% Confidence Limit	-1.56	-2.31	-2.08	-2.01	-2.01	-2.01
	Lower 95% Confidence Limit	0.599	-0.148	0.0843	0.156	0.161	0.161
	P - Value	38.2	2.59	7.07	9.34	9.51	9.52
440 ± 20km	Correlation Co-efficient	-0.483	-0.954	-0.827	-0.830	-0.826	-0.826
	Upper 95% Confidence Limit	-1.57	-2.04	-1.91	-1.91	-1.91	-1.91
	Lower 95% Confidence Limit	0.602	0.132	0.260	0.257	0.261	0.261
	P - Value	38.3	8.53	13.6	13.4	13.6	13.6
480 ± 20km	Correlation Co-efficient	-0.119	-0.0400	0.00997	0.374	0.371	0.371
	Upper 95% Confidence Limit	-1.10	-1.02	-0.970	-0.608	-0.611	-0.611
	Lower 95% Confidence Limit	0.859	0.940	0.990	1.36	1.35	1.35
	P - Value	81.1	93.6	98.4	45.5	45.9	45.9

Table 8.5: Storm 2 Day 4 Results.

Storm 2, Day 4: 27th July 2004							
Assumed IPP Altitude		S_4	σ_ϕ(1s)	σ_ϕ(3s)	σ_ϕ(10s)	σ_ϕ(30s)	σ_ϕ(60s)
120 ± 20km	Correlation Co-efficient	0.595	-0.52	-0.535	-0.300	-0.297	-0.293
	Upper 95% Confidence Limit	-0.200	-1.31	-1.33	-1.09	-1.09	-1.09
	Lower 95% Confidence Limit	1.39	0.274	0.260	0.495	0.497	0.502
	P - Value	14.1	19.9	18.7	46.0	46.3	47.0
160 ± 20km	Correlation Co-efficient	0.707	-0.511	-0.605	-0.644	-0.644	-0.644
	Upper 95% Confidence Limit	-0.0887	-1.31	-1.40	-1.44	-1.44	-1.44
	Lower 95% Confidence Limit	1.50	0.285	0.191	0.153	0.152	0.153
	P - Value	8.16	20.9	13.6	11.3	11.3	11.3
200 ± 20km	Correlation Co-efficient	0.293	1.89	2.15	1.33	1.33	1.32
	Upper 95% Confidence Limit	-0.948	0.644	0.904	0.0842	0.0819	0.0767
	Lower 95% Confidence Limit	1.54	3.13	3.39	2.57	2.57	2.57
	P - Value	64.3	0.293	0.0717	3.64	3.67	3.75
240 ± 20km	Correlation Co-efficient	-1.06	1.65	1.95	1.12	1.11	1.11
	Upper 95% Confidence Limit	-2.16	0.552	0.847	0.0157	0.0123	0.00833
	Lower 95% Confidence Limit	0.0373	2.75	3.05	2.22	2.21	2.21
	P - Value	5.83	0.325	0.0526	4.68	4.75	4.83
280 ± 20km	Correlation Co-efficient	0.513	-0.139	-0.514	-0.634	-0.638	-0.637
	Upper 95% Confidence Limit	-0.580	-1.23	-1.61	-1.73	-1.73	-1.73
	Lower 95% Confidence Limit	1.61	0.956	0.581	0.46	0.458	0.458
	P - Value	35.8	80.3	35.8	25.7	25.4	25.4
320 ± 20km	Correlation Co-efficient	1.38	-1.61	-1.93	-1.74	-1.74	-1.74
	Upper 95% Confidence Limit	0.312	-2.68	-3.00	-2.81	-2.81	-2.81
	Lower 95% Confidence Limit	2.46	-0.535	-0.855	-0.663	-0.664	-0.662
	P - Value	1.14	0.332	0.0432	0.152	0.152	0.154

Storm 2, Day 4: 27th July 2004 Continued							
360 ± 20km	Correlation Co-efficient	-0.212	-1.43	-1.49	-1.39	-1.39	-1.39
	Upper 95% Confidence Limit	-1.30	-2.50	-2.57	-2.47	-2.47	-2.47
	Lower 95% Confidence Limit	0.866	-0.348	-0.411	-0.312	-0.311	-0.311
	P - Value	70.0	0.954	0.679	1.15	1.16	1.16
400 ± 20km	Correlation Co-efficient	-0.628	-1.19	-0.965	-0.763	-0.758	-0.757
	Upper 95% Confidence Limit	-1.70	-2.26	-2.04	-1.84	-1.83	-1.83
	Lower 95% Confidence Limit	0.446	-0.113	0.110	0.312	0.317	0.317
	P - Value	25.2	3.04	7.84	16.4	16.7	16.7
440 ± 20km	Correlation Co-efficient	0.680	1.97	2.50	1.88	1.88	1.87
	Upper 95% Confidence Limit	-0.64	0.645	1.17	0.556	0.550	0.546
	Lower 95% Confidence Limit	2.00	3.30	3.82	3.21	3.20	3.20
	P - Value	31.4	0.356	0.0218	0.542	0.557	0.565
480 ± 20km	Correlation Co-efficient	0.210	0.382	0.6022	1.10	1.09	1.09
	Upper 95% Confidence Limit	-0.790	-0.618	-0.399	0.101	0.0916	0.0921
	Lower 95% Confidence Limit	1.21	1.38	1.60	2.10	2.09	2.09
	P - Value	68.13	45.4	23.8	3.09	3.24	3.23

Table 8.6: Storm 2, Day 5 Results.

Storm 2, Day 5: 28th July 2004							
Assumed IPP Altitude		S_4	σ_ϕ(1s)	σ_ϕ(3s)	σ_ϕ(10s)	σ_ϕ(30s)	σ_ϕ(60s)
120 ± 20km	Correlation Co-efficient	0.0882	0.223	-0.584	-0.835	-0.842	-0.846
	Upper 95% Confidence Limit	-1.00	-0.870	-1.68	-1.93	-1.94	-1.94
	Lower 95% Confidence Limit	1.18	1.31	0.509	0.257	0.250	0.247
	P - Value	87.4	69.0	29.5	13.4	13.1	12.9
160 ± 20km	Correlation Co-efficient	0.0498	0.376	-0.689	-0.938	-0.945	-0.949
	Upper 95% Confidence Limit	-1.03	-0.708	-1.77	-2.02	-2.03	-2.03
	Lower 95% Confidence Limit	1.13	1.46	0.395	0.146	0.140	0.136
	P - Value	92.8	49.6	21.3	9.00	8.77	8.66
200 ± 20km	Correlation Co-efficient	0.763	0.0755	0.0845	-0.0132	-0.0175	-0.0184
	Upper 95% Confidence Limit	-0.323	-1.01	-1.00	-1.10	-1.11	-1.11
	Lower 95% Confidence Limit	1.85	1.16	1.17	1.07	1.07	1.07
	P - Value	16.8	89.2	87.9	98.1	97.5	97.4
240 ± 20km	Correlation Co-efficient	1.99	1.12	2.03	1.45	1.45	1.44
	Upper 95% Confidence Limit	0.931	0.0643	0.968	0.390	0.387	0.385
	Lower 95% Confidence Limit	3.04	2.18	3.09	2.51	2.50	2.50
	P - Value	0.0227	3.76	0.0177	0.733	0.746	0.764
280 ± 20km	Correlation Co-efficient	-0.0226	-0.458	-0.565	-0.476	-0.476	-0.475
	Upper 95% Confidence Limit	-1.08	-1.52	-1.63	-1.54	-1.54	-1.54
	Lower 95% Confidence Limit	1.04	0.602	0.495	0.584	0.584	0.585
	P - Value	96.7	39.7	29.6	37.9	37.9	38.0
320 ± 20km	Correlation Co-efficient	1.93	1.15	1.96	1.40	1.40	1.39
	Upper 95% Confidence Limit	0.877	0.0966	0.902	0.342	0.339	0.335
	Lower 95% Confidence Limit	2.98	2.21	3.02	2.46	2.45	2.45
	P - Value	0.0331	3.24	0.0281	0.951	0.966	0.986

Storm 2, Day 5: 28th July 2004 Continued							
360 ± 20km	Correlation Co-efficient	0.0203	0.231	-0.223	-0.418	-0.425	-0.428
	Upper 95% Confidence Limit	-1.26	-1.05	-1.50	-1.70	-1.70	-1.71
	Lower 95% Confidence Limit	1.30	1.51	1.06	0.862	0.855	0.852
	P - Value	97.5	72.3	73.2	52.2	51.5	51.2
400 ± 20km	Correlation Co-efficient	2.08	1.24	2.28	1.66	1.66	1.66
	Upper 95% Confidence Limit	0.913	0.0626	1.11	0.490	0.487	0.483
	Lower 95% Confidence Limit	3.25	2.41	3.45	2.84	2.83	2.83
	P - Value	0.0486	3.90	0.0141	0.546	0.555	0.567
440 ± 20km	Correlation Co-efficient	0.921	0.0737	0.196	0.0897	0.0895	0.0896
	Upper 95% Confidence Limit	-0.259	-1.11	-0.986	-1.09	-1.09	-1.09
	Lower 95% Confidence Limit	2.10	1.26	1.38	1.27	1.27	1.27
	P - Value	12.6	90.3	74.5	88.2	88.2	88.2
480 ± 20km	Correlation Co-efficient	-0.559	0.216	-0.769	-0.921	-0.927	-0.929
	Upper 95% Confidence Limit	-1.53	-0.753	-1.74	-1.89	-1.90	-1.90
	Lower 95% Confidence Limit	0.408	1.18	0.200	0.0488	0.0424	0.0404
	P - Value	25.7	66.3	12.0	6.27	6.09	6.03

Table 8.7: Storm 3, Day 1 Results.

Storm 3, Day 1: 8th November 2004							
Assumed IPP Altitude		S_4	σ_ϕ(1s)	σ_ϕ(3s)	σ_ϕ(10s)	σ_ϕ(30s)	σ_ϕ(60s)
120 ± 20km	Correlation Co-efficient	0.201	-0.602	-0.997	-1.03	-1.03	-1.03
	Upper 95% Confidence Limit	0.980	-1.38	-1.78	-1.81	-1.81	-1.81
	Lower 95% Confidence Limit	-0.578	0.180	-0.215	-0.247	-0.246	-0.244
	P - Value	61.3	13.1	1.25	0.994	1.00	1.01
160 ± 20km	Correlation Co-efficient	0.236	-0.794	-1.47	-1.62	-1.62	-1.62
	Upper 95% Confidence Limit	1.31	-1.87	-2.55	-2.69	-2.69	-2.69
	Lower 95% Confidence Limit	-0.834	0.279	-0.401	-0.546	-0.546	-0.545
	P - Value	66.5	14.7	0.712	0.312	0.312	0.313
200 ± 20km	Correlation Co-efficient	0.308	-0.4242	-0.465	0.0458	0.0554	0.0637
	Upper 95% Confidence Limit	1.40	-1.52	-1.56	-1.05	-1.04	-1.03
	Lower 95% Confidence Limit	-0.78	0.669	0.63	1.14	1.15	1.16
	P - Value	57.9	44.7	40.5	93.5	92.1	90.9
240 ± 20km	Correlation Co-efficient	-0.657	2.93	4.39	3.40	3.39	3.38
	Upper 95% Confidence Limit	0.410	1.86	3.33	2.33	2.32	2.31
	Lower 95% Confidence Limit	-1.72	4.00	5.46	4.47	4.46	4.45
	P - Value	22.7	$7.93\text{x}10^{-06}$	$8.50\text{x}10^{-14}$	$5.06\text{x}10^{-08}$	$5.34\text{x}10^{-08}$	$6.00\text{x}10^{-08}$
280 ± 20km	Correlation Co-efficient	0.223	2.29	3.71	2.68	2.67	2.66
	Upper 95% Confidence Limit	1.47	1.04	2.46	1.42	1.42	1.41
	Lower 95% Confidence Limit	-1.02	3.54	4.96	3.93	3.92	3.91
	P - Value	72.5	0.0334	$6.12\text{x}10^{-07}$	0.00277	0.00288	0.00304
320 ± 20km	Correlation Co-efficient	0.0232	-0.185	-0.0668	-0.0455	-0.0458	-0.0463
	Upper 95% Confidence Limit	1.09	-1.25	-1.14	-1.12	-1.12	-1.12
	Lower 95% Confidence Limit	-1.04	0.884	1.00	1.02	1.02	1.02
	P - Value	96.6	73.4	90.3	93.4	93.3	93.2

Storm 3, Day 1: 8th November 2004 Continued							
360 ± 20km	Correlation Co-efficient	-0.576	1.68	2.76	1.71	1.71	1.70
	Upper 95% Confidence Limit	0.677	0.424	1.50	0.455	0.452	0.446
	Lower 95% Confidence Limit	-1.83	2.94	4.02	2.97	2.97	2.96
	P - Value	36.8	0.877	0.00168	0.763	0.774	0.796
400 ± 20km	Correlation Co-efficient	0.569	-0.552	-0.759	-0.593	-0.590	-0.587
	Upper 95% Confidence Limit	1.76	-1.75	-1.95	-1.79	-1.79	-1.78
	Lower 95% Confidence Limit	-0.621	0.643	0.437	0.603	0.606	0.609
	P - Value	34.9	36.5	21.3	33.1	33.3	33.6
440 ± 20km	Correlation Co-efficient	0.119	-0.69	-1.57	-1.41	-1.41	-1.41
	Upper 95% Confidence Limit	1.31	-1.89	-2.77	-2.61	-2.61	-2.60
	Lower 95% Confidence Limit	-1.07	0.505	-0.374	-0.210	-0.209	-0.206
	P - Value	84.6	25.7	1.01	2.12	2.13	2.16
480 ± 20km	Correlation Co-efficient	0.806	-0.312	-0.693	-0.995	-0.995	-1.00
	Upper 95% Confidence Limit	1.77	-1.28	-1.66	-1.97	-1.97	-1.97
	Lower 95% Confidence Limit	-0.162	0.659	0.279	-0.0228	-0.0230	-0.0233
	P - Value	10.3	52.9	16.2	4.49	4.48	4.48

Table 8.8: Storm 3 Day 2 Results.

Storm 3, Day 2: 9th November 2004							
Assumed IPP Altitude		S_4	σ_ϕ(1s)	σ_ϕ(3s)	σ_ϕ(10s)	σ_ϕ(30s)	σ_ϕ(60s)
120 ± 20km	Correlation Co-efficient	0.879	-0.273	-0.241	-0.310	-0.309	-0.309
	Upper 95% Confidence Limit	0.0887	-1.06	-1.03	-1.10	-1.10	-1.10
	Lower 95% Confidence Limit	1.67	0.519	0.552	0.483	0.484	0.484
	P - Value	2.92	49.9	55.2	44.4	44.5	44.6
160 ± 20km	Correlation Co-efficient	-0.624	0.352	0.391	0.339	0.333	0.334
	Upper 95% Confidence Limit	-1.42	-0.442	-0.403	-0.456	-0.461	-0.461
	Lower 95% Confidence Limit	0.167	1.15	1.18	1.13	1.13	1.13
	P - Value	12.2	38.5	33.5	40.3	41.1	41.0
200 ± 20km	Correlation Co-efficient	-0.186	-0.0217	-0.116	-0.0698	-0.0701	-0.0684
	Upper 95% Confidence Limit	-1.41	-1.25	-1.35	-1.30	-1.30	-1.30
	Lower 95% Confidence Limit	1.04	1.21	1.11	1.16	1.16	1.16
	P - Value	76.6	97.2	85.4	91.1	91.1	91.3
240 ± 20km	Correlation Co-efficient	-1.76	1.38	0.00693	0.140	0.140	0.140
	Upper 95% Confidence Limit	-2.87	0.268	-1.11	-0.978	-0.978	-0.977
	Lower 95% Confidence Limit	-0.644	2.50	1.12	1.26	1.26	1.26
	P - Value	0.199	1.51	99.0	80.6	80.6	80.5
280 ± 20km	Correlation Co-efficient	0.534	2.34	3.27	3.69	3.67	3.67
	Upper 95% Confidence Limit	-0.777	1.03	1.96	2.38	2.36	2.36
	Lower 95% Confidence Limit	1.84	3.66	4.58	5.00	4.98	4.98
	P - Value	42.5	0.0475	0.000108	$3.74\text{x}10^{-06}$	$4.47\text{x}10^{-06}$	$4.47\text{x}10^{-06}$
320 ± 20km	Correlation Co-efficient	0.806	5.10	0.847	1.19	1.17	1.17
	Upper 95% Confidence Limit	-0.276	4.02	-0.238	0.102	0.0868	0.0874
	Lower 95% Confidence Limit	1.89	6.18	1.93	2.27	2.26	2.26
	P - Value	14.4	$2.68\text{x}10^{-18}$	12.6	3.20	3.429	3.42

Storm 3, Day 2: 9th November 2004 Continued							
360 ± 20km	Correlation Co-efficient	-0.0333	2.43	0.280	0.531	0.526	0.527
	Upper 95% Confidence Limit	-1.12	1.34	-0.810	-0.560	-0.564	-0.563
	Lower 95% Confidence Limit	1.054	3.52	1.37	1.62	1.62	1.62
	P - Value	95.21	0.00125	61.4	34.0	34.4	34.3
400 ± 20km	Correlation Co-efficient	0.682	6.91	0.840	1.11	1.10	1.11
	Upper 95% Confidence Limit	-0.530	5.70	-0.375	-0.107	-0.113	-0.111
	Lower 95% Confidence Limit	1.89	8.11	2.06	2.33	2.32	2.32
	P - Value	27.0	6.67×10^{-27}	17.6	7.40	7.54	7.49
440 ± 20km	Correlation Co-efficient	1.17	1.46	0.469	1.16	1.14	1.15
	Upper 95% Confidence Limit	-0.0794	0.213	-0.783	-0.0960	-0.108	-0.104
	Lower 95% Confidence Limit	2.42	2.71	1.72	2.41	2.40	2.40
	P - Value	6.65	2.18	46.2	7.03	7.33	7.23
480 ± 20km	Correlation Co-efficient	1.40	-0.158	-0.403	-0.492	-0.496	-0.497
	Upper 95% Confidence Limit	0.416	-1.15	-1.39	-1.48	-1.49	-1.49
	Lower 95% Confidence Limit	2.39	0.832	0.588	0.500	0.495	0.495
	P - Value	0.536	75.4	42.5	33.1	32.7	32.6

Table 8.9: Storm 3, Day 3 Results.

Storm 3, Day 3: 10th November 2004							
Assumed IPP Altitude		S_4	σ_ϕ(1s)	σ_ϕ(3s)	σ_ϕ(10s)	σ_ϕ(30s)	σ_ϕ(60s)
120 ± 20km	Correlation Co-efficient	1.27	-0.264	-0.268	0.332	0.350	0.359
	Upper 95% Confidence Limit	0.154	-1.38	-1.38	-0.784	-0.766	-0.757
	Lower 95% Confidence Limit	2.36	0.849	0.847	1.45	1.46	1.47
	P - Value	2.56	64.2	63.8	56.0	53.9	52.9
160 ± 20km	Correlation Co-efficient	-1.33	-0.616	-0.605	-0.600	-0.600	-0.597
	Upper 95% Confidence Limit	-2.44	-1.72	-1.71	-1.71	-1.71	-1.71
	Lower 95% Confidence Limit	-0.225	0.492	0.505	0.511	0.511	0.513
	P - Value	1.83	27.6	28.5	29.0	29.0	29.2
200 ± 20km	Correlation Co-efficient	0.0442	0.209	0.289	0.901	0.893	0.890
	Upper 95% Confidence Limit	-1.09	-0.931	-0.851	-0.240	-0.248	-0.252
	Lower 95% Confidence Limit	1.18	1.35	1.43	2.04	2.03	2.03
	P - Value	93.9	72.0	61.9	12.2	12.5	12.7
240 ± 20km	Correlation Co-efficient	-1.10	1.38	1.66	3.10	3.09	3.08
	Upper 95% Confidence Limit	-2.22	0.253	0.540	1.98	1.96	1.95
	Lower 95% Confidence Limit	0.0253	2.50	2.79	4.23	4.21	4.20
	P - Value	5.54	1.63	0.372	6.71×10^{-06}	7.91×10^{-06}	8.64×10^{-06}
280 ± 20km	Correlation Co-efficient	2.56	-0.514	-0.302	0.247	0.271	0.286
	Upper 95% Confidence Limit	1.27	-1.80	-1.59	-1.04	-1.02	-1.00
	Lower 95% Confidence Limit	3.84	0.772	0.986	1.54	1.56	1.57
	P - Value	0.00951	43.3	64.6	70.7	68.0	66.4
320 ± 20km	Correlation Co-efficient	2.62	-0.0592	-0.350	0.273	0.302	0.317
	Upper 95% Confidence Limit	1.57	-1.11	-1.41	-0.783	-0.755	-0.739
	Lower 95% Confidence Limit	3.68	0.995	0.706	1.33	1.36	1.37
	P - Value	0.000101	91.2	51.6	61.2	57.6	55.6

Storm 3, Day 3: 10th November 2004 Continued							
360 ± 20km	Correlation Co-efficient	0.609	-0.509	-0.461	-0.511	0.302	-0.514
	Upper 95% Confidence Limit	-0.476	-1.60	-1.55	-1.60	-0.755	-1.60
	Lower 95% Confidence Limit	1.69	0.579	0.628	0.578	1.36	0.576
	P - Value	27.1	35.9	40.7	35.8	57.6	35.6
400 ± 20km	Correlation Co-efficient	1.03	-0.472	-0.805	-0.440	-0.434	-0.431
	Upper 95% Confidence Limit	-0.0675	-1.58	-1.91	-1.55	-1.54	-1.54
	Lower 95% Confidence Limit	2.13	0.631	0.299	0.665	0.672	0.674
	P - Value	6.58	40.2	15.3	43.5	44.2	44.5
440 ± 20km	Correlation Co-efficient	-0.0404	0.00707	0.148	0.0656	0.0836	0.0931
	Upper 95% Confidence Limit	-1.14	-1.10	-0.958	-1.04	-1.02	-1.01
	Lower 95% Confidence Limit	1.06	1.11	1.25	1.17	1.19	1.20
	P - Value	94.3	99.0	79.3	90.8	88.2	86.9
480 ± 20km	Correlation Co-efficient	-1.21	-0.723	-0.634	-0.628	-0.627	-0.626
	Upper 95% Confidence Limit	-2.23	-1.75	-1.66	-1.66	-1.65	-1.65
	Lower 95% Confidence Limit	-0.186	0.303	0.392	0.40	0.401	0.402
	P - Value	2.05	16.7	22.6	23.1	23.2	23.3

Table 8.10: Storm 3, Day 4 Results.

Storm 3, Day 4: 11th November 2004							
Assumed IPP Altitude		S_4	σ_ϕ(1s)	σ_ϕ(3s)	σ_ϕ(10s)	σ_ϕ(30s)	σ_ϕ(60s)
120 ± 20km	Correlation Co-efficient	-1.81	-0.762	-0.720	-0.750	-0.743	-0.740
	Upper 95% Confidence Limit	-2.88	-1.83	-1.79	-1.82	-1.810	-1.81
	Lower 95% Confidence Limit	-0.749	0.304	0.346	0.317	0.323	0.327
	P - Value	0.0839	16.1	18.5	16.8	17.2	17.4
160 ± 20km	Correlation Co-efficient	-0.488	-0.990	-1.06	-1.11	-1.10	-1.10
	Upper 95% Confidence Limit	-1.56	-2.06	-2.13	-2.18	-2.18	-2.17
	Lower 95% Confidence Limit	0.586	0.0845	0.0187	-0.0320	-0.0254	-0.0210
	P - Value	37.3	7.09	5.41	4.36	4.48	4.57
200 ± 20km	Correlation Co-efficient	-2.20	-0.924	-0.741	-0.744	-0.737	-0.734
	Upper 95% Confidence Limit	-3.37	-2.10	-1.92	-1.92	-1.91	-1.91
	Lower 95% Confidence Limit	-1.02	0.250	0.434	0.431	0.438	0.442
	P - Value	0.0240	12.3	21.6	21.4	21.9	22.1
240 ± 20km	Correlation Co-efficient	-1.73	-0.702	-0.576	-0.580	-0.574	-0.572
	Upper 95% Confidence Limit	-2.79	-1.76	-1.64	-1.64	-1.63	-1.63
	Lower 95% Confidence Limit	-0.673	0.357	0.483	0.480	0.486	0.489
	P - Value	0.134	19.4	28.6	28.4	28.8	29.1
280 ± 20km	Correlation Co-efficient	-1.26	-0.703	-0.291	-0.508	-0.508	-0.508
	Upper 95% Confidence Limit	-2.36	-1.81	-1.39	-1.61	-1.61	-1.61
	Lower 95% Confidence Limit	-0.157	0.401	0.814	0.597	0.597	0.597
	P - Value	2.51	21.2	60.6	36.7	36.7	36.7
320 ± 20km	Correlation Co-efficient	0.725	-0.122	-0.271	-0.303	-0.302	-0.300
	Upper 95% Confidence Limit	-0.301	-1.15	-1.30	-1.33	-1.33	-1.33
	Lower 95% Confidence Limit	1.75	0.906	0.758	0.726	0.727	0.728
	P - Value	16.6	81.6	60.6	56.4	56.5	56.7

Storm 3, Day 4: 11th November Continued							
360 ± 20km	Correlation Co-efficient	0.618	0.561	-0.474	-0.605	-0.606	-0.605
	Upper 95% Confidence Limit	-0.444	-0.501	-1.54	-1.67	-1.67	-1.67
	Lower 95% Confidence Limit	1.68	1.62	0.589	0.459	0.458	0.459
	P - Value	25.4	30.1	38.2	26.5	26.5	26.5
400 ± 20km	Correlation Co-efficient	0.0929	-0.120	-0.458	-0.599	-0.601	-0.603
	Upper 95% Confidence Limit	-0.989	-1.20	-1.54	-1.68	-1.69	-1.69
	Lower 95% Confidence Limit	1.18	0.963	0.626	0.485	0.483	0.482
	P - Value	86.6	82.8	40.8	27.9	27.7	27.6
440 ± 20km	Correlation Co-efficient	-0.309	-0.524	-0.532	-0.652	-0.651	-0.650
	Upper 95% Confidence Limit	-1.39	-1.608	-1.62	-1.74	-1.74	-1.74
	Lower 95% Confidence Limit	0.774	0.561	0.553	0.433	0.434	0.436
	P - Value	57.6	34.4	33.6	23.9	24.0	24.1
480 ± 20km	Correlation Co-efficient	-0.0139	0.198	0.591	0.198	0.199	0.200
	Upper 95% Confidence Limit	-1.04	-0.824	-0.431	-0.825	-0.824	-0.824
	Lower 95% Confidence Limit	1.01	1.22	1.61	1.22	1.22	1.22
	P - Value	97.9	70.4	25.7	70.4	70.3	70.2

Table 8.11: Storm 4, Day 1 Results.

Storm 4, Day 1: 14th May 2005							
Assumed IPP Altitude		S_4	σ_ϕ(1s)	σ_ϕ(3s)	σ_ϕ(10s)	σ_ϕ(30s)	σ_ϕ(60s)
120 ± 20km	Correlation Co-efficient	10.0	No data	No data	8.12	8.13	No data
	Upper 95% Confidence Limit	-4.86	No data	No data	-6.75	-6.74	No data
	Lower 95% Confidence Limit	24.4	No data	No data	22.6	22.7	No data
	P - Value	18.6	No data	No data	28.4	28.3	No data
160 ± 20km	Correlation Co-efficient	5.89	No data	No data	4.45	4.44	No data
	Upper 95% Confidence Limit	-9.24	No data	No data	-10.7	-10.7	No data
	Lower 95% Confidence Limit	20.8	No data	No data	19.4	19.4	No data
	P - Value	44.5	No data	No data	56.5	56.5	No data
200 ± 20km	Correlation Co-efficient	-0.530	No data	No data	-2.56	-2.57	No data
	Upper 95% Confidence Limit	-18.0	No data	No data	-20.0	-20.0	No data
	Lower 95% Confidence Limit	17.0	No data	No data	15.0	15.0	No data
	P - Value	95.3	No data	No data	77.6	77.5	No data
240 ± 20km	Correlation Co-efficient	7.40	No data	No data	6.03	6.05	No data
	Upper 95% Confidence Limit	-10.4	No data	No data	-11.7	-11.7	No data
	Lower 95% Confidence Limit	24.7	No data	No data	23.4	23.4	No data
	P - Value	41.4	No data	No data	50.6	50.5	No data
280 ± 20km	Correlation Co-efficient	7.40	No data	No data	6.03	6.05	No data
	Upper 95% Confidence Limit	-10.4	No data	No data	-11.7	-11.7	No data
	Lower 95% Confidence Limit	24.7	No data	No data	23.4	23.4	No data
	P - Value	41.4	No data	No data	50.6	50.5	No data
320 ± 20km	Correlation Co-efficient	7.59	No data	No data	5.99	6.01	No data
	Upper 95% Confidence Limit	-10.6	No data	No data	-12.2	-12.2	No data
	Lower 95% Confidence Limit	25.3	No data	No data	23.8	23.8	No data
	P - Value	41.4	No data	No data	51.9	51.8	No data

Storm 4, Day 1: 14th May 2005 Continued							
360 ± 20km	Correlation Co-efficient	6.70	No data	No data	4.94	4.95	No data
	Upper 95% Confidence Limit	-12.7	No data	No data	-14.5	-14.4	No data
	Lower 95% Confidence Limit	25.6	No data	No data	24.0	24.0	No data
	P - Value	49.9	No data	No data	61.9	61.8	No data
400 ± 20km	Correlation Co-efficient	10.9	No data	No data	7.63	7.65	No data
	Upper 95% Confidence Limit	-9.10	No data	No data	-12.4	-12.4	No data
	Lower 95% Confidence Limit	30.1	No data	No data	27.0	27.1	No data
	P - Value	28.4	No data	No data	45.5	45.4	No data
440 ± 20km	Correlation Co-efficient	12.9	No data	No data	9.23	9.26	No data
	Upper 95% Confidence Limit	-7.16	No data	No data	-10.8	-10.8	No data
	Lower 95% Confidence Limit	31.9	No data	No data	28.5	28.6	No data
	P - Value	20.7	No data	No data	36.6	36.5	No data
480 ± 20km	Correlation Co-efficient	3.58	No data	No data	9.23	1.33	No data
	Upper 95% Confidence Limit	-16.4	No data	No data	-10.8	-18.6	No data
	Lower 95% Confidence Limit	23.3	No data	No data	28.5	21.1	No data
	P - Value	72.6	No data	No data	36.6	89.6	No data

Table 8.12: Storm 4, Day 2 Results.

Storm 4, Day 2: 15th May 2005							
Assumed IPP Altitude		S_4	σ_ϕ(1s)	σ_ϕ(3s)	σ_ϕ(10s)	σ_ϕ(30s)	σ_ϕ(60s)
120 ± 20km	Correlation Co-efficient	6.61	No data	No data	7.12	7.13	No data
	Upper 95% Confidence Limit	-1.22	No data	No data	-0.703	-0.694	No data
	Lower 95% Confidence Limit	14.4	No data	No data	14.9	14.9	No data
	P - Value	9.81	No data	No data	7.44	7.40	No data
160 ± 20km	Correlation Co-efficient	-3.33	No data	No data	-3.61	-3.61	No data
	Upper 95% Confidence Limit	-11.0	No data	No data	-11.3	-11.3	No data
	Lower 95% Confidence Limit	4.39	No data	No data	4.11	4.10	No data
	P - Value	39.7	No data	No data	35.9	35.9	No data
200 ± 20km	Correlation Co-efficient	2.37	No data	No data	2.50	2.50	No data
	Upper 95% Confidence Limit	-5.25	No data	No data	-5.12	-5.12	No data
	Lower 95% Confidence Limit	9.97	No data	No data	10.1	10.1	No data
	P - Value	54.2	No data	No data	52.1	52.0	No data
240 ± 20km	Correlation Co-efficient	-3.38	No data	No data	-3.73	-3.73	No data
	Upper 95% Confidence Limit	-11.3	No data	No data	-11.6	-11.6	No data
	Lower 95% Confidence Limit	4.54	No data	No data	4.19	4.19	No data
	P - Value	40.3	No data	No data	35.6	35.6	No data
280 ± 20km	Correlation Co-efficient	7.89	No data	No data	8.34	8.35	No data
	Upper 95% Confidence Limit	-0.0309	No data	No data	0.416	0.424	No data
	Lower 95% Confidence Limit	15.7	No data	No data	16.2	16.2	No data
	P - Value	5.09	No data	No data	3.92	3.90	No data
320 ± 20km	Correlation Co-efficient	2.621	-0.0592	-0.350	0.273	0.302	0.317
	Upper 95% Confidence Limit	1.57	-1.11	-1.41	-0.783	-0.755	-0.739
	Lower 95% Confidence Limit	3.68	0.995	0.706	1.33	1.36	1.37
	P - Value	0.000101	91.2	51.6	61.2	57.6	55.6

Storm 4, Day 2: 15th May 2005 Continued							
360 ± 20km	Correlation Co-efficient	-3.40	No data	No data	-3.83	-3.83	No data
	Upper 95% Confidence Limit	-11.4	No data	No data	-11.8	-11.8	No data
	Lower 95% Confidence Limit	4.62	No data	No data	4.19	4.19	No data
	P - Value	40.6	No data	No data	34.9	34.9	No data
400 ± 20km	Correlation Co-efficient	23.1	No data	No data	23.8	23.8	No data
	Upper 95% Confidence Limit	15.7	No data	No data	16.4	16.5	No data
	Lower 95% Confidence Limit	30.2	No data	No data	30.9	31.0	No data
	P - Value	$2.54x10^{-07}$	No data	No data	$7.53x10^{-08}$	$7.29x10^{-08}$	No data
440 ± 20km	Correlation Co-efficient	18.7	No data	No data	19.3	19.3	No data
	Upper 95% Confidence Limit	10.8	No data	No data	11.3	11.3	No data
	Lower 95% Confidence Limit	26.4	No data	No data	26.9	27.0	No data
	P - Value	0.000528	No data	No data	0.000276	0.000271	No data
480 ± 20km	Correlation Co-efficient	-1.21	-0.723	-0.634	-0.628	-0.627	-0.626
	Upper 95% Confidence Limit	-2.23	-1.75	-1.66	-1.66	-1.65	-1.65
	Lower 95% Confidence Limit	-0.1863	0.303	0.392	0.400	0.401	0.402
	P - Value	2.055	16.7	22.6	23.1	23.2	23.3

Table 8.13: Storm 4, Day 3 Results.

Storm 4, Day 3: 16th May 2005							
Assumed IPP Altitude		S_4	σ_ϕ(1s)	σ_ϕ(3s)	σ_ϕ(10s)	σ_ϕ(30s)	σ_ϕ(60s)
120 ± 20km	Correlation Co-efficient	-0.112	No data	No data	-0.420	-0.420	No data
	Upper 95% Confidence Limit	-2.01	No data	No data	-2.31	-2.31	No data
	Lower 95% Confidence Limit	1.78	No data	No data	1.47	1.47	No data
	P - Value	90.8	No data	No data	66.4	66.4	No data
160 ± 20km	Correlation Co-efficient	-0.896	No data	No data	-0.871	-0.871	No data
	Upper 95% Confidence Limit	-2.80	No data	No data	-2.78	-2.78	No data
	Lower 95% Confidence Limit	1.01	No data	No data	1.03	1.03	No data
	P - Value	35.7	No data	No data	37.0	37.0	No data
200 ± 20km	Correlation Co-efficient	0.313	No data	No data	0.872	0.871	No data
	Upper 95% Confidence Limit	-1.70	No data	No data	-1.14	-1.14	No data
	Lower 95% Confidence Limit	2.32	No data	No data	2.88	2.88	No data
	P - Value	76.0	No data	No data	39.5	39.6	No data
240 ± 20km	Correlation Co-efficient	-0.601	No data	No data	-0.646	-0.646	No data
	Upper 95% Confidence Limit	-3.20	No data	No data	-3.25	-3.25	No data
	Lower 95% Confidence Limit	2.00	No data	No data	1.96	1.96	No data
	P - Value	65.1	No data	No data	62.7	62.7	No data
280 ± 20km	Correlation Co-efficient	0.787	No data	No data	1.91	1.91	No data
	Upper 95% Confidence Limit	-2.24	No data	No data	-1.12	-1.12	No data
	Lower 95% Confidence Limit	3.81	No data	No data	4.93	4.93	No data
	P - Value	61.0	No data	No data	21.6	21.7	No data
320 ± 20km	Correlation Co-efficient	3.14	No data	No data	3.01	3.00	No data
	Upper 95% Confidence Limit	0.702	No data	No data	0.569	0.567	No data
	Lower 95% Confidence Limit	5.57	No data	No data	5.44	5.44	No data
	P - Value	1.16	No data	No data	1.56	1.57	No data

Storm 4, Day 3: 16th May 2005 Continued							
360 ± 20km	Correlation Co-efficient	3.21	No data	No data	4.12	4.12	No data
	Upper 95% Confidence Limit	0.135	No data	No data	1.05	1.05	No data
	Lower 95% Confidence Limit	6.27	No data	No data	7.18	7.18	No data
	P - Value	4.07	No data	No data	0.856	0.846	No data
400 ± 20km	Correlation Co-efficient	3.45	No data	No data	4.31	4.32	No data
	Upper 95% Confidence Limit	0.575	No data	No data	1.43	1.44	No data
	Lower 95% Confidence Limit	6.33	No data	No data	7.18	7.19	No data
	P - Value	1.87	No data	No data	0.333	0.329	No data
440 ± 20km	Correlation Co-efficient	1.74	No data	No data	2.69	2.69	No data
	Upper 95% Confidence Limit	-1.26	No data	No data	-0.311	-0.306	No data
	Lower 95% Confidence Limit	4.74	No data	No data	5.68	5.69	No data
	P - Value	25.5	No data	No data	7.90	7.84	No data
480 ± 20km	Correlation Co-efficient	1.54	No data	No data	1.83	1.83	No data
	Upper 95% Confidence Limit	-0.935	No data	No data	-0.647	-0.644	No data
	Lower 95% Confidence Limit	4.01	No data	No data	4.30	4.30	No data
	P - Value	22.3	No data	No data	14.8	14.7	No data

Appendix 3: Correlation of Mean Turbulent Wave Amplitude with Scintillation Indices: Full Results

The full results for all days analysed are tabulated in the subsequent pages of this appendix.

Table 9.1: Storm 1, Day 1 Results.

Storm 1, Day 1: 30th Oct 2003							
Assumed IPP Altitude		S_4	σ_ϕ(1s)	σ_ϕ(3s)	σ_ϕ(10s)	σ_ϕ(30s)	σ_ϕ(60s)
120 ± 20km	Correlation Co-efficient	-7.77	No data	No data	5.65	5.65	No data
	Upper 95% Confidence Limit	-13.3	No data	No data	0.750	0.746	No data
	Lower 95% Confidence Limit	-2.23	No data	No data	10.5	10.5	No data
	P - Value	0.606	No data	No data	2.39	2.40	No data
160 ± 20km	Correlation Co-efficient	-7.99	No data	No data	10.5	10.5	No data
	Upper 95% Confidence Limit	-13.5	No data	No data	5.64	5.64	No data
	Lower 95% Confidence Limit	-2.43	No data	No data	15.4	15.4	No data
	P - Value	0.490	No data	No data	0.00268	0.00270	No data
200 ± 20km	Correlation Co-efficient	-3.24	No data	No data	10.8	10.8	No data
	Upper 95% Confidence Limit	-8.78	No data	No data	5.81	5.82	No data
	Lower 95% Confidence Limit	2.32	No data	No data	15.8	15.8	No data
	P - Value	25.4	No data	No data	0.00253	0.00250	No data
240 ± 20km	Correlation Co-efficient	-4.32	No data	No data	-1.87	-1.87	No data
	Upper 95% Confidence Limit	-9.80	No data	No data	-6.98	-6.98	No data
	Lower 95% Confidence Limit	1.18	No data	No data	3.26	3.25	No data
	P - Value	12.4	No data	No data	47.5	47.5	No data
280 ± 20km	Correlation Co-efficient	4.04	No data	No data	1.53	1.53	No data
	Upper 95% Confidence Limit	-1.51	No data	No data	-3.72	-3.71	No data
	Lower 95% Confidence Limit	9.56	No data	No data	6.77	6.77	No data
	P - Value	15.3	No data	No data	56.8	56.7	No data
320 ± 20km	Correlation Co-efficient	3.69	No data	No data	3.96	3.97	No data
	Upper 95% Confidence Limit	-1.77	No data	No data	-1.32	-1.31	No data
	Lower 95% Confidence Limit	9.12	No data	No data	9.22	9.22	No data
	P - Value	18.6	No data	No data	14.1	14.1	No data

Storm 1, Day 1: 30th Oct 2003 Continued							
360 ± 20km	Correlation Co-efficient	2.43	No data	No data	1.58	1.58	No data
	Upper 95% Confidence Limit	-3.04	No data	No data	-3.69	-3.69	No data
	Lower 95% Confidence Limit	7.88	No data	No data	6.85	6.85	No data
	P - Value	38.4	No data	No data	55.6	55.7	No data
400 ± 20km	Correlation Co-efficient	-1.04	No data	No data	12.5	12.5	No data
	Upper 95% Confidence Limit	-6.49	No data	No data	7.31	7.31	No data
	Lower 95% Confidence Limit	4.41	No data	No data	17.7	17.7	No data
	P - Value	70.8	No data	No data	0.000295	0.000297	No data
440 ± 20km	Correlation Co-efficient	-3.26	No data	No data	2.91	2.91	No data
	Upper 95% Confidence Limit	-8.66	No data	No data	-2.39	-2.40	No data
	Lower 95% Confidence Limit	2.17	No data	No data	8.20	8.19	No data
	P - Value	23.9	No data	No data	28.2	28.3	No data
480 ± 20km	Correlation Co-efficient	-6.21	No data	No data	0.744	0.740	No data
	Upper 95% Confidence Limit	-11.6	No data	No data	-4.53	-4.53	No data
	Lower 95% Confidence Limit	-0.788	No data	No data	6.01	6.00	No data
	P - Value	2.49	No data	No data	78.2	78.3	No data

Table 9.2: Storm 2, Day 2 Results.

Storm 2, Day 1: 24th July 2004							
Assumed IPP Altitude		S_4	σ_ϕ(1s)	σ_ϕ(3s)	σ_ϕ(10s)	σ_ϕ(30s)	σ_ϕ(60s)
120 ± 20km	Correlation Co-efficient	-0.751	-0.00985	-0.657	-0.641	-0.639	0.387
	Upper 95% Confidence Limit	-1.57	-0.828	-1.45	-1.43	-1.43	-0.431
	Lower 95% Confidence Limit	0.0650	0.808	0.135	0.151	0.152	1.21
	P - Value	7.13	98.1	10.4	11.3	11.3	35.4
160 ± 20km	Correlation Co-efficient	-0.904	-0.0562	-0.509	-0.421	-0.419	0.523
	Upper 95% Confidence Limit	-1.72	-0.872	-1.64	-1.55	-1.55	-0.294
	Lower 95% Confidence Limit	-0.0904	0.760	0.618	0.706	0.708	1.34
	P - Value	2.94	89.3	37.6	46.4	46.6	20.9
200 ± 20km	Correlation Co-efficient	0.420	1.74	-0.587	-0.559	-0.558	0.415
	Upper 95% Confidence Limit	-0.394	0.920	-1.82	-1.80	-1.79	-0.401
	Lower 95% Confidence Limit	1.23	2.55	0.650	0.678	0.680	1.23
	P - Value	31.1	0.00306	35.2	37.6	37.7	31.9
240 ± 20km	Correlation Co-efficient	0.931	1.48	0.182	0.0984	0.0976	0.333
	Upper 95% Confidence Limit	0.116	0.667	-0.909	-0.992	-0.993	-0.483
	Lower 95% Confidence Limit	1.75	2.30	1.27	1.19	1.19	1.15
	P - Value	2.51	0.0368	74.4	86.0	86.1	42.4
280 ± 20km	Correlation Co-efficient	2.35	0.977	-0.498	-0.539	-0.539	0.981
	Upper 95% Confidence Limit	1.53	0.157	-1.59	-1.63	-1.63	0.161
	Lower 95% Confidence Limit	3.16	1.80	0.591	0.549	0.550	1.80
	P - Value	1.86×10^{-06}	1.95	37.0	33.2	33.2	1.90
320 ± 20km	Correlation Co-efficient	-0.852	-0.00985	-0.0238	-0.119	-0.118	-1.69
	Upper 95% Confidence Limit	-1.95	-0.828	-1.11	-1.20	-1.20	-2.80
	Lower 95% Confidence Limit	0.249	0.808	1.06	0.962	0.964	-0.587
	P - Value	12.9	98.1	96.6	82.9	83.0	0.270

Storm 2, Day 1: 24th July 2004 Continued							
360 ± 20km	Correlation Co-efficient	0.638	2.67	-0.289	-0.336	-0.336	2.04
	Upper 95% Confidence Limit	-0.458	1.57	-1.37	-1.42	-1.42	0.938
	Lower 95% Confidence Limit	1.73	3.78	0.796	0.748	0.749	3.13
	P - Value	25.4	0.000213	60.2	54.3	54.4	0.0280
400 ± 20km	Correlation Co-efficient	0.101	1.76	-0.302	-0.332	-0.331	0.905
	Upper 95% Confidence Limit	-0.996	0.658	-1.39	-1.42	-1.41	-0.194
	Lower 95% Confidence Limit	1.20	2.85	0.781	0.751	0.752	2.00
	P - Value	85.7	0.172	58.4	54.8	54.9	10.7
440 ± 20km	Correlation Co-efficient	0.0439	0.498	-0.222	-0.0487	-0.0447	-0.164
	Upper 95% Confidence Limit	-1.06	-0.601	-1.56	-1.39	-1.39	-1.27
	Lower 95% Confidence Limit	1.14	1.60	1.12	1.29	1.30	0.939
	P - Value	93.8	37.4	74.5	94.3	94.8	77.1
480 ± 20km	Correlation Co-efficient	-0.982	-0.218	-0.172	-0.268	-0.271	-0.234
	Upper 95% Confidence Limit	-1.99	-1.324	-1.17	-1.27	-1.27	-1.25
	Lower 95% Confidence Limit	0.0279	0.884	0.828	0.732	0.729	0.778
	P - Value	5.67	69.8	73.6	59.9	59.6	65.1

Table 9.3: Storm 2, Day 2 Results.

Storm 2, Day 2: 25th July 2004							
Assumed IPP Altitude		S_4	σ_ϕ(1s)	σ_ϕ(3s)	σ_ϕ(10s)	σ_ϕ(30s)	σ_ϕ(60s)
120 ± 20km	Correlation Co-efficient	0.188	-0.686	-0.860	-1.05	-1.05	-1.153
	Upper 95% Confidence Limit	-0.495	-1.51	-1.68	-1.87	-1.87	-1.84
	Lower 95% Confidence Limit	0.872	0.135	-0.0385	-0.223	-0.223	-0.467
	P - Value	58.9	10.2	4.02	1.27	1.27	0.0983
160 ± 20km	Correlation Co-efficient	0.245	-0.186	-0.234	-0.219	-0.218	-1.16
	Upper 95% Confidence Limit	-0.440	-1.01	-1.06	-1.05	-1.04	-1.84
	Lower 95% Confidence Limit	0.930	0.639	0.591	0.607	0.608	-0.470
	P - Value	48.3	65.8	57.8	60.4	60.5	0.0967
200 ± 20km	Correlation Co-efficient	0.496	0.297	0.346	1.00	1.00	-0.243
	Upper 95% Confidence Limit	-0.186	-1.01	-0.960	-0.307	-0.307	-0.928
	Lower 95% Confidence Limit	1.18	1.60	1.65	2.31	2.31	0.441
	P - Value	15.4	65.6	60.4	13.4	13.4	48.6
240 ± 20km	Correlation Co-efficient	0.518	0.785	0.753	1.00	0.991	-0.00310
	Upper 95% Confidence Limit	-0.167	-0.370	-0.402	-0.154	-0.165	-0.690
	Lower 95% Confidence Limit	1.20	1.94	1.91	2.16	2.15	0.683
	P - Value	13.8	18.3	20.1	8.95	9.29	99.3
280 ± 20km	Correlation Co-efficient	0.544	-0.0511	-0.316	-0.901	-0.910	0.348
	Upper 95% Confidence Limit	-0.143	-1.44	-1.70	-2.29	-2.30	-0.341
	Lower 95% Confidence Limit	1.23	1.34	1.07	0.490	0.481	1.04
	P - Value	12.1	94.2	65.5	20.4	20.0	32.2
320 ± 20km	Correlation Co-efficient	0.649	-0.628	-0.595	-0.722	-0.726	0.489
	Upper 95% Confidence Limit	-0.0370	-1.76	-1.73	-1.85	-1.86	-0.198
	Lower 95% Confidence Limit	1.33	0.503	0.535	0.409	0.405	1.18
	P - Value	6.37	27.6	30.2	21.1	20.8	16.3

Storm 2, Day 2: 25th July 2004 Continued							
360 ± 20km	Correlation Co-efficient	0.612	-1.08	-1.02	-2.40	-2.40	0.611
	Upper 95% Confidence Limit	-0.0727	-2.47	-2.42	-3.79	-3.80	-0.0763
	Lower 95% Confidence Limit	1.30	0.320	0.372	-1.00	-1.01	1.30
	P - Value	7.98	13.1	15.1	0.0768	0.0753	8.15
400 ± 20km	Correlation Co-efficient	0.571	-1.29	-1.22	-2.48	-2.48	0.324
	Upper 95% Confidence Limit	-0.117	-2.59	-2.51	-3.78	-3.77	-0.366
	Lower 95% Confidence Limit	1.26	0.000782	0.0750	-1.19	-1.19	1.01
	P - Value	10.4	5.01	6.48	0.0170	0.0173	35.8
440 ± 20km	Correlation Co-efficient	0.594	0.00707	0.148	0.0656	0.0836	0.331
	Upper 95% Confidence Limit	-0.0949	-1.10	-0.958	-1.04	-1.02	-0.361
	Lower 95% Confidence Limit	1.28	1.11	1.25	1.17	1.19	1.02
	P - Value	9.10	99.0	79.3	90.8	88.2	34.8
480 ± 20km	Correlation Co-efficient	0.470	-0.723	-0.634	-0.628	-0.627	0.351
	Upper 95% Confidence Limit	-0.214	-1.75	-1.66	-1.66	-1.65	-0.333
	Lower 95% Confidence Limit	1.15	0.303	0.392	0.400	0.401	1.04
	P - Value	17.8	16.7	22.6	23.1	23.2	31.4

Table 9.4: Storm 2 Day 3 Results.

Storm 2, Day 3: 26th July 2004							
Assumed IPP Altitude		S_4	σ_ϕ(1s)	σ_ϕ(3s)	σ_ϕ(10s)	σ_ϕ(30s)	σ_ϕ(60s)
120 ± 20km	Correlation Co-efficient	-0.480	-0.237	-0.290	-0.404	-0.403	0.587
	Upper 95% Confidence Limit	-1.16	-1.01	-1.07	-1.18	-1.18	-0.100
	Lower 95% Confidence Limit	0.206	0.538	0.484	0.372	0.373	1.27
	P - Value	17.0	54.9	46.3	30.8	30.9	9.42
160 ± 20km	Correlation Co-efficient	-0.457	-0.185	-0.319	-0.416	-0.417	0.446
	Upper 95% Confidence Limit	-1.14	-1.29	-1.43	-1.53	-1.53	-0.243
	Lower 95% Confidence Limit	0.229	0.924	0.790	0.694	0.694	1.13
	P - Value	19.2	74.3	57.3	46.3	46.2	20.4
200 ± 20km	Correlation Co-efficient	-0.465	-0.364	-0.392	-0.00784	-0.00881	0.399
	Upper 95% Confidence Limit	-1.15	-1.46	-1.49	-1.10	-1.11	-0.286
	Lower 95% Confidence Limit	0.218	0.730	0.703	1.09	1.09	1.08
	P - Value	18.2	51.4	48.3	98.9	98.7	25.3
240 ± 20km	Correlation Co-efficient	2.25	-0.391	-0.317	-0.670	-0.670	-1.93
	Upper 95% Confidence Limit	1.29	-1.48	-1.40	-1.76	-1.76	-2.89
	Lower 95% Confidence Limit	3.21	0.694	0.767	0.417	0.417	-0.965
	P - Value	0.000442	48.0	56.5	22.7	22.7	0.00880
280 ± 20km	Correlation Co-efficient	1.37	0.00885	0.197	0.143	0.136	-0.702
	Upper 95% Confidence Limit	0.421	-1.07	-0.885	-0.939	-0.946	-1.65
	Lower 95% Confidence Limit	2.32	1.09	1.29	1.23	1.22	0.250
	P - Value	0.466	98.7	72.2	79.6	80.5	14.9
320 ± 20km	Correlation Co-efficient	2.00	-1.34	-1.51	-2.09	-2.08	1.64
	Upper 95% Confidence Limit	1.06	-2.41	-2.58	-3.16	-3.15	0.710
	Lower 95% Confidence Limit	2.92	-0.278	-0.446	-1.03	-1.02	2.57
	P - Value	0.00252	1.35	0.545	0.0119	0.0127	0.0543

Storm 2, Day 3: 26th July 2004 Continued							
360 ± 20km	Correlation Co-efficient	0.125	-0.742	-0.620	0.0347	0.0311	-1.62
	Upper 95% Confidence Limit	-0.806	-1.82	-1.69	-1.04	-1.04	-2.55
	Lower 95% Confidence Limit	1.06	0.331	0.453	1.11	1.11	-0.684
	P - Value	79.2	17.5	25.7	95.0	95.5	0.0685
400 ± 20km	Correlation Co-efficient	0.365	-1.23	-0.999	-0.928	-0.923	-0.328
	Upper 95% Confidence Limit	-0.554	-2.31	-2.08	-2.01	-2.01	-1.25
	Lower 95% Confidence Limit	1.28	-0.148	0.0843	0.156	0.161	0.592
	P - Value	43.6	2.59	7.07	9.34	9.51	48.5
440 ± 20km	Correlation Co-efficient	0.685	-0.954	-0.827	-0.830	-0.826	-0.119
	Upper 95% Confidence Limit	-0.236	-2.04	-1.91	-1.92	-1.91	-1.04
	Lower 95% Confidence Limit	1.61	0.132	0.260	0.257	0.261	0.804
	P - Value	14.5	8.53	13.6	13.4	13.6	80.0
480 ± 20km	Correlation Co-efficient	1.38	-0.0400	0.00997	0.374	0.371	1.33
	Upper 95% Confidence Limit	0.537	-1.02	-0.970	-0.608	-0.611	0.484
	Lower 95% Confidence Limit	2.23	0.940	0.990	1.36	1.35	2.18
	P - Value	0.135	93.6	98.4	45.5	45.9	0.206

Table 9.5: Storm 2, Day 4 Results.

Storm 2, Day 4: 27th July 2004							
Assumed IPP Altitude		S_4	σ_ϕ(1s)	σ_ϕ(3s)	σ_ϕ(10s)	σ_ϕ(30s)	σ_ϕ(60s)
120 ± 20km	Correlation Co-efficient	0.0391	-1.03	-0.535	-0.300	-0.297	-0.198
	Upper 95% Confidence Limit	-0.658	-1.73	-1.33	-1.09	-1.09	-0.896
	Lower 95% Confidence Limit	0.737	-0.332	0.260	0.495	0.497	0.500
	P - Value	91.3	0.381	18.7	46.0	46.3	57.8
160 ± 20km	Correlation Co-efficient	-1.98	1.69	-0.605	-0.644	-0.644	0.587
	Upper 95% Confidence Limit	-2.96	0.710	-1.40	-1.44	-1.44	-0.392
	Lower 95% Confidence Limit	-1.01	2.67	0.191	0.153	0.152	1.57
	P - Value	0.00691	0.0720	13.6	11.3	11.3	24.0
200 ± 20km	Correlation Co-efficient	-0.0964	0.698	2.15	1.33	1.33	1.04
	Upper 95% Confidence Limit	-1.06	-0.267	0.904	0.0842	0.0819	0.0710
	Lower 95% Confidence Limit	0.869	1.66	3.40	2.57	2.57	2.00
	P - Value	84.5	15.6	0.0717	3.64	3.67	3.54
240 ± 20km	Correlation Co-efficient	-0.366	-0.590	1.95	1.12	1.11	-0.226
	Upper 95% Confidence Limit	-1.31	-1.54	0.847	0.0157	0.0123	-1.17
	Lower 95% Confidence Limit	0.579	0.356	3.05	2.22	2.21	0.720
	P - Value	44.8	22.2	0.0526	4.68	4.75	64.0
280 ± 20km	Correlation Co-efficient	0.466	-0.920	-0.514	-0.634	-0.638	-1.02
	Upper 95% Confidence Limit	-0.477	-1.86	-1.61	-1.73	-1.73	-1.97
	Lower 95% Confidence Limit	1.41	0.0235	0.581	0.461	0.458	-0.0784
	P - Value	33.2	5.60	35.8	25.7	25.4	3.38
320 ± 20km	Correlation Co-efficient	1.43	-1.35	-1.93	-1.74	-1.74	-1.64
	Upper 95% Confidence Limit	0.510	-2.27	-3.00	-2.81	-2.81	-2.56
	Lower 95% Confidence Limit	2.35	-0.429	-0.855	-0.663	-0.664	-0.7163
	P - Value	0.231	0.407	0.0432	0.152	0.152	0.0492

Storm 2, Day 4: 27th July 2004 Continued							
360 ± 20km	Correlation Co-efficient	1.92	-1.03	-1.49	-1.39	-1.39	-1.23
	Upper 95% Confidence Limit	0.999	-1.95	-2.57	-2.47	-2.47	-2.15
	Lower 95% Confidence Limit	2.84	-0.104	-0.411	-0.312	-0.311	-0.313
	P - Value	0.00440	2.91	0.679	1.15	1.16	0.865
400 ± 20km	Correlation Co-efficient	2.23	-0.535	-0.965	-0.763	-0.758	-0.811
	Upper 95% Confidence Limit	1.31	-1.46	-2.04	-1.84	-1.83	-1.74
	Lower 95% Confidence Limit	3.16	0.391	0.110	0.312	0.317	0.115
	P - Value	0.000231	25.8	7.84	16.4	16.7	8.62
440 ± 20km	Correlation Co-efficient	2.18	-0.439	2.50	1.88	1.88	-0.764
	Upper 95% Confidence Limit	1.25	-1.37	1.17	0.556	0.550	-1.69
	Lower 95% Confidence Limit	3.11	0.489	3.82	3.21	3.20	0.164
	P - Value	0.000415	35.4	0.0218	0.542	0.557	10.6
480 ± 20km	Correlation Co-efficient	0.909	0.700	0.602	1.10	1.09	0.803
	Upper 95% Confidence Limit	0.0515	-0.1585	-0.399	0.101	0.0916	-0.0547
	Lower 95% Confidence Limit	1.77	1.56	1.60	2.10	2.09	1.66
	P - Value	3.77	11.0	23.8	3.09	3.24	6.65

Table 9.6: Storm 2, Day 5 Results.

Storm 2, Day 5: 28th July 2004							
Assumed IPP Altitude		S_4	σ_ϕ(1s)	σ_ϕ(3s)	σ_ϕ(10s)	σ_ϕ(30s)	σ_ϕ(60s)
120 ± 20km	Correlation Co-efficient	-0.0720	-0.478	-0.584	-0.835	-0.842	-1.01
	Upper 95% Confidence Limit	-0.743	-1.15	-1.68	-1.93	-1.94	-1.68
	Lower 95% Confidence Limit	0.599	0.194	0.509	0.257	0.250	-0.333
	P - Value	83.3	16.3	29.5	13.4	13.1	0.339
160 ± 20km	Correlation Co-efficient	0.588	-0.213	-0.689	-0.938	-0.945	-0.128
	Upper 95% Confidence Limit	-0.0846	-0.887	-1.77	-2.02	-2.03	-0.802
	Lower 95% Confidence Limit	1.26	0.461	0.395	0.146	0.140	0.547
	P - Value	8.67	53.5	21.3	9.00	8.77	71.1
200 ± 20km	Correlation Co-efficient	0.346	-0.0980	0.0845	-0.0132	-0.0175	0.623
	Upper 95% Confidence Limit	-0.330	-0.775	-1.00	-1.10	-1.11	-0.0543
	Lower 95% Confidence Limit	1.02	0.579	1.17	1.07	1.07	1.30
	P - Value	31.6	77.7	87.9	98.1	97.5	7.14
240 ± 20km	Correlation Co-efficient	0.449	-0.643	2.03	1.45	1.45	-1.18
	Upper 95% Confidence Limit	-0.228	-1.32	0.968	0.390	0.387	-1.86
	Lower 95% Confidence Limit	1.13	0.0344	3.09	2.51	2.50	-0.499
	P - Value	19.4	6.28	0.0177	0.733	0.746	0.0665
280 ± 20km	Correlation Co-efficient	0.428	-0.575	-0.565	-0.476	-0.476	-0.764
	Upper 95% Confidence Limit	-0.251	-1.26	-1.63	-1.54	-1.54	-1.44
	Lower 95% Confidence Limit	1.11	0.106	0.495	0.584	0.584	-0.0826
	P - Value	21.7	9.80	29.6	37.9	37.9	2.80
320 ± 20km	Correlation Co-efficient	-0.0273	-0.616	1.96	1.40	1.40	-0.571
	Upper 95% Confidence Limit	-0.708	-1.30	0.902	0.342	0.339	-1.25
	Lower 95% Confidence Limit	0.653	0.0656	3.02	2.46	2.45	0.111
	P - Value	93.7	7.65	0.0281	0.951	0.966	10.1

Storm 2, Day 5: 28th July 2004 Continued							
360 ± 20km	Correlation Co-efficient	0.734	-0.294	-0.223	-0.418	-0.425	-0.00948
	Upper 95% Confidence Limit	0.0525	-0.977	-1.50	-1.70	-1.70	-0.692
	Lower 95% Confidence Limit	1.41	0.388	1.06	0.862	0.855	0.673
	P - Value	3.48	39.8	73.2	52.2	51.5	97.8
400 ± 20km	Correlation Co-efficient	0.432	-0.186	2.28	1.66	1.66	0.614
	Upper 95% Confidence Limit	-0.250	-0.869	1.11	0.490	0.487	-0.0691
	Lower 95% Confidence Limit	1.11	0.497	3.45	2.84	2.83	1.30
	P - Value	21.5	59.3	0.0141	0.546	0.555	7.81
440 ± 20km	Correlation Co-efficient	0.564	-0.307	0.196	0.0897	0.0895	0.135
	Upper 95% Confidence Limit	-0.119	-0.991	-0.986	-1.09	-1.09	-0.549
	Lower 95% Confidence Limit	1.25	0.376	1.38	1.27	1.27	0.819
	P - Value	10.5	37.9	74.5	88.2	88.2	69.8
480 ± 20km	Correlation Co-efficient	0.840	-0.000264	-0.769	-0.921	-0.927	0.588
	Upper 95% Confidence Limit	0.158	-0.683	-1.74	-1.89	-1.90	-0.0954
	Lower 95% Confidence Limit	1.52	0.683	0.200	0.0488	0.0424	1.27
	P - Value	1.58	99.9	12.0	6.27	6.09	9.17

Table 9.7: Storm 3, Day 1 Results.

Storm 3, Day 1: 8th Nov 2004							
Assumed IPP Altitude		S_4	σ_ϕ(1s)	σ_ϕ(3s)	σ_ϕ(10s)	σ_ϕ(30s)	σ_ϕ(60s)
120 ± 20km	Correlation Co-efficient	0.384	1.16	-0.997	-1.03	-1.03	2.16
	Upper 95% Confidence Limit	-0.704	0.0710	-1.78	-1.81	-1.81	1.07
	Lower 95% Confidence Limit	1.47	2.25	-0.215	-0.247	-0.246	3.25
	P - Value	48.9	3.68	1.25	0.994	1.00	0.0107
160 ± 20km	Correlation Co-efficient	0.574	0.741	-1.47	-1.62	-1.62	-0.0118
	Upper 95% Confidence Limit	-0.500	-0.337	-2.55	-2.69	-2.69	-1.09
	Lower 95% Confidence Limit	1.65	1.82	-0.401	-0.546	-0.546	1.07
	P - Value	29.5	17.8	0.712	0.312	0.312	98.3
200 ± 20km	Correlation Co-efficient	0.717	0.393	-0.465	0.0458	0.0554	-1.29
	Upper 95% Confidence Limit	-0.375	-0.703	-1.56	-1.05	-1.04	-2.38
	Lower 95% Confidence Limit	1.81	1.49	0.629	1.14	1.15	-0.191
	P - Value	19.8	48.2	40.5	93.5	92.1	2.14
240 ± 20km	Correlation Co-efficient	0.446	-0.356	4.39	3.40	3.39	-0.393
	Upper 95% Confidence Limit	-0.646	-1.45	3.33	2.33	2.32	-1.49
	Lower 95% Confidence Limit	1.54	0.741	5.46	4.47	4.46	0.705
	P - Value	42.3	52.5	$8.50\text{x}10^{-14}$	$5.06\text{x}10^{-08}$	$5.34\text{x}10^{-08}$	48.3
280 ± 20km	Correlation Co-efficient	0.539	0.0801	3.71	2.68	2.67	-0.0267
	Upper 95% Confidence Limit	-0.556	-1.02	2.46	1.42	1.42	-1.13
	Lower 95% Confidence Limit	1.64	1.18	4.96	3.93	3.92	1.08
	P - Value	33.5	88.7	$6.12\text{x}10^{-07}$	0.00277	0.00288	96.2
320 ± 20km	Correlation Co-efficient	-0.821	0.574	-0.0668	-0.0455	-0.0458	1.05
	Upper 95% Confidence Limit	-1.90	-0.509	-1.14	-1.12	-1.12	-0.0347
	Lower 95% Confidence Limit	0.256	1.66	1.00	1.02	1.02	2.13
	P - Value	13.5	29.9	90.3	93.4	93.3	5.78

Storm 3, Day 1: 8th Nov 2004 Continued							
360 ± 20km	Correlation Co-efficient	-0.772	0.472	2.76	1.71	1.71	0.889
	Upper 95% Confidence Limit	-1.85	-0.612	1.50	0.455	0.452	-0.196
	Lower 95% Confidence Limit	0.307	1.56	4.02	2.97	2.97	1.97
	P - Value	16.1	39.4	0.00168	0.763	0.774	10.8
400 ± 20km	Correlation Co-efficient	-0.818	0.398	-0.759	-0.593	-0.590	0.758
	Upper 95% Confidence Limit	-1.90	-0.688	-1.95	-1.79	-1.79	-0.329
	Lower 95% Confidence Limit	0.262	1.48	0.437	0.603	0.606	1.84
	P - Value	13.8	47.2	21.3	33.1	33.3	17.2
440 ± 20km	Correlation Co-efficient	-0.828	0.488	-1.57	-1.41	-1.41	0.905
	Upper 95% Confidence Limit	-1.91	-0.602	-2.77	-2.61	-2.61	-0.186
	Lower 95% Confidence Limit	0.257	1.58	-0.374	-0.210	-0.209	2.00
	P - Value	13.5	38.0	1.01	2.12	2.13	10.47
480 ± 20km	Correlation Co-efficient	-0.556	0.249	-0.693	-0.995	-0.995	0.0841
	Upper 95% Confidence Limit	-1.56	-0.764	-1.66	-1.97	-1.97	-0.929
	Lower 95% Confidence Limit	0.451	1.26	0.279	-0.0228	-0.0230	1.10
	P - Value	27.9	63.0	16.2	4.49	4.48	87.1

Table 9.8: Storm 3, Day 2 Results.

Storm 3, Day 2: 9th Nov 2004							
Assumed IPP Altitude		S_4	σ_ϕ(1s)	σ_ϕ(3s)	σ_ϕ(10s)	σ_ϕ(30s)	σ_ϕ(60s)
120 ± 20km	Correlation Co-efficient	-0.119	-3.30	-0.241	-0.310	-0.309	-5.40
	Upper 95% Confidence Limit	-0.909	-4.09	-1.03	-1.10	-1.10	-6.19
	Lower 95% Confidence Limit	0.671	-2.50	0.552	0.483	0.484	-4.61
	P - Value	76.8	$3.46\text{x}10^{-14}$	55.2	44.4	44.5	$1.18\text{x}10^{-38}$
160 ± 20km	Correlation Co-efficient	-0.0440	-3.23	0.391	0.339	0.333	-5.31
	Upper 95% Confidence Limit	-0.836	-4.02	-0.403	-0.456	-0.461	-6.10
	Lower 95% Confidence Limit	0.747	-2.43	1.18	1.13	1.13	-4.51
	P - Value	91.3	$1.53\text{x}10^{-13}$	33.5	40.3	41.1	$3.24\text{x}10^{-37}$
200 ± 20km	Correlation Co-efficient	0.111	-3.86	-0.116	-0.0698	-0.0701	-5.10
	Upper 95% Confidence Limit	-0.688	-4.66	-1.35	-1.30	-1.30	-5.90
	Lower 95% Confidence Limit	0.910	-3.06	1.11	1.16	1.16	-4.30
	P - Value	78.5	$3.20\text{x}10^{-19}$	85.6	91.1	91.1	$9.07\text{x}10^{-34}$
240 ± 20km	Correlation Co-efficient	-0.00308	-0.956	0.00693	0.140	0.140	-1.66
	Upper 95% Confidence Limit	-1.10	-2.05	-1.11	-0.978	-0.978	-2.75
	Lower 95% Confidence Limit	1.09	0.139	1.12	1.26	1.26	-0.561
	P - Value	99.6	8.71	99.3	80.6	80.6	0.305
280 ± 20km	Correlation Co-efficient	1.08	1.04	3.27	3.69	3.67	0.569
	Upper 95% Confidence Limit	-0.0396	-0.0829	1.96	2.38	2.36	-0.557
	Lower 95% Confidence Limit	2.20	2.17	4.58	5.00	4.98	1.69
	P - Value	5.87	6.95	0.000108	$3.75\text{x}10^{-06}$	$4.47\text{x}10^{-06}$	32.2
320 ± 20km	Correlation Co-efficient	1.52	1.53	0.847	1.19	1.17	1.15
	Upper 95% Confidence Limit	0.431	0.438	-0.238	0.102	0.0868	0.0543
	Lower 95% Confidence Limit	2.62	2.63	1.93	2.27	2.26	2.25
	P - Value	0.627	0.608	12.6	3.20	3.43	3.97

Storm 3, Day 2: 9th Nov 2004 Continued							
360 ± 20km	Correlation Co-efficient	2.04	1.66	0.280	0.531	0.526	1.23
	Upper 95% Confidence Limit	0.936	0.555	-0.810	-0.560	-0.564	0.130
	Lower 95% Confidence Limit	3.13	2.76	1.37	1.62	1.62	2.34
	P - Value	0.0285	0.320	61.4	34.0	34.4	2.84
400 ± 20km	Correlation Co-efficient	1.28	-1.38	0.840	1.11	1.10	-2.26
	Upper 95% Confidence Limit	0.178	-2.48	-0.375	-0.107	-0.113	-3.37
	Lower 95% Confidence Limit	2.39	-0.271	2.06	2.33	2.32	-1.15
	P - Value	2.29	1.47	17.6	7.40	7.54	0.00643
440 ± 20km	Correlation Co-efficient	0.158	-1.27	0.469	1.16	1.14	-1.77
	Upper 95% Confidence Limit	-0.952	-2.39	-0.785	-0.0960	-0.108	-2.88
	Lower 95% Confidence Limit	1.27	-0.162	1.72	2.41	2.40	-0.651
	P - Value	78.0	2.47	46.2	7.03	7.33	0.190
480 ± 20km	Correlation Co-efficient	-1.06	-1.016	-0.403	-0.492	-0.496	-1.32
	Upper 95% Confidence Limit	-2.10	-2.06	-1.39	-1.48	-1.49	-2.36
	Lower 95% Confidence Limit	-0.0194	0.0301	0.588	0.500	0.495	-0.275
	P - Value	4.59	5.70	42.5	33.1	32.7	1.33

Table 9.9: Storm 3, Day 3 Results.

Storm 3, Day 3: 10th Nov 2004							
Assumed IPP Altitude		S_4	σ_ϕ(1s)	σ_ϕ(3s)	σ_ϕ(10s)	σ_ϕ(30s)	σ_ϕ(60s)
120 ± 20km	Correlation Co-efficient	-2.62	-4.08	-0.268	0.332	0.350	-5.64
	Upper 95% Confidence Limit	-3.41	-4.87	-1.38	-0.784	-0.766	-6.43
	Lower 95% Confidence Limit	-1.83	-3.29	0.847	1.45	1.46	-4.85
	P - Value	$8.71\text{x}10^{-09}$	$5.11\text{x}10^{-22}$	63.8	56.0	53.9	$2.91\text{x}10^{-42}$
160 ± 20km	Correlation Co-efficient	-2.52	-4.13	-0.605	-0.600	-0.600	-5.71
	Upper 95% Confidence Limit	-3.31	-4.92	-1.71	-1.71	-1.71	-6.50
	Lower 95% Confidence Limit	-1.73	-3.34	0.505	0.511	0.511	-4.92
	P - Value	$4.35\text{x}10^{-08}$	$1.58\text{x}10^{-22}$	28.5	28.6	29.0	$3.10\text{x}10^{-43}$
200 ± 20km	Correlation Co-efficient	-1.67	-3.46	0.289	0.901	0.893	-5.54
	Upper 95% Confidence Limit	-2.47	-4.26	-0.851	-0.240	-0.248	-6.33
	Lower 95% Confidence Limit	-0.875	-2.67	1.43	2.04	2.03	-4.74
	P - Value	0.00389	$1.71\text{x}10^{-15}$	61.9	12.2	12.5	$4.20\text{x}10^{-40}$
240 ± 20km	Correlation Co-efficient	-1.81	-3.36	1.66	3.10	3.09	-5.36
	Upper 95% Confidence Limit	-2.61	-4.16	0.540	1.98	1.96	-6.15
	Lower 95% Confidence Limit	-1.01	-2.57	2.79	4.23	4.21	-4.56
	P - Value	0.000858	$1.51\text{x}10^{-14}$	0.372	$6.71\text{x}10^{-06}$	$7.91\text{x}10^{-06}$	$2.48\text{x}10^{-37}$
280 ± 20km	Correlation Co-efficient	-1.71	-3.39	-0.302	0.247	0.271	-5.60
	Upper 95% Confidence Limit	-2.51	-4.19	-1.59	-1.04	-1.02	-6.40
	Lower 95% Confidence Limit	-0.903	-2.58	0.986	1.54	1.56	-4.80
	P - Value	0.00312	$1.52\text{x}10^{-14}$	64.6	70.7	68.0	$2.48\text{x}10^{-40}$
320 ± 20km	Correlation Co-efficient	-1.79	-3.45	-0.350	0.273	0.302	-5.90
	Upper 95% Confidence Limit	-2.60	-4.26	-1.41	-0.783	-0.755	-6.71
	Lower 95% Confidence Limit	-0.988	-2.65	0.706	1.33	1.36	-5.10
	P - Value	0.00127	$4.93\text{x}10^{-15}$	51.6	61.2	57.6	$1.59\text{x}10^{-44}$

Storm 3, Day 3: 10th Nov 2004 Continued							
360 ± 20km	Correlation Co-efficient	-2.40	-3.30	-0.461	-0.511	0.302	-5.82
	Upper 95% Confidence Limit	-0.788	-4.10	-1.55	-1.60	-0.755	-6.62
	Lower 95% Confidence Limit	0.0105	-2.49	0.628	0.578	1.36	-5.01
	P - Value	-1.91	1.14×10^{-13}	40.7	35.8	57.6	3.25×10^{-43}
400 ± 20km	Correlation Co-efficient	-2.72	-2.94	-0.805	-0.440	-0.434	-5.27
	Upper 95% Confidence Limit	-1.10	-3.74	-1.91	-1.55	-1.54	-6.08
	Lower 95% Confidence Limit	0.000351	-2.13	0.299	0.665	0.672	-4.46
	P - Value	-1.92	1.22×10^{-10}	15.3	43.5	44.2	3.82×10^{-35}
440 ± 20km	Correlation Co-efficient	-2.72	-2.94	0.148	0.0656	0.0836	-5.27
	Upper 95% Confidence Limit	-1.11	-3.75	-0.958	-1.04	-1.02	-6.08
	Lower 95% Confidence Limit	0.000340	-2.13	1.25	1.17	1.19	-4.46
	P - Value	-2.25	1.16×10^{-10}	79.3	90.8	88.2	4.82×10^{-35}
480 ± 20km	Correlation Co-efficient	-3.06	-2.98	-0.634	-0.628	-0.627	-5.77
	Upper 95% Confidence Limit	-1.44	-3.79	-1.66	-1.66	-1.65	-6.58
	Lower 95% Confidence Limit	5.07×10^{-06}	-2.17	0.392	0.400	0.401	-4.96
	P - Value	-2.40	5.90×10^{-11}	22.6	23.1	23.2	4.61×10^{-42}

Table 9.10: Storm 3, Day 4 Results.

Storm 3, Day 4: 11th Nov 2004							
Assumed IPP Altitude		S_4	σ_ϕ (1s)	σ_ϕ (3s)	σ_ϕ (10s)	σ_ϕ (30s)	σ_ϕ (60s)
120 ± 20km	Correlation Co-efficient	0.238	-1.02	-0.720	-0.750	-0.743	-2.07
	Upper 95% Confidence Limit	-0.549	-1.81	-1.79	-1.82	-1.81	-2.86
	Lower 95% Confidence Limit	1.03	-0.231	0.346	0.317	0.323	-1.28
	P - Value	55.3	1.13	18.5	16.8	17.2	2.6288E-05
160 ± 20km	Correlation Co-efficient	0.420	-0.945	-1.06	-1.11	-1.10	-1.97
	Upper 95% Confidence Limit	-0.370	-1.74	-2.13	-2.18	-2.18	-2.76
	Lower 95% Confidence Limit	1.21	-0.154	0.0187	-0.0320	-0.0254	-1.18
	P - Value	29.7	1.92	5.41	4.36	4.48	0.000103
200 ± 20km	Correlation Co-efficient	0.432	-0.826	-0.741	-0.744	-0.737	-1.54
	Upper 95% Confidence Limit	-0.366	-1.63	-1.92	-1.92	-1.91	-2.34
	Lower 95% Confidence Limit	1.23	-0.0260	0.434	0.431	0.438	-0.742
	P - Value	28.9	4.30	21.6	21.4	21.9	0.0159
240 ± 20km	Correlation Co-efficient	0.283	-0.779	-0.576	-0.580	-0.574	-1.60
	Upper 95% Confidence Limit	-0.520	-1.58	-1.64	-1.64	-1.63	-2.41
	Lower 95% Confidence Limit	1.09	0.0244	0.483	0.480	0.486	-0.797
	P - Value	48.9	5.74	28.6	28.4	28.8	0.00956
280 ± 20km	Correlation Co-efficient	0.217	-1.05	-0.291	-0.508	-0.508	-1.86
	Upper 95% Confidence Limit	-0.596	-1.86	-1.39	-1.61	-1.61	-2.68
	Lower 95% Confidence Limit	1.03	-0.232	0.814	0.597	0.597	-1.05
	P - Value	60.1	1.18	60.6	36.7	36.7	0.000743
320 ± 20km	Correlation Co-efficient	0.357	-0.892	-0.271	-0.303	-0.302	-1.87
	Upper 95% Confidence Limit	-0.457	-1.71	-1.30	-1.33	-1.33	-2.68
	Lower 95% Confidence Limit	1.17	-0.0781	0.758	0.726	0.727	-1.05
	P - Value	39.0	3.17	60.6	56.4	56.5	0.000704

Storm 3, Day 4: 11th Nov 2004 Continued							
360 ± 20km	Correlation Co-efficient	0.176	-0.975	-0.474	-0.605	-0.606	-1.89
	Upper 95% Confidence Limit	-0.640	-1.79	-1.54	-1.67	-1.67	-2.71
	Lower 95% Confidence Limit	0.992	-0.159	0.589	0.459	0.458	-1.07
	P - Value	67.2	1.92	38.2	26.5	26.5	0.000571
400 ± 20km	Correlation Co-efficient	0.100	-1.01	-0.458	-0.599	-0.601	-1.91
	Upper 95% Confidence Limit	-0.720	-1.83	-1.54	-1.68	-1.69	-2.73
	Lower 95% Confidence Limit	0.920	-0.192	0.626	0.485	0.483	-1.09
	P - Value	81.1	1.56	40.8	27.9	27.7	0.000493
440 ± 20km	Correlation Co-efficient	-0.00609	-1.08	-0.532	-0.652	-0.651	-1.96
	Upper 95% Confidence Limit	-0.827	-1.91	-1.62	-1.74	-1.74	-2.78
	Lower 95% Confidence Limit	0.815	-0.263	0.553	0.433	0.434	-1.14
	P - Value	98.8	0.970	33.6	23.9	24.0	0.000293
480 ± 20km	Correlation Co-efficient	0.0969	-0.917	0.591	0.198	0.199	-1.87
	Upper 95% Confidence Limit	-0.726	-1.74	-0.431	-0.825	-0.824	-2.70
	Lower 95% Confidence Limit	0.919	-0.0943	1.61	1.22	1.22	-1.05
	P - Value	81.7	2.89	25.7	70.4	70.3	0.000837

Table 9.11: Storm 4, Day 1 Results.

Storm 4, Day 1: 14th May 2005							
Assumed IPP Altitude		S_4	σ_ϕ(1s)	σ_ϕ(3s)	σ_ϕ(10s)	σ_ϕ(30s)	σ_ϕ(60s)
120 ± 20km	Correlation Co-efficient	3.02	No data	No data	8.12	8.13	No data
	Upper 95% Confidence Limit	-3.44	No data	No data	-6.75	-6.74	No data
	Lower 95% Confidence Limit	9.45	No data	No data	22.6	22.7	No data
	P - Value	36.0	No data	No data	28.4	28.3	No data
160 ± 20km	Correlation Co-efficient	0.672	No data	No data	4.45	4.44	No data
	Upper 95% Confidence Limit	-6.08	No data	No data	-10.7	-10.7	No data
	Lower 95% Confidence Limit	7.42	No data	No data	19.4	19.4	No data
	P - Value	84.5	No data	No data	56.5	56.5	No data
200 ± 20km	Correlation Co-efficient	-0.740	No data	No data	-2.56	-2.57	No data
	Upper 95% Confidence Limit	-7.75	No data	No data	-20.0	-20.0	No data
	Lower 95% Confidence Limit	6.28	No data	No data	15.0	15.0	No data
	P - Value	83.6	No data	No data	77.6	77.5	No data
240 ± 20km	Correlation Co-efficient	-3.30	No data	No data	6.03	6.05	No data
	Upper 95% Confidence Limit	-10.3	No data	No data	-11.7	-11.7	No data
	Lower 95% Confidence Limit	3.72	No data	No data	23.4	23.4	No data
	P - Value	35.7	No data	No data	50.6	50.5	No data
280 ± 20km	Correlation Co-efficient	-4.29	No data	No data	6.03	6.05	No data
	Upper 95% Confidence Limit	-11.4	No data	No data	-11.7	-11.7	No data
	Lower 95% Confidence Limit	2.84	No data	No data	23.4	23.4	No data
	P - Value	23.8	No data	No data	50.6	50.5	No data
320 ± 20km	Correlation Co-efficient	-5.22	No data	No data	5.99	6.01	No data
	Upper 95% Confidence Limit	-12.6	No data	No data	-12.2	-12.2	No data
	Lower 95% Confidence Limit	2.23	No data	No data	23.8	23.8	No data
	P - Value	17.0	No data	No data	51.9	51.8	No data

Storm 4, Day 1: 14th May 2005 Continued							
360 ± 20km	Correlation Co-efficient	1.13	No data	No data	4.94	4.95	No data
	Upper 95% Confidence Limit	-6.50	No data	No data	-14.5	-14.4	No data
	Lower 95% Confidence Limit	8.74	No data	No data	24.0	24.0	No data
	P - Value	77.2	No data	No data	61.9	61.8	No data
400 ± 20km	Correlation Co-efficient	0.558	No data	No data	7.63	7.65	No data
	Upper 95% Confidence Limit	-7.08	No data	No data	-12.4	-12.4	No data
	Lower 95% Confidence Limit	8.19	No data	No data	27.1	27.1	No data
	P - Value	88.6	No data	No data	45.5	45.4	No data
440 ± 20km	Correlation Co-efficient	0.481	No data	No data	9.23	9.26	No data
	Upper 95% Confidence Limit	-7.15	No data	No data	-10.8	-10.8	No data
	Lower 95% Confidence Limit	8.11	No data	No data	28.5	28.6	No data
	P - Value	90.2	No data	No data	36.6	36.5	No data
480 ± 20km	Correlation Co-efficient	0.916	No data	No data	1.34	1.33	No data
	Upper 95% Confidence Limit	-6.721	No data	No data	-18.6	-18.6	No data
	Lower 95% Confidence Limit	8.54	No data	No data	21.1	21.1	No data
	P - Value	81.4	No data	No data	89.6	89.6	No data

Table 9.12: Storm 4, Day 2 Results.

Storm 4, Day 2: 15th May 2005							
Assumed IPP Altitude		S_4	σ_ϕ(1s)	σ_ϕ(3s)	σ_ϕ(10s)	σ_ϕ(30s)	σ_ϕ(60s)
120 ± 20km	Correlation Co-efficient	-1.98	No data	No data	7.12	7.13	No data
	Upper 95% Confidence Limit	-4.06	No data	No data	-0.703	-0.694	No data
	Lower 95% Confidence Limit	0.108	No data	No data	14.9	14.9	No data
	P - Value	6.32	No data	No data	7.44	7.40	No data
160 ± 20km	Correlation Co-efficient	-1.49	No data	No data	-3.61	-3.61	No data
	Upper 95% Confidence Limit	-3.58	No data	No data	-11.3	-11.3	No data
	Lower 95% Confidence Limit	0.605	No data	No data	4.11	4.10	No data
	P - Value	16.4	No data	No data	35.9	35.9	No data
200 ± 20km	Correlation Co-efficient	-1.47	No data	No data	2.50	2.50	No data
	Upper 95% Confidence Limit	-3.73	No data	No data	-5.12	-5.12	No data
	Lower 95% Confidence Limit	0.798	No data	No data	10.1	10.1	No data
	P - Value	20.4	No data	No data	52.1	52.0	No data
240 ± 20km	Correlation Co-efficient	-1.23	No data	No data	-3.73	-3.73	No data
	Upper 95% Confidence Limit	-3.54	No data	No data	-11.6	-11.6	No data
	Lower 95% Confidence Limit	1.08	No data	No data	4.19	4.19	No data
	P - Value	29.5	No data	No data	35.6	35.6	No data
280 ± 20km	Correlation Co-efficient	-2.46	No data	No data	8.34	8.35	No data
	Upper 95% Confidence Limit	-4.96	No data	No data	0.416	0.424	No data
	Lower 95% Confidence Limit	0.0396	No data	No data	16.2	16.2	No data
	P - Value	5.37	No data	No data	3.92	3.90	No data
320 ± 20km	Correlation Co-efficient	-3.51	No data	-0.350	0.273	0.302	No data
	Upper 95% Confidence Limit	-6.18	No data	-1.41	-0.783	-0.755	No data
	Lower 95% Confidence Limit	-0.843	No data	0.706	1.33	1.36	No data
	P - Value	0.994	No data	51.69	61.2	57.6	No data

Storm 4, Day 2: 15th May 2005 Continued							
360 ± 20km	Correlation Co-efficient	-3.62	No data	No data	-3.83	-3.83	No data
	Upper 95% Confidence Limit	-6.31	No data	No data	-11.8	-11.8	No data
	Lower 95% Confidence Limit	-0.930	No data	No data	4.19	4.19	No data
	P - Value	0.839	No data	No data	34.9	34.9	No data
400 ± 20km	Correlation Co-efficient	-3.21	No data	No data	23.8	23.8	No data
	Upper 95% Confidence Limit	-5.98	No data	No data	16.4	16.5	No data
	Lower 95% Confidence Limit	-0.426	No data	No data	30.9	31.0	No data
	P - Value	2.38	No data	No data	$7.53x10^{-08}$	$7.3x10^{-08}$	No data
440 ± 20km	Correlation Co-efficient	-3.38	No data	No data	19.3	19.3	No data
	Upper 95% Confidence Limit	-6.15	No data	No data	11.3	11.3	No data
	Lower 95% Confidence Limit	-0.609	No data	No data	26.9	27.0	No data
	P - Value	1.69	No data	No data	0.000276	0.000271	No data
480 ± 20km	Correlation Co-efficient	-3.52	No data	-0.634	-0.628	-0.627	No data
	Upper 95% Confidence Limit	-6.46	No data	-1.66	-1.66	-1.65	No data
	Lower 95% Confidence Limit	-0.568	No data	0.392	0.400	0.401	No data
	P - Value	1.94	No data	22.6	23.1	23.2	No data

Table 9.13: Storm 4, Day 3 Results.

Storm 4, Day 3: 16th May 2005							
Assumed IPP Altitude		S_4	σ_ϕ(1s)	σ_ϕ(3s)	σ_ϕ(10s)	σ_ϕ(30s)	σ_ϕ(60s)
120 ± 20km	Correlation Co-efficient	-4.89	No data	No data	-0.420	-0.420	No data
	Upper 95% Confidence Limit	-25.9	No data	No data	-2.31	-2.31	No data
	Lower 95% Confidence Limit	16.6	No data	No data	1.47	1.47	No data
	P - Value	65.7	No data	No data	66.4	66.4	No data
160 ± 20km	Correlation Co-efficient	-15.4	No data	No data	-0.871	-0.871	No data
	Upper 95% Confidence Limit	-37.2	No data	No data	-2.78	-2.78	No data
	Lower 95% Confidence Limit	8.08	No data	No data	1.03	1.03	No data
	P - Value	19.7	No data	No data	37.0	37.0	No data
200 ± 20km	Correlation Co-efficient	-19.0	No data	No data	0.872	0.871	No data
	Upper 95% Confidence Limit	-40.5	No data	No data	-1.14	-1.14	No data
	Lower 95% Confidence Limit	4.58	No data	No data	2.88	2.88	No data
	P - Value	11.3	No data	No data	39.5	39.6	No data
240 ± 20km	Correlation Co-efficient	-15.7	No data	No data	-0.646	-0.646	No data
	Upper 95% Confidence Limit	-38.1	No data	No data	-3.25	-3.25	No data
	Lower 95% Confidence Limit	8.49	No data	No data	1.96	1.96	No data
	P - Value	20.2	No data	No data	62.7	62.7	No data
280 ± 20km	Correlation Co-efficient	-12.2	No data	No data	1.91	1.91	No data
	Upper 95% Confidence Limit	-35.9	No data	No data	-1.12	-1.12	No data
	Lower 95% Confidence Limit	13.0	No data	No data	4.93	4.93	No data
	P - Value	34.2	No data	No data	21.6	21.7	No data
320 ± 20km	Correlation Co-efficient	-11.4	No data	No data	3.01	3.00	No data
	Upper 95% Confidence Limit	-35.7	No data	No data	0.569	0.567	No data
	Lower 95% Confidence Limit	14.4	No data	No data	5.44	5.44	No data
	P - Value	38.7	No data	No data	1.56	1.57	No data

Storm 4, Day 3: 16th May 2005 Continued							
360 ± 20km	Correlation Co-efficient	-11.4	No data	No data	4.12	1.05	No data
	Upper 95% Confidence Limit	-35.8	No data	No data	1.05	7.18	No data
	Lower 95% Confidence Limit	14.4	No data	No data	7.18	0.846	No data
	P - Value	38.4	No data	No data	0.856	4.32	No data
400 ± 20km	Correlation Co-efficient	-11.8	No data	No data	4.31	1.44	No data
	Upper 95% Confidence Limit	-35.7	No data	No data	1.43	7.19	No data
	Lower 95% Confidence Limit	13.6	No data	No data	7.18	0.329	No data
	P - Value	36.2	No data	No data	0.333	2.69	No data
440 ± 20km	Correlation Co-efficient	-11.7	No data	No data	2.69	-0.306	No data
	Upper 95% Confidence Limit	-35.6	No data	No data	-0.311	5.69	No data
	Lower 95% Confidence Limit	13.7	No data	No data	5.68	7.84	No data
	P - Value	36.7	No data	No data	7.90	1.83	No data
480 ± 20km	Correlation Co-efficient	-12.30	No data	No data	1.83	-0.644	No data
	Upper 95% Confidence Limit	-36.0	No data	No data	-0.647	4.30	No data
	Lower 95% Confidence Limit	12.9	No data	No data	4.30	14.7	No data
	P - Value	33.7	No data	No data	14.8	1.05	No data

References

Beach, T. L. (2006), Perils of the GPS phase scintillation index (sigma(phi)), *Radio Science*, *41*(5).

Bengtsson, L., et al. (2006), Storm tracks and climate change, *Journal of Climate*, *19*(15), 3518-3543.

Bust, G. S., and C. N. Mitchell (2008), History, current state, and future directions of ionospheric imaging, *Reviews of Geophysics*, *46*(1).

Chaturvedi, P. K., et al. (1994), Effects of Field Line Mapping on the Gradient-Drift Instability in the Coupled E-Region and F-Region High-Latitude Ionosphere, *Radio Science*, *29*(1), 317-335.

Chen, F. F. (1984), *Introduction to Plasma Physics and Controlled Fusion*, 2nd ed., Plenum Press, New York.

Coley, W. R., and R. A. Heelis (1995), Adaptive Identification and Characterization of Polar Ionization Patches, *Journal of Geophysical Research-Space Physics*, *100*(A12), 23819-23827.

Davies, K. (1990), *Ionospheric Radio*, Peter Peregrinus, London.

Eriksson, S., et al. (2002), Comparing a spherical harmonic model of the global electric field distribution with Astrid-2 observations, *Journal of Geophysical Research-Space Physics*, *107*(A11).

Gershman, B. N., and A. A. Ponyatov (1988), A RELATION BETWEEN THE SPATIAL SPECTRA OF ELECTRON-DENSITY AND ELECTRIC-FIELD FLUCTUATIONS IN THE PRESENCE OF GRADIENT-DRIFT INSTABILITY IN THE IONOSPHERE, *Geomagnetizm I Aeronomiya*, *28*(3), 496-498.

Gondarenko, N. A., and P. N. Guzdar (1999), Gradient drift instability in high latitude plasma patches: ion inertial effects, *Geophysical Research Letters*, *26*(22), 3345-3348.

Gondarenko, N. A., and P. N. Guzdar (2001), Three-dimensional structuring characteristics of high-latitude plasma patches, *Journal of Geophysical Research-Space Physics*, *106*(A11), 24611-24620.

Gondarenko, N. A., et al. (2003), Structuring of high latitude plasma patches with variable drive, *Geophysical Research Letters*, *30*(4).

Gondarenko, N. A., and P. N. Guzdar (2004a), Plasma patch structuring by the nonlinear evolution of the gradient drift instability in the high-latitude ionosphere, *Journal of Geophysical Research-Space Physics*, *109*(A9).

Gondarenko, N. A., and P. N. Guzdar (2004b), Density and electric field fluctuations associated with the gradient drift instability in the high-latitude ionosphere, *Geophysical Research Letters*, *31*(11).

Gondarenko, N. A., et al. (2005), Generation and evolution of density irregularities due to self-focusing in ionospheric modifications, *Journal of Geophysical Research-Space Physics*, *110*(A9).

Gondarenko, N. A. a. P. N. G. (2006a), Nonlinear three-dimensional simulations of mesoscale structuring by multiple drives in high-latitude plasma patches, *Journal of Geophysical Research-Space Physics*, *111*(A8).

Gondarenko, N. A. a. P. N. G. (2006b), Simulations of the scintillation-producing irregularities in high-latitude plasma patches, *Geophysical Research Letters*, *33*(22).

Guzdar, P. N., et al. (1998), The thermal self-focusing instability near the critical surface in the high-latitude ionosphere, *Journal of Geophysical Research-Space Physics*, *103*(A2), 2231-2237.
Hargreaves, J. K. (1992), *The Solar-Terrestrial Environment*, Cambridge University Press.
Hodges, K. I. (1998), Feature-point detection using distance transforms: Application to tracking tropical convective complexes, *Monthly Weather Review*, *126*(3), 785-795.
Hodges, K. I. (1999), Adaptive constraints for feature tracking, *Monthly Weather Review*, *127*(6), 1362-1373.
Hodges, K. I., et al. (2003), A comparison of recent reanalysis datasets using objective feature tracking: Storm tracks and tropical easterly waves, *Monthly Weather Review*, *131*(9), 2012-2037.
Hodges, K. I. (2008), Confidence intervals and significance tests for spherical data derived from feature tracking, *Monthly Weather Review*, *136*(5), 1758-1777.
Hopsch, S. B., et al. (2007), West African storm tracks and their relationship to Atlantic tropical cyclones, *Journal of Climate*, *20*(11), 2468-2483.
Hoskins, B. J., and K. I. Hodges (2005), A new perspective on Southern Hemisphere storm tracks, *Journal of Climate*, *18*(20), 4108-4129.
Huba, J. D., et al. (1985), Ionospheric Turbulence - Interchange Instabilities and Chaotic Fluid Behavior, *Geophysical Research Letters*, *12*(1), 65-68.
Hunsucker, R. D. a. J. K. H. (2003), *The High-Latitude Ionosphere and its Effects on Radio Propagation*, 1 ed., 617 pp., Cambridge University Press, Cambridge.
Kaplan, E. D. e. (1996), *Understanding GPS: Principles and Applications.*, Artech House Publishers, Boston.
Kelley, M. C. (1989), *The Earth's Ionosphere: Plasma Physics and Electrodynamics*, 1 ed., Academic Press.
Kersley, L., et al. (1989), Scintillation and Eiscat Investigations of Gradient-Drift Irregularities in the High-Latitude Ionosphere, *Journal of Atmospheric and Terrestrial Physics*, *51*(4), 241-247.
Keskinen, M. J., et al. (1988), Nonlinear Evolution of the Kelvin-Helmholtz Instability in the High-Latitude Ionosphere, *Journal of Geophysical Research-Space Physics*, *93*(A1), 137-152.
Kintner, P. M., and C. E. Seyler (1985), The Status of Observations and Theory of High-Latitude Ionospheric and Magnetospheric Plasma Turbulence, *Space Science Reviews*, *41*(1-2), 91-129.
Kivanc, O., and R. A. Heelis (1997), Structures in ionospheric number density and velocity associated with polar cap ionization patches, *Journal of Geophysical Research-Space Physics*, *102*(A1), 307-318.
Kunitsyn, T. (2003), *Ionospheric Tomography*, Springer.
Macmillan, S., and S. Maus (2005), International geomagnetic reference field - the tenth generation, *Earth Planets and Space*, *57*(12), 1135-1140.
Maus, S., et al. (2005a), The 10th generation international geomagnetic reference field, *Physics of the Earth and Planetary Interiors*, *151*(3-4), 320-322.
Maus, S., et al. (2005b), The 10th-Generation International Geomagnetic Reference Field, *Geophysical Journal International*, *161*(3), 561-565.
Maus, S., et al. (2005c), NGDC/GFZ candidate models for the 10th generation International Geomagnetic Reference Field, *Earth Planets and Space*, *57*(12), 1151-1156.
McNamara, L. F. (1991), *The Ionosphere: Communications, Surveillance and Direction Finding*, Original ed., Krieger Publishing Company.

Mikhailovskii, A. B. (1992), *Electromagnetic Instabilities in an Inhomogeneous Plasma*, Institute of Physics Publishing, Bristol.
Mounir, H., et al. (1991), THE SMALL-SCALE TURBULENT STRUCTURE OF THE HIGH-LATITUDE IONOSPHERE - ARCAD-AUREOL-3 OBSERVATIONS, *Annales Geophysicae-Atmospheres Hydrospheres and Space Sciences*, *9*(11), 725-737.
NGDC (2006), SSIES Ion Scintillation Monitor, http://www.ngdc.noaa.gov/dmsp/sensors/ssies.html.
Picone, J. M., et al. (2002), NRLMSISE-00 empirical model of the atmosphere: Statistical comparisons and scientific issues, *Journal of Geophysical Research-Space Physics*, *107*(A12).
Sojka, J. J., et al. (1998), Gradient drift instability growth rates from global-scale modeling of the polar ionosphere, *Radio Science*, *33*(6), 1915-1928.
Sojka, J. J., et al. (2000), Modeling the evolution of meso-scale ionospheric irregularites at high latitudes, *Geophysical Research Letters*, *27*(21), 3595-3598.
Spencer, P. S. J., and C. N. Mitchell (2007), Imaging of fast moving electron-density structures in the polar cap, *Annals of Geophysics*, *50*(3), 427-434.
Weimer, D. R. (1995), Models of High-Latitude Electric Potentials Derived with a Least Error Fit of Spherical Harmonic Coefficients, *Journal of Geophysical Research-Space Physics*, *100*(A10), 19595-19607.
Weimer, D. R. (1996), A flexible, IMF dependent model of high-latitude electric potentials having "space weather" applications, *Geophysical Research Letters*, *23*(18), 2549-2552.
Weimer, D. R. (2001a), An improved model of ionospheric electric potentials including substorm perturbations and application to the Geospace Environment Modeling November 24, 1996, event, *Journal of Geophysical Research-Space Physics*, *106*(A1), 407-416.
Weimer, D. R. (2001b), Maps of ionospheric field-aligned currents as a function of the interplanetary magnetic field derived from Dynamics Explorer 2 data, *Journal of Geophysical Research-Space Physics*, *106*(A7), 12889-12902.
Weimer, D. R. (2005a), Improved ionospheric electrodynamic models and application to calculating Joule heating rates, *Journal of Geophysical Research-Space Physics*, *110*(A5).
Weimer, D. R. (2005b), Predicting surface geomagnetic variations using ionospheric electrodynamic models, *Journal of Geophysical Research-Space Physics*, *110*(A12).
Winglee, R. M., et al. (1997), Comparison of the high-latitude ionospheric electrodynamics inferred from global simulations and semiempirical models for the January 1992 GEM campaign, *Journal of Geophysical Research-Space Physics*, *102*(A12), 26961-26977.
Zvezdin, V. N., and S. V. Fridman (1992), Regimes of Ionospheric Turbulence from Fractal Analysis of Satellite Radio Signal Scintillations, *Journal of Atmospheric and Terrestrial Physics*, *54*(7-8), 957-962.